

Quantum simulation using arrays of gate-defined quantum dots

Mukhopadhyay, Uditendu

DOI

[10.4233/uuid:e7c4b281-c510-4522-95a6-8a4a5245a4c2](https://doi.org/10.4233/uuid:e7c4b281-c510-4522-95a6-8a4a5245a4c2)

Publication date

2019

Document Version

Final published version

Citation (APA)

Mukhopadhyay, U. (2019). *Quantum simulation using arrays of gate-defined quantum dots*. [Dissertation (TU Delft), Delft University of Technology]. <https://doi.org/10.4233/uuid:e7c4b281-c510-4522-95a6-8a4a5245a4c2>

Important note

To cite this publication, please use the final published version (if applicable). Please check the document version above.

Copyright

Other than for strictly personal use, it is not permitted to download, forward or distribute the text or part of it, without the consent of the author(s) and/or copyright holder(s), unless the work is under an open content license such as Creative Commons.

Takedown policy

Please contact us and provide details if you believe this document breaches copyrights. We will remove access to the work immediately and investigate your claim.

QUANTUM SIMULATION USING ARRAYS OF GATE-DEFINED QUANTUM DOTS

QUANTUM SIMULATION USING ARRAYS OF GATE-DEFINED QUANTUM DOTS

Proefschrift

ter verkrijging van de graad van doctor
aan de Technische Universiteit Delft,
op gezag van de Rector Magnificus prof. dr. ir. T.H.J.J van der Hagen,
voorzitter van het College voor Promoties,
in het openbaar te verdedigen op donderdag 3 oktober 2019 om 15:00 uur

door

Uditendu MUKHOPADHYAY

Master of Science in Physical Sciences,
Indian Institute of Science Education and Research Kolkata, India
geboren te Bankura, India.

CONTENTS

Summary	ix
Samenvatting	xi
1 Introduction	1
1.1 Quantum simulation	2
1.2 Thesis Outline	5
Bibliography	5
2 Basics of gate-defined quantum-dot arrays and their resemblance to the Fermi-Hubbard Model	7
2.1 Gate-defined quantum-dot arrays	8
2.1.1 Formation of gate-defined quantum dots in a 2DEG	8
2.1.2 Sensing a quantum dot array.	8
2.1.3 Hyperfine Interaction	10
2.1.4 Spin-orbit Interaction	11
2.1.5 Spin readout using Pauli Spin Blockade	11
2.2 Fermi-Hubbard model	13
2.3 Similarities between the Fermi-Hubbard model and gate-defined quantum-dot arrays	15
Bibliography	16
3 Device fabrication and experimental setup	21
3.1 Device Fabrication	22
3.1.1 Overview of the fabrication steps	22
3.1.2 Fine gate structure of 2x2 dot array.	23
3.1.3 Fine gate structure of an eight-dot linear array.	27
3.1.4 Practical tips and tricks for sample selection, handling, and bonding	28
3.2 Experimental Setup	29
3.2.1 Dilution Refrigerator.	29
3.2.2 Control and Measurement Electronics	29
Bibliography	35
4 A 2×2 quantum dot array with controllable inter-dot tunnel couplings	37
4.1 Introduction	38
4.2 Device Details.	39
4.3 Controllable Charge Occupation	40
4.4 Controllable Nearest-Neighbour Tunnel Coupling	42
4.5 Single Shot Spin Readout	43

4.6	Discussion	44
4.7	Additional Material	45
4.7.1	Controllable nearest-neighbour tunnel-coupling with one electron per dot	45
4.7.2	Thermal Excitation During Spin Readout	46
	Bibliography	48
5	Nagaoka ferromagnetism observed in a quantum dot plaquette	51
5.1	Introduction	52
5.2	Nagaoka model in the quantum dot plaquette	53
5.3	Experimental access to the Nagaoka regime.	53
5.4	Measurement results	57
5.5	Discussion	64
5.6	Additional Material	64
5.6.1	Device fabrication and methods	64
5.6.2	Extended Fermi-Hubbard models used to simulate different experiments in the main text	66
5.6.3	Mapping 3-spin states onto 2-spin measurements	72
	Bibliography	74
6	A capacitance spectroscopy-based platform for realizing gate-defined electronic lattices	77
6.1	Introduction	78
6.2	Heterostructure and Capacitance spectroscopy.	78
6.3	Gate Design and Fabrication	79
6.4	Measurements	81
6.4.1	Global gates: disorder levels	81
6.4.2	Grid gates: periodic potential strength	83
6.5	Discussion: what to search for in future data	86
6.6	Outlook	87
6.7	Supplementary Material	88
6.7.1	Capacitance bridge	88
6.7.2	Design and fabrication details	88
6.7.3	Conversion from capacitance to density of states	91
	Bibliography	93
7	Conclusions and Outlook	97
7.1	Conclusions.	98
7.2	Outlook	99
7.2.1	Simulation using a 2x2 dot array device	99
7.2.2	Scaling of quantum dot arrays	100
7.2.3	Simulation using larger quantum dot array devices	102
	Bibliography	103

Acknowledgements	105
A Fabrication recipe of the Quantum dot devices in GaAs	109
Curriculum Vitæ	117
List of Publications	119

SUMMARY

We are entering the era of the second quantum revolution, where we aim to harness the power of quantum mechanics to create new technologies. Quantum technologies have the potential to revolutionize the fields of simulation, computation, communication, sensing, metrology, and many others. Here we discuss analog quantum simulation, which has attracted a lot of attention in the last few years from several platforms. Although arrays of gate-defined quantum dots exhibit significant potential for analog simulation, example experiments have been few and far between. This thesis focuses on simulating the Fermi-Hubbard model using two dimensional (2d) arrays of quantum dots.

The first experiment describes the creation and measurement of a 2×2 quantum dot array. Historically, most experiments with quantum dots have been performed with linear arrays due to the relative ease of fabrication. We introduce a bi-layer gate structure, facilitated by the lift-off of sputtered silicon nitride, to create the 2×2 dot array. This gate design enables us to achieve unprecedented tunability of the tunnel coupling between all nearest-neighbor pairs of dots in 2d arrays. We also demonstrate individual control over the chemical potential and the electron occupation of each dot along with accurate measurement of the on-site and inter-site interaction terms. The use of virtual gates significantly aids in the tuning of tunnel coupling and chemical potential. The demonstrated high degree of control of the system along with fast single-shot spin-readout achieved through Pauli spin blockade establish this dot array as a promising simulator of the Fermi-Hubbard model.

The 2×2 dot array is used to simulate Nagaoka ferromagnetism in the next experiment. This form of itinerant ferromagnetism arises from the Fermi-Hubbard model, and was first shown analytically in the limit of infinite interaction strengths and infinite lattices by Nagaoka in 1966. Nagaoka ferromagnetism has been a topic of rigorous theoretical studies ever since, but its experimental signature has eluded us for more than five decades. In this experiment, we load the four dot plaquette with three electrons and demonstrate the emergence of spontaneous ferromagnetism by measuring the spin correlation of two out of the three electrons. Changing the topology of the array to an open chain is shown to destroy the ferromagnetic signature, consistent with the Lieb-Mattis theorem. We also show indications that this ferromagnetic ground state can be destroyed by applying a perpendicular magnetic field, unlike most other forms of ferromagnetism. However, this ground state shows striking robustness to the offset in the local potential of any dot. This is the first experimental verification of Nagaoka's prediction as well as the first simulation of magnetism using quantum dot arrays.

The final experiment takes a different approach to simulate the Fermi-Hubbard model with a large 2d array of quantum dots. The dot array is created using only three gates in a

top-down approach. This allows for only global control over the electron filling and tunnel coupling of the dots, contrary to the previous experiments. The readout is performed with capacitance spectroscopy, which allows us to directly probe the density of states of the two-dimensional electron systems. We measure the disorder levels and optimize both substrates and gating strategies to induce periodic potential, sufficiently stronger than the disorder level, at the 2d electron gas. Although we demonstrate a novel platform for the realization of artificial lattices of interacting particles, this effort is currently limited by the substrate inhomogeneity.

SAMENVATTING

We betreden het tijdperk van de tweede quantumrevolutie, waarin het doel is de kracht van quantummechanica te exploiteren om nieuwe technologieën te creëren. Quantumtechnologie heeft de potentie een revolutie te ontketenen in vakgebieden als simulatie, berekening, communicatie, sensoren, metrologie en vele anderen. Hier bespreken we analoge quantumsimulatie, dat de afgelopen jaren de aandacht heeft getrokken van verschillende platformen. Hoewel roosters van door elektrodes gedefinieerde quantumdots significant potentieel bezitten voor het uitvoeren van analoge simulaties, zijn er weinig of geen experimenten. Dit proefschrift focust op het simuleren van het Fermi-Hubbard-model met behulp van tweedimensionale roosters van quantumdots.

Het eerste experiment beschrijft het vormen en meten van een 2×2 -quantumdotrooster. Historisch zijn de meeste experimenten met quantumdots uitgevoerd met lineaire roosters vanwege de relatief gemakkelijke fabricage. We introduceren een dubbellaagse elektrodestructuur, mogelijk gemaakt door lift-off van gesputterd siliciumnitride, om een 2×2 -quantumdotrooster te creëren. Dit elektrodeontwerp stelt ons in staat niet eerder gedemonstreerde controle over de tunnelkoppeling tussen alle aan elkaar grenzende quantumdots in tweedimensionale roosters te bereiken. Tevens demonstreren we individuele controle over het chemische potentiaal en de elektronbezetting van iedere quantumdot in combinatie met accurate meting van de intradot- en interdotinteractietermen. Het gebruik van virtuele elektrodes draagt significant bij aan het instellen van de tunnelkoppeling en de chemische potentiaal. De gedemonstreerde hoge mate van controle over het systeem in combinatie met snelle uitlezing van individuele spins, bereikt door Pauli-spinblokkade, vestigt dit quantumdotrooster als veelbelovende simulator van het Fermi-Hubbard-model.

In het volgende experiment gebruiken we het 2×2 -quantumdotrooster om Nagaoka-ferromagnetisme te simuleren. Deze vorm van ferromagnetisme gebaseerd op mobiele elektronen komt voort uit het Fermi-Hubbard-model en werd voor het eerst analytisch getoond in de limiet van oneindige interactiesterktes en oneindige roosters door Nagaoka in 1966. Nagaoka-ferromagnetisme is sindsdien onderwerp van diepgaand theoretisch onderzoek, maar experimentele waarneming blijft al meer dan vijf decennia uit. In dit experiment laden we het rooster van vier quantumdots met drie elektronen en tonen het ontstaan van spontaan ferromagnetisme aan door het meten van spincorrelaties tussen twee van de drie elektronen. Het veranderen van de topologie van het rooster naar een open rij verbreekt de ferromagnetische kenmerken, in overeenstemming met het Lieb-Mattis-theorema. Tevens laten we aanwijzingen zien dat deze ferromagnetische grondtoestand wordt verbroken door het aanbrengen van een loodrecht magneetveld, in tegenstelling tot de meeste andere vormen van ferromagnetisme. Echter, deze grondtoestand is verbazingwekkend goed bestand tegen verschillen in het lokale potentiaal van elk van de quantumdots. Dit is de eerste experimentele verificatie van

Nagaoka's voorspelling en tevens de eerste simulatie van magnetisme met behulp van quantumdotroosters.

Het laatste experiment maakt gebruik van een andere aanpak om het Fermi-Hubbard-model te simuleren door middel van een groot tweedimensionaal rooster van quantumdots. Het quantumdotrooster wordt gevormd met behulp van slechts drie elektrodes door middel van een top-down-aanpak. In tegenstelling tot de eerder experimenten, laat dit enkel globale controle over de elektronbezetting en tunnelkoppeling van de quantumdots toe. Uitlezen vindt plaats op basis van capaciteitspectroscopie, dat ons in staat stelt de toestandsdichtheid van het tweedimensionale elektronsysteem direct te onderzoeken. We meten het niveau van wanorde en optimaliseren zowel substraten als strategieën om periodieke potentialen voldoende sterker dan de wanorde in het tweedimensionaal elektronengas te induceren. Hoewel we een nieuwe platform voor het realiseren van kunstmatige roosters van interacterende deeltjes demonstreren, wordt deze aanpak op dit moment gelimiteerd door substraathomogeniteit.

1

INTRODUCTION

Nature isn't classical, dammit, and if you want to make a simulation of nature, you'd better make it quantum mechanical, and by golly it's a wonderful problem, because it doesn't look so easy.

Richard Feynman

1.1. QUANTUM SIMULATION

The elegance of physics lies in its brevity. A few laws or axioms can explain innumerable phenomena. But this is only the beginning of the story. Knowing a theory of physics only allows us to express any problem using a few elegant equations, which we then need to solve in order to find the relevant answers. These solutions often tend to get quite tedious, especially for large systems. Generally, we use computers to help us solve these equations. Unfortunately, this is not a viable approach when the problem at hand is governed by the laws of quantum mechanics with interacting particles. The quantum correlations between the constituent particles of these problems grow exponentially with the number of particles and quickly become intractable by a classical computer. For example, even with the best supercomputers available today, it will take longer than the age of the universe to simulate a single molecule with tens of atoms. As the natural world around us is inherently quantum, to understand it better, we need a realistic way of solving these problems. To tackle this issue, Richard Feynman first introduced the idea of simulating quantum with quantum [1]. Building on this idea, one can use a quantum system to simulate another and thus avoid the exponential scaling of required resources.

Quantum systems are difficult to prepare, protect and measure. Due to their constant interaction with the environment, the information stored in a quantum state is lost rather quickly. Moreover, the traditional measurement tools used by scientists are classical in nature and not readily suited for quantum measurements. For decades, all these essentially prevented researchers from using quantum systems in any controlled experiment.

But tremendous technological advances made in the last few decades have enabled us to exploit the full potential of quantum mechanics in experiments. Scientists now routinely use single electrons or photons to generate superpositions and entanglements in labs. This, in turn, has facilitated numerous efforts to utilize the power of quantum to revolutionize technologies in the areas of computation, simulation, secure communication, just to name a few. In this thesis, I am going to focus on simulation.

There are two main ways to simulate a system of interest using another quantum system, namely digital and analog simulation. The ideas are quite similar to their classical counterparts. Let's say we want to simulate the air drag of a car in a wind tunnel. We can make a computer model of the car and the wind and solve the equations to get our answer. The quantum equivalent of this approach is known as digital quantum simulation. Here, we use a highly programmable quantum processor to map the Hamiltonian of the system of interest and measure the energies of different states after the desired time-evolution. Alternatively, we can emulate the car-air drag problem by measuring the air drag on a scaled model of the car in a model wind tunnel. Similarly, in an analog quantum simulation, we map one system on to a similar, more controllable, artificial system. By changing the parameters of this artificial system and measuring their effects, we try to learn about the actual system of interest. The control required over these artificial systems is still significantly less than in digital simulations.

Due to its slightly relaxed control requirement, analog simulation is perfectly suited for implementation using currently available, noisy, intermediate-scale quantum technology [2]. Essentially, in this approach, we can sacrifice the full coherent control of a quantum system, which is proven to be particularly tricky with increasing system size, in

favor of faster scaling up. One of the main challenges in analog simulation is to find an artificial system close enough to the system of interest. As one can imagine, the validity of analog simulation results depends largely on the initial similarity. In the last few years, researchers have used several platforms [3–6], such as optical lattices and trapped ions, to successfully simulate physical systems of interest.

Arrays of gate-defined quantum dots are especially promising candidates for analog quantum simulation. These quantum dots are islands of electrons electrostatically created by strategic depletion of a two-dimensional electron gas (2DEG). Electrons are loaded in these dots from nearby reservoirs and the number of electrons in each dot can be controlled up to single electron. Additionally, we can control the tunnel coupling between the neighboring sites. These arrays form a natural platform for emulating the Fermi-Hubbard model, as they adhere to almost the same Hamiltonian. The Fermi-Hubbard model provides a description of interacting electrons in a lattice. This seemingly simple model reveals strong quantum correlations, which can explain striking phenomena such as superconductivity [7] or certain forms of magnetism [8]. But solutions to the Fermi-Hubbard model become intractable by classical methods with increasing lattice size. With quantum dot arrays however, the ease of tunability, control of the relevant parameters, low electron temperature, fast measurement of the spin and charge states, and potential for scalability potentially enable us to venture into unexplored territory in the Fermi-Hubbard phase-space. Furthermore, we hope to utilize the breakthroughs coming from a booming interest in the field, both from industries and research labs, in using quantum dots as the basic underlying hardware of quantum computers.

Most experiments involving quantum dots have so far been conducted with a handful of dots in linear configurations [9–14]. In 2017, Hensgens et. al. demonstrated the required control over a three-dot linear array and simulated the transition between Coulomb blockade and collective Coulomb blockade [15]. Scaling the number of dots in a linear array has historically been limited by the manual tuning required to fight both the intrinsic and the fabrication-induced disorders. Moreover, the distance between dots and electron reservoirs introduces an extra challenge for (un)loading electrons. Scaling from a linear to a two-dimensional (2D) array introduces additional challenges in terms of routing of the gates, which make it difficult to fabricate a 2D array with similar control to that of linear arrays. Recently, researchers have come up with preliminary ideas for efficient tuning of larger linear arrays. Meanwhile, the handful of attempts to go beyond a linear array of dots have lacked the control over the parameter-space needed to try out simulation experiments, especially involving spins [16–18]. The only instance of simulation with such an array probes the charge-frustration in a triangular, three-dot system [19].

The aim of this thesis is to explore ways to scale up to 2D quantum dot arrays and use them in analog simulation of the Fermi-Hubbard model. The quantum dots are created in a 2DEG, formed in a GaAs/AlGaAs heterostructure. We use two separate methods to scale up the arrays. On one hand, we investigate a top-down approach to make a large 2D array of 1000×1000 dots without site-specific control. We analyze the feasibility of using this system to simulate the metal - Mott insulator transition. On the other hand, we employ a bottom-up approach to fabricate and tune up a 2×2 dot array. We address the

issue of the tunability of the system up to a point where it is possible to simulate physical models in this device. Finally, we use this device to perform simulation of Nagaoka ferromagnetism, the occurrence of ferromagnetic ground state in an almost-half-filled lattice, driven by interactions. This unusual form of ferromagnetism exists without the presence of a magnetic field. Furthermore, the ferromagnetic ground state can be destroyed with an external magnetic field. The results obtained from this experiment could enhance our understanding of magnetism as a whole.

Although the main target of my work is analog simulation, the advances made in my thesis should also be useful for quantum computation experiments using quantum dots. Moreover, we look into the fabrication of an eight-dot linear array, to be used for quantum simulations. Furthermore, the bottom-up fabrication technique to create the 2×2 dot array can readily be extended to a ladder array of size $2 \times N$.

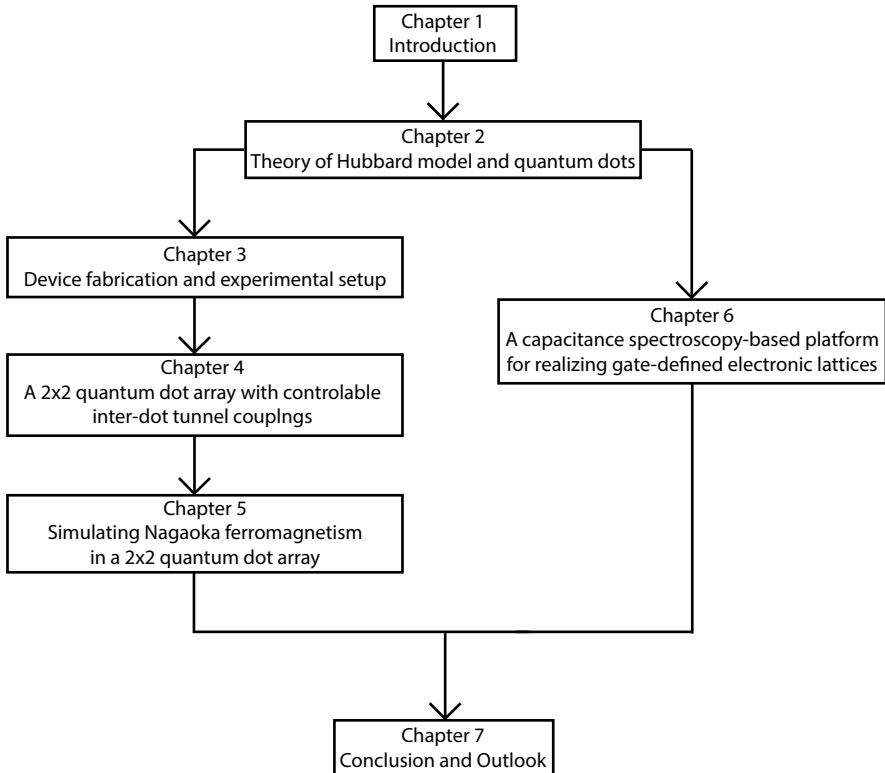


Figure 1.1: Structure of the dissertation

1.2. THESIS OUTLINE

As mentioned earlier, I followed two different approaches to perform quantum simulation using 2D quantum-dot arrays. Although, my initial work was with the 1000×1000 dot array, for reasons which will be clear after reading this thesis, most of my research uses the 2×2 dot array. As these two approaches are rather different, they are treated separately here. Chapters 3 to 5 elaborate on our work using the 2×2 dot array. In chapter 6, the findings from the 1000×1000 dot work are discussed. Finally, the two approaches are combined again in chapter 7. The structure of the dissertation is shown in Fig. 1.1.

Finally, here is a brief outline of the chapters:

Chapter 2 reviews the essential theoretical concepts needed to understand the experimental results in the following chapters. First, I describe the underlying principles of electrons in electrostatically-defined lateral quantum dots in a 2DEG. This is followed by a discussion of the Fermi-Hubbard model and its similarities to a quantum dot array. Finally, the chapter ends with a short introduction to Nagaoka ferromagnetism.

In **Chapter 3**, I start with a detailed description of the fabrication for the 2×2 quantum dot array, measured during the course of this research. This is followed by a discussion of the experimental set-up used in **Chapters 4** and **5**.

Chapter 4 focuses on creating a 2×2 dot system, with individual control over each dot. Here, I present measurements that demonstrate control over electron filling and nearest-neighbour tunnel coupling, together with fast single-shot spin read-out — establishing our system as a promising solid-state analog quantum simulator.

I present the results of one such simulation in **Chapter 5**. We used the symmetry present in our sample to show the emergence of a ferromagnetic ground state in an almost half-filled square lattice, as theoretically predicted by Nagaoka in 1966. We then tuned the Hamiltonian parameters to move between regions with ferromagnetic and unpolarised ground states to further test this interpretation.

Chapter 6 describes our effort to dramatically scale up the number of quantum dots in an array at the cost of individual control over the dots. In this context, I discuss the disorder and the (in)homogeneity of the devices measured. We used capacitance spectroscopy as a global measurement technique for this part of the research.

Chapter 7 summarizes the key findings of this thesis and outlines possible steps towards fabricating and using larger dot arrays for quantum simulation.

BIBLIOGRAPHY

- [1] R. P. Feynman, *International Journal of Theoretical Physics* **21**, 467 (1982).
- [2] J. Preskill, *Quantum* **2**, 79 (2018).
- [3] I. Bloch, J. Dalibard, and S. Nascimbene, *Nature Physics* **8**, 267 (2012).
- [4] R. Blatt and C. F. Roos, *Nature Physics* **8**, 277 (2012).
- [5] A. Aspuru-Guzik and P. Walther, *Nature physics* **8**, 285 (2012).
- [6] A. A. Houck, H. E. Türeci, and J. Koch, *Nature Physics* **8**, 292 (2012).

- [7] P. W. Anderson, in *Journal of Physics: Conference Series*, Vol. 449 (IOP Publishing, 2013) p. 012001.
- [8] D. C. Mattis, *The theory of magnetism I: statics and dynamics*, Springer series in solid-state sciences (Springer, 1981).
- [9] J. R. Petta, A. C. Johnson, J. M. Taylor, E. A. Laird, A. Yacoby, M. D. Lukin, C. M. Marcus, M. P. Hanson, and A. C. Gossard, *Science* **309**, 2180 (2005).
- [10] T. A. Baart, M. Shafiei, T. Fujita, C. Reichl, W. Wegscheider, and L. M. K. Vandersypen, *Nature Nanotechnology* **11**, 330 EP (2016).
- [11] F. K. Malinowski, F. Martins, T. B. Smith, S. D. Bartlett, A. C. Doherty, P. D. Nissen, S. Fallahi, G. C. Gardner, M. J. Manfra, C. M. Marcus, and F. Kuemmeth, *Phys. Rev. X* **8**, 011045 (2018).
- [12] T. Fujita, T. A. Baart, C. Reichl, W. Wegscheider, and L. M. K. Vandersypen, *npj Quantum Information* **3**, 22 (2017).
- [13] T. Ito, T. Otsuka, S. Amaha, M. R. Delbecq, T. Nakajima, J. Yoneda, K. Takeda, G. Allison, A. Noiri, K. Kawasaki, and S. Tarucha, *Scientific Reports* **6**, 39113 EP (2016).
- [14] A. R. Mills, D. M. Zajac, M. J. Gullans, F. J. Schupp, T. M. Hazard, and J. R. Petta, *Nature Communications* **10**, 1063 (2019).
- [15] T. Hensgens, T. Fujita, L. Janssen, X. Li, C. J. Van Diepen, C. Reichl, W. Wegscheider, S. Das Sarma, and L. M. K. Vandersypen, *Nature* **548**, 70 (2017).
- [16] A. Noiri, K. Kawasaki, T. Otsuka, T. Nakajima, J. Yoneda, S. Amaha, M. R. Delbecq, K. Takeda, G. Allison, A. Ludwig, A. D. Wieck, and S. Tarucha, *Semicond. Sci. Technol.* **32**, 084004 (2017).
- [17] R. Thalineau, S. Hermelin, A. D. Wieck, C. Bäuerle, L. Saminadayar, and T. Meunier, *Appl. Phys. Lett.* **101**, 103102 (2012).
- [18] P.-A. Mortemousque, E. Chanrion, B. Jadot, H. Flentje, A. Ludwig, A. D. Wieck, M. Urdampilleta, C. Bäuerle, and T. Meunier, arXiv preprint arXiv:1808.06180 (2018).
- [19] M. Seo, H. K. Choi, S.-Y. Lee, N. Kim, Y. Chung, H.-S. Sim, V. Umansky, and D. Mahalu, *Phys. Rev. Lett.* **110**, 046803 (2013).

2

BASICS OF GATE-DEFINED QUANTUM-DOT ARRAYS AND THEIR RESEMBLANCE TO THE FERMI-HUBBARD MODEL

The purpose of this chapter is to outline the essential theoretical concepts that elucidate the experimental results described in the later chapters. We start by explaining the basics of gate-defined quantum dots and how to create, control and measure them. Next, we present a short review of the Fermi-Hubbard model, along with its importance in solid-state physics. Finally, the similarities between the physics of a quantum-dot array and the Fermi-Hubbard model are discussed.

2.1. GATE-DEFINED QUANTUM-DOT ARRAYS

Quantum dots are artificially created islands of electrons (holes), where the charge occupation can be precisely controlled. The energy levels in a quantum dot are discrete at low temperature due to their small size (1 - 100 nm) and three-dimensional (3D) confinement. This, along with the tunability of several parameters of quantum dots enable us to use them as artificial atoms. Researchers around the world use different kinds of quantum dots, e.g.: quantum dots defined in semiconductor nano-wires [1, 2] and carbon nanotubes [3], self-assembled quantum dots [4], single molecules controlled by electrodes [5] etc., for various experiments. Here, we discuss gate-defined quantum dots [6, 7] within a 2DEG created in a semiconductor heterostructure of GaAs/AlGaAs.

2.1.1. FORMATION OF GATE-DEFINED QUANTUM DOTS IN A 2DEG

As mentioned earlier, the quantum dots are created by confining charge particles in 3D. Due to the heterostructure design, the electrons in the 2DEG are confined in the vertical (z) direction, whereas the confinement in the other two directions comes from the applied electric field through gate voltages.

The 2DEG is formed in a heterostructure of GaAs and AlGaAs ($Al_xGa_{1-x}As$) grown using molecular beam epitaxy. During this growth, a very thin Si delta-doping band is introduced within the AlGaAs layer. A triangular potential well forms at the interface of the GaAs and the AlGaAs layers due to the differences in bandgap between them. The extra electrons coming from the Si dopants accumulate at this potential well to create the 2DEG. At low temperature, only the lowest mode of the well gets populated with electrons. This effectively restricts their movement perpendicular to the plane of the 2DEG. These electrons can still move freely in the 2DEG plane. The matching lattice constants for GaAs and AlGaAs and tremendous development in growth technique help in creating heterostructures with a low disorder. The wafers used for the works described in chapters 3-5 have the 2DEG roughly 90 nm below the surface of the heterostructure with $x \approx 0.3$, mobility $\sim 2 \times 10^6$ cm²/Vs, and electron density $\sim 2 \times 10^{11}$ cm⁻².

The confinement of electrons in a 2DEG acts as the first step in forming gate-defined quantum dots. We fabricate metal gates on the surface of the heterostructure to obtain the confinement from the other two directions. The potential landscape of the 2DEG can be altered by applying voltages to these gates. This change in potential landscape enables the creation of a quantum dot by depleting parts of the 2DEG and confining a certain number of electrons in a well-defined location. We can control the number of electrons in a dot by changing the voltage applied to certain gates. We can also control the coupling between two dots or a dot and a reservoir by using gate voltages. The design of the gate-structure dictates the size and the shape of a quantum dot array. Details of the gate-structures used are discussed in Chapter 3.

2.1.2. SENSING A QUANTUM DOT ARRAY

We have discussed how to create and control electron-occupation of a quantum dot by changing gate-voltages in the previous subsection. Here, we describe how one can detect the response of electrons in a quantum dot array to changes in gate-voltages, using charge-sensing [7]. In charge-sensing, the response of a nearby charge sensor is measured as a function of the gate voltages, which create the dot array. The charge sensor

is able to detect the movement of electrons through capacitive coupling to the dot array of interest. As this detection technique does not affect the charge state of the dot array of interest, we prefer it rather than measuring the current transport through quantum dots [6]. Several quantum objects, such as quantum-point contacts [8] and quantum dots [9], has been used as a charge-sensor so far. We use a separate quantum dot as a charge-sensing dot.

To use a quantum dot as a charge sensor, we first tune the gate voltages to be on a steep flank of a Coulomb peak. The current passing through the sensing dot in this configuration is highly sensitive to any small change in the electrostatic environment around it. Any addition, removal or movement of charge in the quantum dot array results in a change of the current measured through the sensing dot. The response of the sensing dot as a function of different gate-voltages that define the array is used to recognize different charge configurations of the dot array. Plots of these responses are commonly known as the charge-stability diagrams. These diagrams enable us to load a deterministic number of electrons in each dot by changing gate voltages. The sensitivity of a charge sensor depends on the capacitive coupling between the sensor and the dot array. The coupling decreases with increasing distance between the two. Multiple sensing dots can be used to sense all parts of a large quantum dot array.

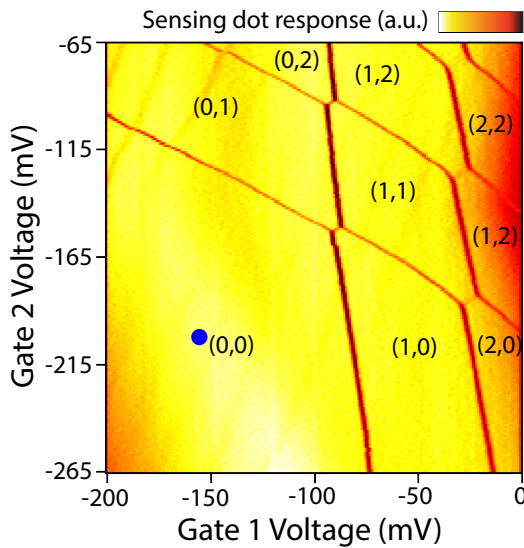


Figure 2.1: Charge stability diagram of a double-dot array, measured by charge sensing. The differentiated signal of the charge sensor is plotted as a function of two gate voltages. In the label (a,b), a and b denote the number of electrons in dots 1 and 2 respectively.

A double dot charge stability diagram is shown in Fig. 2.1. The diagram indicates the electron occupation of the dot array from (0,0) to (2,2), where (a,b) depicts the number of electrons in dots 1 and 2 respectively. The lines in this plot represent the movement of electrons in the dot array. The almost vertical and horizontal lines are addition lines for dots 1 and 2 respectively. We can change gate voltages and add (remove) one elec-

tron from a reservoir to a dot by crossing an addition line corresponding to the dot. As a result, going over any addition line changes the total number of electrons in the dot array. It is essential to know the exact electron occupation of the array at a given set of gate voltages to perform quantum dot measurements and experiments. To keep track of the exact number of electrons in the dots, increasingly negative voltages are applied to the gates, until no new addition line appears in the diagram, indicating that both quantum dots are empty (for example, the blue circle in Fig. 2.1). From this point, electrons can be added to each dot by crossing the corresponding addition lines. A close look at Fig. 2.1 reveals another kind of line, which appears when two addition lines cross each other. Going across these lines doesn't change the total electron number in the dot array, but moves one electron from one dot to another. These are called inter-dot lines. In general, addition lines appear more prominently than inter-dot lines in a charge stability diagram.

We have routinely used charge-stability diagrams to tune-up and control the dot-arrays. With an increasing number of dots in an array, these diagrams become harder to interpret, due to cross-talk between different gates and dots [10]. These effects can be compensated by using a linear combination of multiple gate voltages as a virtual gate [11, 12]. Changing a virtual gate voltage is supposed to only influence a particular quantum dot while keeping the other dots unaffected. A detailed description of how these virtual gates are defined can be found in section 4.4.

Apart from measuring the electron occupancy of each dot, we also use the charge stability diagrams to estimate different relevant energies (see subsection 2.3) related to a dot array. The exact estimation processes are described in details in chapter 4.

2.1.3. HYPERFINE INTERACTION

The spin of an electron in a dot interacts with the nuclear spins of the host material via hyperfine interaction. In a GaAs quantum dot, an electron is surrounded by atoms (both Ga and As) with non-zero nuclear spin. The Hamiltonian for this Fermi contact hyperfine interaction is given by

$$\mathcal{H}_{HF} = \sum_{k=1}^N A_k \vec{I}_k \cdot \vec{S} \quad (2.1)$$

The vectors \vec{I}_k and \vec{S} denote the spin operator for nucleus k and the electron spin under consideration respectively [13]. The coupling strength (A_k) depends on the overlap between the electron and the nucleus wavefunctions. For a typical GaAs dot, roughly 10^6 nuclei contribute with nonzero individual coupling.

We can model the effect of this ensemble of nuclear spins by an effective magnetic field $\left(\vec{B}_N = \frac{\sum_{k=1}^N A_k \vec{I}_k}{g\mu_B} \right)$, known as the Overhauser field. Under this assumption:

$$\mathcal{H}_{HF} = g\mu_B \vec{B}_N \cdot \vec{S} \quad (2.2)$$

where g is the electron g -factor and μ_B is Bohr magneton. B_N attains its maximum value ($B_{N,max} \sim 5$ T in GaAs [14]) when all the nuclear spins are fully polarized. However in almost all our experiments, the nuclear spins should be completely unpolarized as there is

no external magnetic field. So, we expect the average value of B_N to be 0 with a Gaussian distribution of width $\sigma_N = \frac{B_{N,max}}{\sqrt{N}} \approx 5$ mT in all directions [15].

Next, we discuss the effect of this Overhauser field on electrons in more than one dot. Two or more spatially separated dots experience slightly different Overhauser fields (ΔB_N) from each other due to local fluctuations. These differences can be used to drive transitions between different spin states. For example, in the case of two electrons in two dots, the x, y and z components of ΔB_N mix the S(1,1) state with the $T_+(1,1)$, $T_-(1,1)$ and $T_0(1,1)$ states [7, 16].

2.1.4. SPIN-ORBIT INTERACTION

The magnetic moment ($\mu_B = 9.27 \times 10^{-24}$ J/T) of the spin of an electron interacts with any magnetic environment. An electron moving in a electric field (\vec{E}) experiences an effective magnetic field, $\vec{B}_{SO} \propto \vec{E} \times \vec{p}$. Here \vec{p} is the momentum of the electron. The resulting interaction of an electron spin and the magnetic field arising from its motion is called the spin-orbit interaction (SOI). The spin-orbit Hamiltonian has the form $\mathcal{H}_{SO} \propto \vec{\sigma} \cdot \vec{B}_{SO}$, where $\vec{\sigma}$ is the Pauli vector.

There are two main origins of spin-orbit coupling in a GaAs/AlGaAs heterostructure.

1. The local electric fields due to the bulk inversion asymmetry (BIA) in GaAs crystals lead to the Dresselhaus contribution to the SOI [17].
2. The structural inversion asymmetry (SIA) due to the asymmetric confining potential at the GaAs/AlGaAs interface gives rise to the Rashba contribution to the SOI [18].

For a 2DEG grown along the (001) crystallographic direction, the spin-orbit Hamiltonian is given by

$$\mathcal{H}^{2D,(001)} = \alpha(-p_y\sigma_x + p_x\sigma_y) + \beta(-p_x\sigma_x + p_y\sigma_y) \quad (2.3)$$

Here x and y refer to (100) and (010) crystallographic directions respectively and α, β are the strengths of Rashba and Dresselhaus interactions. α depends on material properties and the confining potential, whereas β depends on the material properties and $\langle p_z^2 \rangle$. From Eqn. 2.3, we can see that the Rashba and Dresselhaus interactions orient differently in different directions in the XY plane (Fig. 2.2). As a result, effective spin-orbit interaction also depends on the direction of the electron's motion.

The SOI enables electric-field fluctuations to cause spin-relaxation [20]. An electric field cannot couple to pure spin states. However, due to SOI, the eigenstates become admixtures of spin and orbital states [21]. The orbital parts of these states couple to the electric field and as a result enable spin-relaxation through SOI. In Chapter 5, we discuss the effects of SOI on our experiment in detail.

2.1.5. SPIN READOUT USING PAULI SPIN BLOCKADE

Finally, we discuss how to measure the spins of the electrons in a quantum dot. We have used the principle of Pauli spin blockade (PSB) [22] to perform spin measurements in our work. PSB is used to determine if two electron-spins in two separate dots are in singlet or

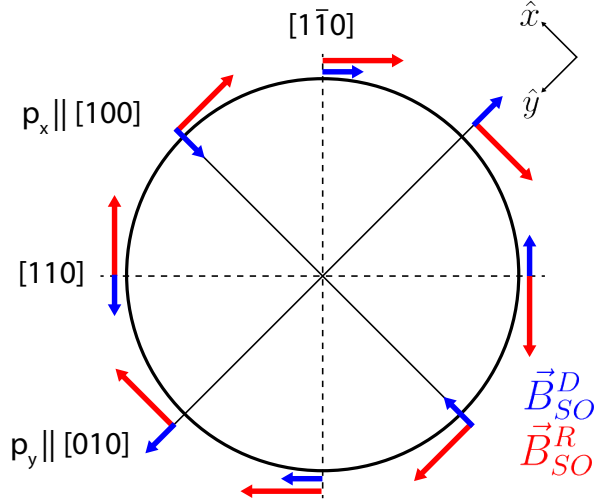


Figure 2.2: The spin-orbit field (\vec{B}_{SO}) acting on an electron moving in a 2DEG with momentum \vec{p} . The red and blue arrows refer to Rashba and Dresselhaus components (chosen with different modulus and $\alpha < 0, \beta > 0$) respectively. This figure is adopted from Ref. [19].

triplet configuration. We start in the charge state (1,1) of a double dot and try to quickly pulse to the (2,0) state (or (0,2) state). This protocol should show us two different signals in the charge-sensor depending on the relative spin-configuration of the electrons under the right conditions. If the two electrons are in a spin-singlet configuration, they will instantly move to the same dot ((2,0) charge configuration). However, a transition to (2,0) charge state is forbidden if the two electrons are in spin-triplet configuration, as the three (2,0) triplet states (T_0 , T_+ and T_-) are higher in energy due to Pauli exclusion principle [23]. The electrons will then remain in the (1,1) charge configuration, which can be measured by the charge sensor signal [24]. The effect is known as the Pauli spin blockade (PSB). This blockade is lifted after a finite time as the hyperfine field (ΔB_N) mixes the three triplet states with the singlet (S(1,1)) state, which allows a transition to the (2,0) charge state [7, 25]. The mixing rates of the S(1,1) state with the $T_+(1,1)$, $T_-(1,1)$ and $T_0(1,1)$ states are expected to be equal without the presence of an external magnetic field (relevant for our experiments). This, in turn, gives one relaxation time from all three triplet states to the singlet state. We note that this phenomenon is detectable in a small detuning range close to the resonance condition between (1,1) and (2,0) charge states. Outside this detuning range, the blockade is quickly lifted through an exchange of one electron with one of the dot reservoirs, making it hard to detect. The read-out window can be adjusted by changing the tunnel coupling of the dots to their individual reservoirs [26]. Experimental results of PSB readout in our system are described in Chapter 4.

2.2. FERMI-HUBBARD MODEL

The properties of electrons in various materials is an active field of research for several decades. Different models are used to study these properties depending on the interactions present between the electrons and the ion cores. The free electron model [27] successfully describes the behavior of delocalized valence electrons in metals, by neglecting electron-electron and electron-ion interactions. Whereas, the tight binding model describes electrons tightly confined to individual atoms [28]. These highly localized electrons have limited interaction with electrons in neighboring atoms through the superposition of electron wave functions. We focus on the Hubbard model [29] in this thesis due to its applicability to quantum dot arrays. The Hubbard model is commonly used to describe Coulomb-induced strongly-correlated electron systems. Although this model was first introduced to study transition-metal monoxides (FeO, CoO, etc), it has since been used to study several fascinating systems, such as heavy fermions [30] and high-temperature superconductors[31].

The Hubbard model in its simplest form approximates a solid-state system by a collection of atoms (sites) each with a single electronic orbital (band). Each orbital can have at most two electrons with opposite spins (\uparrow or \downarrow) following Pauli's exclusion principle. The nuclei of these atoms are considered to be fixed in position and create a lattice. The electrons interact via Coulomb interaction. We only consider the interaction between electrons in the same atomic orbital. This interaction is either zero (if the orbital is empty or has a single electron) or U (if the orbital has two electrons). We assume no interaction between electrons in different atomic orbitals in the basic Hubbard model. The kinetic energy of these electrons is given by the ability of electrons to move from one orbital to another. The energy scale t of this 'hopping' is given by the overlap of electronic wave-functions of the two atomic orbitals under consideration. The hopping is significant only between nearest neighbors. The basic form of the Hubbard model consists of only these two energy terms. We write the Hubbard Hamiltonian in second quantization notation, using fermionic creation and annihilation operators (c^\dagger and c):

$$H = U \sum_i n_{i\uparrow} n_{i\downarrow} - t \sum_{\langle i,j \rangle, \sigma} \left[c_{i\sigma}^\dagger c_{j\sigma} + h.c. \right] \quad (2.4)$$

Here, $\sigma = \uparrow$ or \downarrow denote the spin of an electron and i, j refer to the index of the lattice site. $c_{i\sigma}^\dagger$ ($c_{i\sigma}$) refers to the creation (annihilation) operator of an electron of spin σ on site i . Finally, $n_{i\sigma} = c_{i\sigma}^\dagger c_{i\sigma}$ is the number operator which gives us the number of electrons with spin σ on site i . The value of this number operator can either be 0 or 1 in this model. We add another energy term μ (chemical potential) to this Hamiltonian, which controls the filling of electrons on each site. The resultant Hamiltonian takes the following form:

$$H = U \sum_i n_{i\uparrow} n_{i\downarrow} - t \sum_{\langle i,j \rangle, \sigma} \left[c_{i\sigma}^\dagger c_{j\sigma} + h.c. \right] - \mu \sum_i n_i \quad (2.5)$$

For an atom with multiple orbitals, the inner orbitals are considered together with the nucleus as a fixed ion core, whereas the outermost orbital is considered as the single band.

This model looks reasonably simple at first glance. But, a strong electron-electron correlation arises from this model with increasing lattice size. Several interesting physical phenomena emerge from the simple looking model due to these correlations, as we start to change the different Hubbard parameters. In the limit of low temperature and $t \ll U$, the Hubbard model gives rise to a Mott insulator phase at half filling (one electron per site). Tunneling is suppressed in this limit, as it results in double-occupancy of a site, which is energetically unfavorable. As a result, the energy band breaks into two. The electrons going into an empty site fills the lower band. Whereas, the electrons occupying an already singly-occupied site fills the upper band. Thus at half-filling, the lower band is full whereas the upper band is empty, making the system behave like an insulator [32]. One can destroy the Mott-insulator phase by decreasing the ratio of U/t . Quantum fluctuations (hopping) becomes more and more favorable with decreasing U/t and the electrons tend to move around the lattice. This essentially closes the gap between the upper and the lower band and makes the system behave like a metal. A similar effect is also expected if the thermal fluctuation is too large. Another way to destroy this insulator phase is to change the lattice filling (introduce doping) using the chemical potential (μ). The Mott insulators are also closely related to high-temperature (cuprate) superconductors [31, 33]. It is predicted that this superconducting phase can be accessed by gradually introducing doping away from half filling in a Mott insulator, at very low temperatures.

We can also use the Hubbard model to explain certain kinds of magnetism. The Stoner model of ferromagnetism can be derived from the Hubbard model using a mean field approximation [34]. Also for a finite U , the Hubbard model ground state shows antiferromagnetic ordering at half-filling. However, a ferromagnetic phase arises slightly away from half-filling at strong enough coupling (U) in two or three dimensions (but not in one dimension) [35]. Further doping away from half-filling eliminates any magnetic ordering. We discuss one form of ferromagnetism arising slightly way from half-filling in two dimensions (Nagaoka ferromagnetism [36]) in chapter 5.

One can derive the Heisenberg model of spin-spin interaction from the Hubbard model in the limit of $U \gg t$. Hopping of electrons through the lattice is energetically suppressed in this limit. Using hopping as a perturbation on the dominant Coulomb repulsion, we can see that the effective Hamiltonian only consists of spin-spin interactions [37]. This spin-spin interaction is used to perform gate-operations for experiments with spin-qubits [38].

These diverse applications have made the Hubbard model one of the most active research topics in condensed matter physics. Unfortunately, the solution to this model becomes intractable with increasing lattice size. Physicists have studied this model using a wide range of analytic and numerical techniques in the last few decades. A more recent approach is to study the Hubbard model using analog quantum simulation [12, 39–43]. Most of these simulation experiments have been performed using ultracold atoms so far. We discuss the capability of gate-defined quantum dot arrays to mimic the fermionic Hubbard model in the next subsection.

2.3. SIMILARITIES BETWEEN THE FERMI-HUBBARD MODEL AND GATE-DEFINED QUANTUM-DOT ARRAYS

A gate-defined quantum dot array has properties largely similar to those described in the Hubbard model [44–49]. The confinement potential of each quantum-dot plays the role of an atomic potential in the model to create a single site. The control over the fabrication process allows us to create a regular array of these dots. Moreover, we can restrict gate-voltages to only allow a maximum of two electrons per dot. Combining all these attributes, a quantum-dot array can be programmed to mimic the assumptions of the Hubbard model, with some modification.

Table 2.1: Typical energy scales for Hubbard parameters in a gate-defined quantum-dot array

Energy Term	Typical Values in a quantum-dot array (meV)
t_{ij}	0 - 0.5
μ_i	0 - 15
U_i	1 - 3
V_{ij}	0 - 1

Next, we examine the similarities between the energy terms. The Hubbard model has three energy terms, namely U , t , and μ (see Eqs. 2.5). The Coulomb on-site interaction between two electrons in the same dot plays the role of U in the quantum-dot arrays. Unlike the atomic lattice, not all quantum-dots are nominally identical. The values of U thus become site-dependent and we replace U by U_i to modify the model accordingly. The role of hopping (t) is played by the tunnel-coupling between two dots. This tunnel-coupling is governed by the overlap of electron wave-functions between the two dots. Each quantum dot also has a local energy offset which controls the electron filling of the dot, similar to the Hubbard model μ . Both t and μ are also site dependent for quantum dot arrays and are replaced by t_{ij} ($= t_{ji}^*$) and μ_i respectively. However, unlike the Hubbard model, we cannot ignore the interaction between electrons in different dots. We extend the Hamiltonian to incorporate this inter-site interaction (V_{ij}). This is the energy penalty to add one additional electron to dot i , due to the presence of an electron in dot j or vice versa. The resultant model, with the extra energy term, is typically known as the extended Hubbard model. The effective Hamiltonian for our system can be written as:

$$H = - \sum_{\langle i,j \rangle, \sigma} t_{ij} \left[c_{i\sigma}^\dagger c_{j\sigma} + h.c. \right] - \sum_i \mu_i n_i + \sum_i U_i n_{i\uparrow} n_{i\downarrow} + \sum_{i,j} V_{ij} n_i n_j \quad (2.6)$$

The first two energy terms (t_{ij} and μ_i) of Eqs. 2.6 can be tuned in a quantum-dot array using gate voltages. Whereas, the values of the final two terms (U_i and V_{ij}) are not gate-tunable, but these can be measured quite accurately. These values mainly depend on the shapes and positions of the dots and stay rather constant once the dots are formed. The typical values observed for these energy terms are shown in Table 2.1. We note that the range of 0 – 15 meV for μ_i is actually the range over which the local energy

of a quantum dot can be tuned. The energy offset required to load two electrons into an empty band of a dot is lower than this range. So, strictly from the Hubbard model perspective, we have full control over μ_i to go from an empty to a full band. Moreover, the quantum dots are operated at a dilution temperature, where the thermal energy (kT) is less than 0.01 meV . As a result, the system can be tuned to have all other energies significantly larger than the thermal energy. This tunable access to a large range of parameters potentially enables us to simulate the Fermi-Hubbard model using quantum dot arrays. We show an example of this tunability in a 2x2 quantum-dot array in chapter 4.

Table 2.2: Typical control of Fermi-Hubbard parameters achieved using quantum dot arrays [12, 50] and ultracold atom lattices [39–43]

Platform	U/t	t/kT
Arrays of gate defined quantum dots	$\mathcal{O}(1) - \mathcal{O}(100)$	$\mathcal{O}(1) - \mathcal{O}(10)$
Lattices of ultracold atoms	$\mathcal{O}(1) - \mathcal{O}(10)$	$\mathcal{O}(0.1) - \mathcal{O}(1)$

Finally, we compare the quantum dot arrays to the ultracold atom lattices for their capacities to simulate the Fermi-Hubbard model. The main (dis)advantages of the two platforms in this regard are discussed below:

1. It is desirable to have access over a large range of U/t values while keeping the thermal energy (kT) as low as possible with respect to hopping (t). Table 2.2 shows that the quantum dot arrays currently have more tunability in U/t and higher values of t/kT , compared to the ultracold atoms. These make the quantum dot arrays potentially better equipped to probe a larger range of the Fermi-Hubbard phase space, including the low-temperature regime that is of highest interest.
2. Control over the chemical potential (μ) enables us to dope the system away from half-filling. This is essential to explore several exotic phases of the Hubbard model, such as superconductivity and certain forms of ferromagnetism. Experiments using both platforms have demonstrated the desired control over μ .
3. The size of the quantum simulator is another important feature. For small system sizes, the simulation results can also be reproduced numerically. This becomes increasingly difficult and eventually impossible with larger systems. Scaling up the number of sites in a lattice has been easier with ultracold atoms so far. The intrinsic disorders in the 2DEG make it difficult to create and manipulate large arrays of quantum dots. The largest quantum dot arrays reported so far contain eight [51] and nine dots [52, 53]. Whereas, the Fermi-Hubbard model has been simulated on a two-dimensional square lattice of ~ 80 sites using ultracold atoms [43].

BIBLIOGRAPHY

- [1] M. T. Björk, C. Thelander, A. E. Hansen, L. E. Jensen, M. W. Larsson, L. R. Wallenberg, and L. Samuelson, *Nano Letters* **4**, 1621 (2004).

- [2] Y. Hu, H. O. H. Churchill, D. J. Reilly, J. Xiang, C. M. Lieber, and C. M. Marcus, *Nature Nanotechnology* **2**, 622 (2007).
- [3] G. A. Steele, G. Gotz, and L. P. Kouwenhoven, *Nature Nanotechnology* **4**, 363 (2009).
- [4] R. J. Warburton, *Nature Materials* **12**, 483 (2013).
- [5] J. Park, A. N. Pasupathy, J. I. Goldsmith, C. Chang, Y. Yaish, J. R. Petta, M. Rinkoski, J. P. Sethna, H. D. Abruña, P. L. McEuen, and D. C. Ralph, *Nature* **417**, 722 (2002).
- [6] L. P. Kouwenhoven, C. M. Marcus, P. L. McEuen, S. Tarucha, R. M. Westervelt, and N. S. Wingreen, "Electron transport in quantum dots," in *Mesoscopic Electron Transport*, edited by L. L. Sohn, L. P. Kouwenhoven, and G. Schön (Springer Netherlands, Dordrecht, 1997) pp. 105–214.
- [7] R. Hanson, L. P. Kouwenhoven, J. R. Petta, S. Tarucha, and L. M. K. Vandersypen, *Rev. Mod. Phys.* **79**, 1217 (2007).
- [8] M. Field, C. G. Smith, M. Pepper, D. A. Ritchie, J. E. F. Frost, G. A. C. Jones, and D. G. Hasko, *Phys. Rev. Lett.* **70**, 1311 (1993).
- [9] C. Barthel, M. Kjærgaard, J. Medford, M. Stopa, C. M. Marcus, M. P. Hanson, and A. C. Gossard, *Phys. Rev. B* **81**, 161308 (2010).
- [10] T. Ito, T. Otsuka, S. Amaha, M. R. Delbecq, T. Nakajima, J. Yoneda, K. Takeda, G. Allison, A. Noiri, K. Kawasaki, and S. Tarucha, *Scientific Reports* **6**, 39113 (2016).
- [11] K. C. Nowack, M. Shafiei, M. Laforest, G. E. D. K. Prawiroatmodjo, L. R. Schreiber, C. Reichl, W. Wegscheider, and L. M. K. Vandersypen, *Science* **333**, 1269 (2011).
- [12] T. Hensgens, T. Fujita, L. Janssen, X. Li, C. J. Van Diepen, C. Reichl, W. Wegscheider, S. Das Sarma, and L. M. K. Vandersypen, *Nature* **548**, 70 (2017).
- [13] A. Abragam, *The principles of nuclear magnetism*, 32 (Oxford university press, 1961).
- [14] D. Paget, G. Lampel, B. Sapoval, and V. I. Safarov, *Phys. Rev. B* **15**, 5780 (1977).
- [15] A. V. Khaetskii, D. Loss, and L. Glazman, *Phys. Rev. Lett.* **88**, 186802 (2002).
- [16] F. H. Koppens, J. A. Folk, J. M. Elzerman, R. Hanson, L. W. Van Beveren, I. T. Vink, H.-P. Tranitz, W. Wegscheider, L. P. Kouwenhoven, and L. M. Vandersypen, *Science* **309**, 1346 (2005).
- [17] G. Dresselhaus, *Phys. Rev.* **100**, 580 (1955).
- [18] Y. A. Bychkov and É. I. Rashba, *JETP lett* **39**, 78 (1984).
- [19] P. Scarlino, E. Kawakami, P. Stano, M. Shafiei, C. Reichl, W. Wegscheider, and L. M. K. Vandersypen, *Phys. Rev. Lett.* **113**, 256802 (2014).
- [20] A. V. Khaetskii and Y. V. Nazarov, *Phys. Rev. B* **61**, 12639 (2000).

- [21] A. V. Khaetskii and Y. V. Nazarov, *Phys. Rev. B* **64**, 125316 (2001).
- [22] K. Ono, D. G. Austing, Y. Tokura, and S. Tarucha, *Science* **297**, 1313 (2002) .
- [23] W. Pauli, *Phys. Rev.* **58**, 716 (1940).
- [24] A. C. Johnson, J. R. Petta, J. M. Taylor, A. Yacoby, M. D. Lukin, C. M. Marcus, M. P. Hanson, and A. C. Gossard, *Nature* **435**, 925 (2005).
- [25] F. H. L. Koppens, C. Buizert, I. T. Vink, K. C. Nowack, T. Meunier, L. P. Kouwenhoven, and L. M. K. Vandersypen, *Journal of Applied Physics* **101**, 081706 (2007).
- [26] P. Harvey-Collard, B. D'Anjou, M. Rudolph, N. T. Jacobson, J. Dominguez, G. A. Ten Eyck, J. R. Wendt, T. Pluym, M. P. Lilly, W. A. Coish, M. Pioro-Ladrière, and M. S. Carroll, *Phys. Rev. X* **8**, 021046 (2018).
- [27] A. Sommerfeld, *Zeitschrift für Physik* **47**, 1 (1928).
- [28] J. C. Slater and G. F. Koster, *Phys. Rev.* **94**, 1498 (1954).
- [29] J. Hubbard, *Proceedings of the Royal Society of London. Series A. Mathematical and Physical Sciences* **276**, 238 (1963).
- [30] C. Chen, *Physica B: Condensed Matter* **206-207**, 729 (1995), proceedings of the International Conference on Strongly Correlated Electron Systems.
- [31] P. W. Anderson, *Journal of Physics: Conference Series* **449**, 012001 (2013).
- [32] M. Imada, A. Fujimori, and Y. Tokura, *Reviews of modern physics* **70**, 1039 (1998).
- [33] P. A. Lee, N. Nagaosa, and X.-G. Wen, *Reviews of modern physics* **78**, 17 (2006).
- [34] A. Mielke and H. Tasaki, *Communications in mathematical physics* **158**, 341 (1993).
- [35] D. C. Mattis, *The theory of magnetism I: statics and dynamics*, Springer series in solid-state sciences (Springer, 1981).
- [36] Y. Nagaoka, *Phys. Rev.* **147**, 392 (1966).
- [37] C. L. Cleveland and R. Medina A, *American Journal of Physics* **44**, 44 (1976).
- [38] D. Loss and D. P. DiVincenzo, *Physical Review A* **57**, 120 (1998).
- [39] R. Jördens, N. Strohmaier, K. Günter, H. Moritz, and T. Esslinger, *Nature* **455**, 204 (2008).
- [40] M. E. Parsons, A. Mazurenko, C. S. Chiu, G. Ji, D. Greif, and M. Greiner, *Science* **353**, 1253 (2016).
- [41] M. Boll, T. A. Hilker, G. Salomon, A. Omran, J. Nespolo, L. Pollet, I. Bloch, and C. Gross, *Science* **353**, 1257 (2016).

- [42] L. W. Cheuk, M. A. Nichols, K. R. Lawrence, M. Okan, H. Zhang, E. Khatami, N. Trivedi, T. Paiva, M. Rigol, and M. W. Zwierlein, *Science* **353**, 1260 (2016).
- [43] A. Mazurenko, C. S. Chiu, G. Ji, M. F. Parsons, M. Kanász-Nagy, R. Schmidt, F. Grusdt, E. Demler, D. Greif, and M. Greiner, *Nature* **545**, 462 (2017).
- [44] C. A. Stafford and S. Das Sarma, *Phys. Rev. Lett.* **72**, 3590 (1994).
- [45] E. Manousakis, *Journal of Low Temperature Physics* **126**, 1501 (2002).
- [46] L. Gaudreau, S. A. Studenikin, A. S. Sachrajda, P. Zawadzki, A. Kam, J. Lapointe, M. Korkusinski, and P. Hawrylak, *Phys. Rev. Lett.* **97**, 036807 (2006).
- [47] T. Byrnes, N. Y. Kim, K. Kusudo, and Y. Yamamoto, *Phys. Rev. B* **78**, 075320 (2008).
- [48] S. Yang, X. Wang, and S. Das Sarma, *Phys. Rev. B* **83**, 161301 (2011).
- [49] P. Barthelemy and L. M. K. Vandersypen, *Annalen der Physik* **525**, 808 (2013).
- [50] U. Mukhopadhyay, J. P. Dehollain, C. Reichl, W. Wegscheider, and L. M. K. Vandersypen, *Applied Physics Letters* **112**, 183505 (2018).
- [51] C. Volk, A. M. J. Zwerver, U. Mukhopadhyay, P. T. Eendebak, C. J. van Diepen, J. P. Dehollain, T. Hensgens, T. Fujita, C. Reichl, W. Wegscheider, and L. M. K. Vandersypen, *npj Quantum Information* **5**, 29 (2019).
- [52] P.-A. Mortemousque, E. Chanrion, B. Jadot, H. Flentje, A. Ludwig, A. D. Wieck, M. Urdampilleta, C. Bäuerle, and T. Meunier, *arXiv preprint arXiv:1808.06180* (2018).
- [53] A. R. Mills, D. M. Zajac, M. J. Gullans, F. J. Schupp, T. M. Hazard, and J. R. Petta, *Nature Communications* **10**, 1063 (2019).

3

DEVICE FABRICATION AND EXPERIMENTAL SETUP

This chapter discusses the procedure for device fabrication and describes details of the experimental setups that were used to obtain the results in the next two chapters.

3.1. DEVICE FABRICATION

As discussed in chapter 1, most measurements involving quantum dot arrays have so far been performed with linear arrays with a few quantum dots. In this section, I discuss our fabrication effort to scale up these quantum dot arrays. We have developed recipes to fabricate a small 2D array of four dots in 2x2 geometry and a linear eight-dot array. We start with a general description of the steps used to fabricate these samples. Most of these steps are quite standard and can also be found in previous works from our group [1]. I include them here for the sake of completion. This is followed by the new developments made during the course of this dissertation. Full fabrication recipes for both devices can be found in Appendix A.

3.1.1. OVERVIEW OF THE FABRICATION STEPS

The following steps are needed to make samples on a substrate received from the growers:

- Both devices were fabricated on similar substrates with GaAs/AlGaAs heterostructures. These substrates have a coating of Gallium (Ga) paste on the back surface. Ga is used as an adhesive, while the heterostructure is grown in a molecular-beam epitaxy (MBE) system to create a 2DEG. Cleaning this Ga is the very first and a crucial step of any fabrication run. If left on the wafer, Ga contaminates not only the sample under fabrication but also the machines used in the fabrication run. Wet etching in hot, diluted hydrochloric acid (HCl) is used to remove this layer of Ga. But HCl can also destroy the heterostructure. To prevent this, the top surface of the substrate is protected with a few μm thick spin-coated photo-resist (S1813). The clean wafer is then diced into smaller pieces for individual fabrication runs, with the resist still on it. Before starting an individual run, the photo-resist is finally stripped in acetone.
- Each individual run starts with the deposition of titanium/gold (Ti/Au) alignment markers. These markers are patterned with electron-beam (ebeam) lithography and are later used to align the subsequent layers in ebeam steps. Moreover, they define the boundary of a device unit-cell.
- In the next step, a mesa pattern is defined and etched to remove the 2DEG from all the unnecessary places. The 2DEG is only needed to create dots, electron reservoirs, and ohmic connections to the reservoirs. This etching of GaAs/AlGaAs is performed using diluted Piranha solution (1:8:240 $\text{H}_2\text{SO}_4:\text{H}_2\text{O}_2:\text{H}_2\text{O}$) yielding etch rates of roughly 4 nm/s. The mesa disconnects the ohmic contacts from one another, as well as reduces the probability of leakage between the large gates and the 2DEG.
- This is followed by the creation of the ohmic contacts to the reservoirs. A metal layer consisting of nickel/gold-germanium/nickel (Ni/AuGe/Ni) is deposited, which diffuses through the heterostructure and connects to the 2DEG when annealed in forming gas environment. These ohmic contacts are used to voltage-bias the reservoirs and to measure current through the quantum dots.

- The next step is to pattern the fine gates. The quantum dots are created by depleting electrons from the 2DEG using voltages on these gates. As a result, the design of this gate structure determines the shape of the resulting dot array. Depending on the dot-array, this step might contain several layers and materials. The details of the fine gate structures for individual arrays are discussed in the following subsections.
- Finally, we create the large gates, which are made of Ti/Au. These gates extend the fine gates and create bond-pads where external wire-bonds can be connected.

After the fabrication steps, a typical chip contains nine unit-cells. These cells can have either the same or different dot-arrays. The finished chip is then covered with photo-resist and diced into individual device unit-cells. The devices are then cleaned in acetone and stored in a vacuum desiccator. Before measurement, one such device is glued on a printed circuit board (PCB) using concentrated PMMA (polymethyl methacrylate - an ebeam resist) for wire-bonding.

3.1.2. FINE GATE STRUCTURE OF 2X2 DOT ARRAY

As we discussed before, the shape of a quantum dot array is defined by the fine gate structure. Here we discuss the developments made to fabricate the fine gate structure of a 2x2 dot array. The quantum-dot community is well experienced in controlling small linear arrays. The 2x2 array, the simplest form of 2D array, is a first step towards eventually scaling up to larger arrays. Our aim is to make a 2x2 dot array with extensive control over the desired parameters, as described in chapter 2.

Initially, a slightly modified version of the well-tested linear array gate-design was explored to make this dot array. Fig. 3.1(a) shows a scanning electron microscope (SEM) image of one such device, with expected positions of the dots and reservoirs. In this design, all the gates exist on the same 2D plane, similar to the previous effort to make a 2x2 dot array [2].

Initial experiments using these devices showed limited, if any, potential to access the desired values for different tunnel couplings in the dot array. We postulate that only low tunnel couplings can be achieved using these devices. The four dots will tend to merge into a single dot as these couplings are increased, as there is no gate to stop this merging. We haven't tested this prediction with experiments. Controlling the desired parameters of the dot array is also rather difficult in these devices due to the lack of individual control knobs. For example, to increase the tunnel coupling between dots 2 and 3, the voltage on gate C_2 needs to be increased. But, this in turn also increases the tunnel coupling between dots 1 and 4. Although cross-capacitance between the gates and the dots can be used to partially compensate for these effects, it severely restricts the access to the parameter-space.

To overcome these problems, we introduce a modified design with one extra gate, D_0 (Fig. 3.1(b)). This gate is needed to separate the four dots, as well as have an individual tuning knob for all nearest-neighbour tunnel couplings. Although the new design looks rather similar to the previous one at first glance, there is a fundamental difference in terms of fabrication between these two gate structures. Unlike all the other gates, the D_0 gate cannot be routed via the same 2D plane without affecting the dot-system. Any

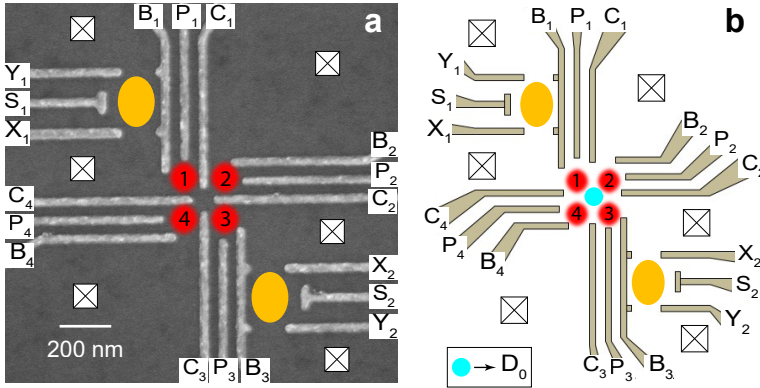


Figure 3.1: (a) SEM image of a device made using the first gate design. (b) Schematic diagram of the second gate design. In both figures, the red circles represent the main dot array, whereas the yellow ellipses show the position of the sensing dots. Both devices contain six electron reservoirs for the quantum dots, each of which is marked with a cross in a square.

voltage applied to the gate D_0 will equally influence not only the center of the four dot system but also under the lead up to the gate. This will either stop us from making one of the four dots or significantly reduce the coupling between two neighbouring dots, depending on the position of the lead.

One way to circumvent this issue is to bring the D_0 gate from a different plane, sufficiently away from the heterostructure surface, and contact the surface only at the center of the dot-array. This can significantly reduce the effect of D_0 at unwanted places. This effect may be further reduced if the lead to the center gate goes over another gate, which runs on the surface. In this case, the potential on the 2DEG will be screened from the voltage on the lead by the voltage on the gate below it. Both these outcomes can be achieved by introducing a double layer gate-design with a dielectric between the layers. This dielectric layer should electrically isolate the D_0 gate from all the gates in bottom layer. Here, the main challenge is to figure out a way to have the D_0 gate run over the dielectric and land on the substrate only at the center of the array.

We considered several approaches, such as wet/dry etch of aluminum oxide (Al_2O_3) and fabrication of an air-bridge, to create the double-layer gate structure. Eventually, we used a slab of silicon nitride (SiN_x) as the dielectric layer. In this approach, the fine gate structure is created in three steps. The schematics of these three layers are shown in Fig. 3.2(a-c) respectively. Fig. 3.2(d-f) show the SEM images of the same layers. In the first step, all gates except D_0 are fabricated using 5/20 nm thick Ti/Au on the bare substrate. This is followed by the lift-off of a sputtered SiN_x slab on top of the gates C_3 and P_3 . This slab is 50 nm thick, 200 nm wide and 1.5 μm long. Finally, the D_0 gate is deposited using lift-off of 10/100 nm thick Ti/Au. This gate runs over the gate C_3 before contacting the substrate. The alignment of these three layers is crucial for proper operation of the device. Bringing the markers close to the fine gate structure and using different markers for each of the three steps, we could align with only a few nanometers of error between layers using the ebeam machine (Raith EBPG5200) in Kavli nanolab, Delft.

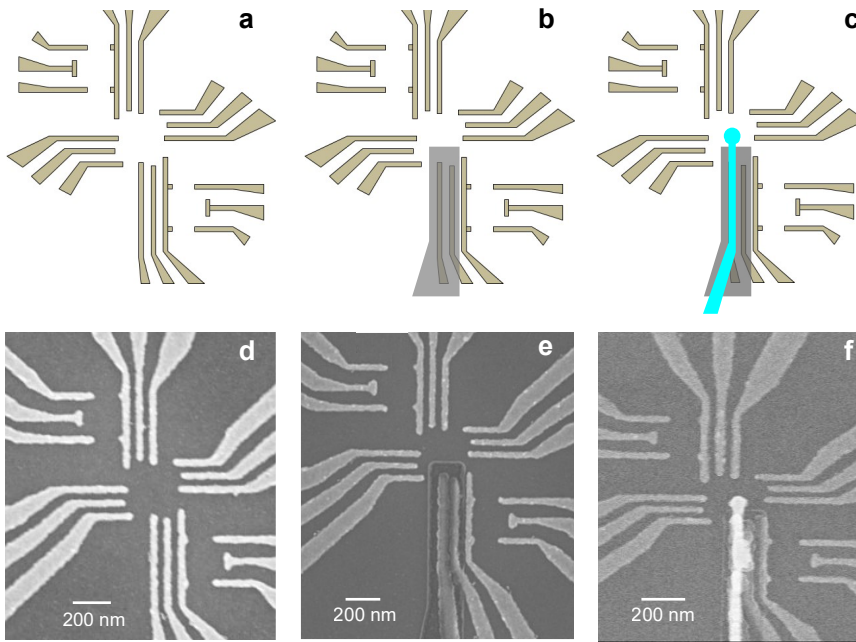


Figure 3.2: [(a)-(c)] Design schematic of the three steps to create the fine gate structure for the 2x2 dot array. The gates in the first layer (golden) are created first, followed by the SiN_x slab (grey). Finally the D_0 gate (cyan) is deposited over the SiN_x slab, contacting the bare substrate at the center of the structure. [(d)-(f)] SEM images of a device, nominally identical to the one used for measurements, after each fabrication step shown in (a)-(c) respectively.

The lift-off of SiN_x is a non-trivial step, which required quite a bit of recipe development. A lift-off process is generally used for making patterns with metals deposited using evaporation technique. Because of the specific direction of deposition, evaporation can reduce step-coverage of the resist mask. This, in turn, helps in lifting off the metals from unwanted regions. However, all the available dielectric deposition techniques result in a much better step-coverage than metal evaporation. This makes lift-off of dielectrics rather difficult. Fortunately, the stress present in the films allows us to use the lift-off process successfully for sputtered SiN_x . Due to the step-coverage from sputtering, SiN_x covers the sidewall of the resist and produces standing-edges at the boundary of the dielectric slab. The height of such an edge is equal to the resist thickness, which is generally taller than the SiN_x slab. These standing-edges create a potential problem for the following step. The chance of the D_0 gate breaking, while crawling over a standing-edge, increases with the height difference between the slab and the edge.

Although it is almost impossible to completely eliminate these SiN_x edges, their heights can be controlled by optimizing the fabrication recipe. As discussed earlier, the heights of these edges depend on the height of the resist used for lift-off. After optimizing, an 80 nm thick single layer AR-P 6200.08¹ resist is used to lift-off 50 nm thick SiN_x . The result-

¹Csar 62 (AR - P 6200), <http://www.allresist.com/csar-62-ar-p-6200/>

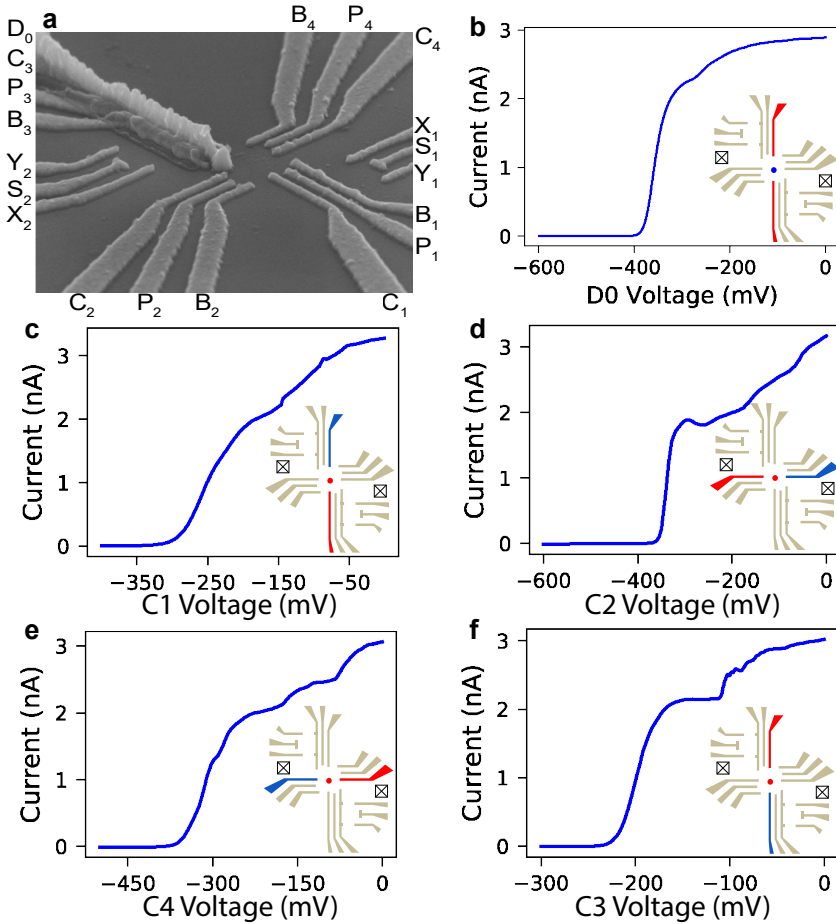


Figure 3.3: (a) Tilted SEM image of a lithographically identical device to the one measured, showing the continuity of the D_0 gate. (b) Pinch-off of the current channel through the center of the device using negative voltage in the D_0 gate, confirming its continuity electrically. [(c)-(f)] Current pinch-off through the same channel with all four C gates. For (b)-(f), the measured current runs between the two reservoirs marked (X in a box) in the device schematic shown in respective insets. In each of the schematics, the voltage on the blue gate is varied during measurement, whereas the two red gates are biased sufficiently with negative voltage to assist the pinch-off. All the other gates are connected to ground during these measurements.

ing edge is only a few tens of nm higher than the slab. This can be successfully covered by making the D_0 gate with 10/100 nm of Ti/Au. Fig. 3.3(a) shows a tilted SEM image of the three-layer fine gate structure. Here the D_0 gate is seen to be going over the C_3 gate before contacting the substrate at the center without any sign of breakage.

Once all three layers looked good in scanning electron microscopy, we performed electrical measurements at dilution temperature to check if the device can be used to make the 2×2 dot array, as expected. First, the leakage between gates D_0 and C_3 (P_3) was measured, which showed no leakage up to a difference of 2 V between the gates. This showed that the SiN_x dielectric slab successfully separates the gates of two different layers. Next, we checked the electrical continuity of the D_0 gate. Fig. 3.3(b) shows how the current between the two indicated reservoirs is pinched-off by applying a negative voltage to D_0 . Finally Fig. 3.3(c-f) show how the same current channel can be pinched off independently by all C gates.

All these results together indicate that the device design can be used to create a 2×2 dot array with extensive control over desired parameters, especially the tunnel coupling between all pairs of double-dots. In chapters 4 and 5, I will discuss experimental results using a 2×2 dot array device of this design.

3.1.3. FINE GATE STRUCTURE OF AN EIGHT-DOT LINEAR ARRAY

The fine gate structure used for the eight-dot linear array is a direct extension of the four dot array measured before [3, 4]. Fig. 3.4(a) shows this gate structure with the expected dot positions. In this thesis, I will only discuss the fabrication of these devices, not the results obtained using them. The devices are currently being measured, and the first results about electron-filling and controlling one such eight-dot array have already been reported [5].

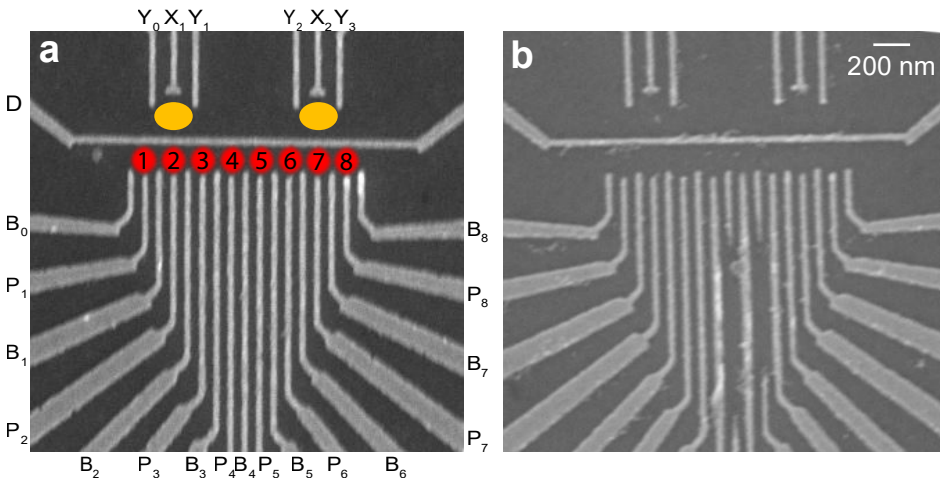


Figure 3.4: (a) An SEM image of an eight-dot linear array device. The red circles show the intended location of the eight dots of the array, whereas the yellow ellipses indicate the sensing dot locations. (b) SEM image of a similar device with broken gate structure.

The main challenge here is to create seventeen gates (B_0 to B_8) parallel to each other with 80 nm pitch. A common problem is to have one or a few of these gates partially broken (see Fig. 3.4(b)). Note where one gate is broken, the two neighbouring gates are wider than the rest. We think this is caused by the collapse of the e-beam resist-walls before the metal deposition. The probability of such a collapse increases with increasing height and decreasing width of the walls. As the widths are fixed by design, the solution is to use a thinner resist layer. A common practice is to optimize the fine-gate structure recipe without the other fabrication steps, and then use that recipe to make final devices with all steps. Initially, this led to nice looking structures for test runs and broken gates in actual devices. After careful investigation, it was found that the thickness of the resist layer is affected by the mesa structure mentioned in subsection 3.1.1. While using the same recipe, the resist was systematically thicker for substrates with mesa. So we optimized the resist-thickness on substrates with mesa to solve the problem.

3.1.4. PRACTICAL TIPS AND TRICKS FOR SAMPLE SELECTION, HANDLING, AND BONDING

- In the final fabrication run, we found the device yield to be roughly 50%. To avoid a lot of unwanted wire-bonding, it is better to select samples with intended fine gate structures. Although we can image the samples in SEM for this selection, it is feared that the high-velocity electrons may induce charge traps and this can deteriorate the device performance. We can image the samples with an atomic force microscope (AFM) instead, using tapping mode in air, which is not expected to harm the sample. The AFM images have enough resolution to aid in the selection of a good device, which can be seen in Fig. 3.5(a-b).

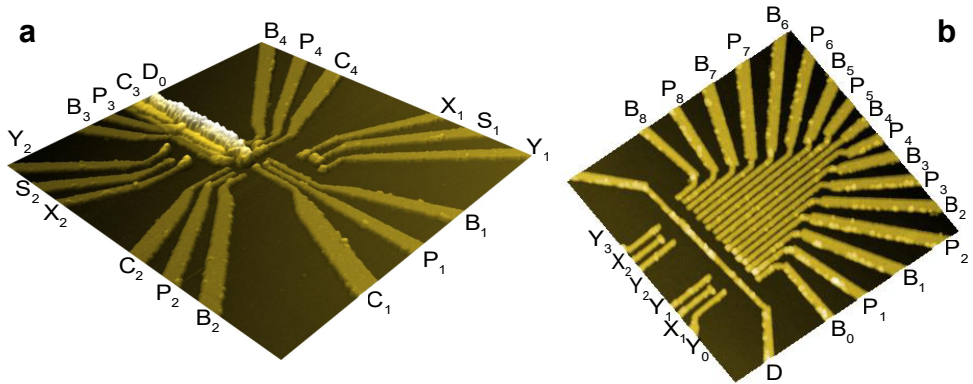


Figure 3.5: (a) AFM image of the 2x2 device measured. (b) AFM image of a linear eight-dot array.

- Utmost care should be taken while carrying and wire-bonding a sample to avoid blowing up the fine gate structure due to electrostatic discharge (ESD). Note that, once a wire is attached to a bond-pad of a sample, it should not be taken off, as this drastically increases the probability of ESD. If the other side of the wire does not contact the PCB, the dangling wire should be pressed to the PCB bond-pad

using the wedge tool, to complete the bond. Samples should always be carried in an ESD-safe box, and once bonding is done, the gates should be grounded through the PCB.

- Although the performance of the gates cannot be tested at room temperature, the ohmic connections to the reservoirs should be tested before a device is cooled down. For working devices, the typical resistance measured between two ohmics is around 100 k Ω .

3.2. EXPERIMENTAL SETUP

Here I describe the experimental setup used to perform measurements reported in chapters 4 and 5. The experimental setup is divided into two main subsections: the dilution refrigerator to cool down the devices and the electronics to control and measure them.

3.2.1. DILUTION REFRIGERATOR

Due to the three dimensional confinement, the energy levels of quantum dots are discretized. To trap electrons in these levels and avoid thermal excitation, experiments are typically performed in dilution refrigerators. Both the 2x2 and eight-dot linear array devices are cooled down in a Bluefors XLD-400 dry fridge simultaneously using a homemade cold-finger attached to the mixing chamber (MC) plate. Fig. 3.6(a-b) show different parts of the fridge used. The base temperature of the fridge reaches below 7 mK with constant voltages on the gates. However, this temperature can rise up to 30 mK, when voltage pulses are applied to several gates. Although the phonons in the substrate should reach the base temperature, the electrons in the 2DEG remain at a higher temperature. This is due to thermal and electrical contact of the 2DEG to the warmer parts of the fridge through measurement wiring and due to electrical noise coupling in from the instrumentation. The wires are electrically filtered and thermally contacted to different plates in the fridge to reduce this electron temperature. Ideally, a radiation shield is also connected to the MC plate to protect the samples from higher temperature radiation. The fridge has a uniaxial superconducting magnet, which can provide fields up to 3 T. To apply a magnetic field perpendicular to the plane of the 2x2 dot array, we had to remove the MC radiation shield in order to create room to mount the sample PCB horizontally. As a result, the samples are subjected to radiation from the can attached to the still plate, which typically has a temperature of 800 mK.

3.2.2. CONTROL AND MEASUREMENT ELECTRONICS

The electronics used are designed to allow for fast control and readout while minimizing unwanted back action on the system. Here we categorize them into four different parts described below.

1. PRINTED CIRCUIT BOARD

A printed circuit board (PCB) (Fig. 3.6(c)) is used to connect a device to the control and measurement lines in the fridge. The sample is glued to the center of the PCB using concentrated PMMA, which is then attached on to the cold-finger for thermal anchoring.

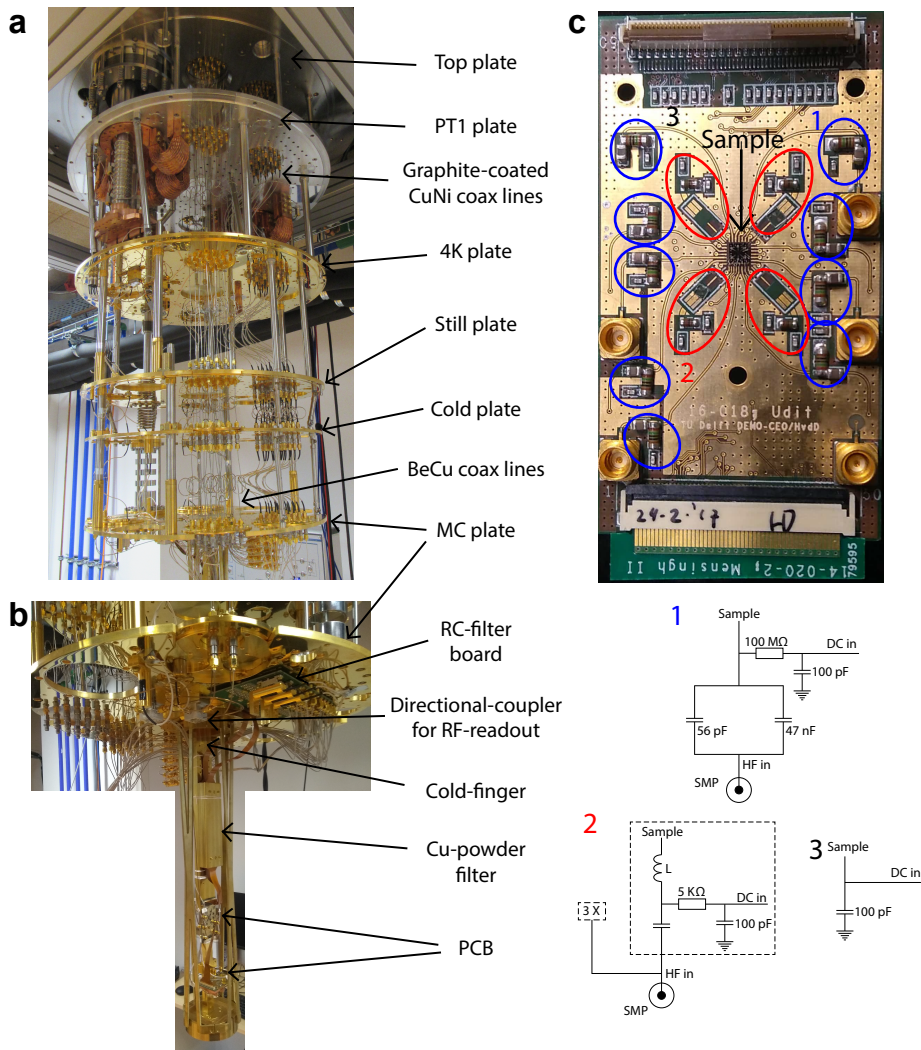


Figure 3.6: (a) Inside of the Bluefors XLD-400 dry fridge from top plate to mixing chamber plate. (b) Bottom of the MC plate and the Cold-finger attached to it. (c) PCB used to cool down the 2x2 dot device. The PCB has nine high-frequency lines (1), each combined with a DC line using a bias-tee. The RF-readout line (2) is split in four, each of which has a DC line connected through a bias-tee. Individual inductances of different inductance need to be connected to these lines to use them for RF-readout via frequency multiplexing. Finally, DC lines are filtered with 100 pF capacitance (3) to ground.

There are 48 DC lines in the PCB to apply voltage bias on the gates. The device bond-pads are electrically connected to these lines via wire-bonds. The lines are connected to two FFC connectors in parallel, one connector to keep the gates on the device grounded while connecting them to the DC wires in the fridge using the other connector.

Moreover, the PCB has nine high-frequency (HF) co-planar wave-guides, which can be connected to coax lines in the fridge through SMP connectors. Each HF line is combined with a DC line using a bias-tee with an RC time constant of ~ 470 ms. Using these lines, fast voltage pulses can be applied to selected gates on the sample to aid in tuning and measurement. To minimize high-frequency cross-talk, each DC line is filtered with a 100 pF capacitor to ground.

Finally, there is another HF wave-guide in the PCB used for RF reflectometry. This wave-guide is split into four readout lines, each containing an LC-tank circuit. Each readout line is coupled with a DC line using a bias-tee and is connected to one reservoir per sensing dot. RF reflectometry enables us to measure the conductance of the individual sensing dots simultaneously using frequency multiplexing. The details of this method are discussed later in this chapter.

2. DC ELECTRONICS

The DC electronics serve two main purposes in the experimental setup.

1. To apply bias voltages to the nano-fabricated gates to create the quantum dots.
2. To measure the DC current between two electron reservoirs, through single or multiple quantum dots.

The gates are biased using digital to analog converter (DAC) modules. The modules can apply voltages from -4 V to 4 V with a $60 \mu\text{V}$ resolution. Currents through the quantum dots are measured using an I-V converter connected to one reservoir adjacent to the dot, while a bias ($\sim 100 \mu\text{V}$) is applied to the other adjacent reservoir. The DC control and measurement modules are battery powered and isolated from other instruments, which are connected to the 50 Hz power line. The DACs and the measurement computer communicate with each other using optical cables.

As mentioned before, there are 96 DC lines distributed equally between the two PCBs. Inside the fridge, two different kinds of lines are used to carry DC signal from the top-plate to the mixing chamber plate: thermocoax lines (24 pieces) and phosphor-bronze looms (3 looms). Each of these looms contains 24 DC lines. The lines in a phosphor-bronze loom are connected to a matrix module² outside the fridge using a 24-pin Fischer cable. Each of these lines goes through a Pi-filter³ in the matrix module to filter out high-frequency components and provide a ripple-free DC voltage. The thermocoax lines are connected to individual coax lines outside the fridge. The other end of each of these coax lines connects to a low-pass filter (DC - 2.5 MHz)⁴, which is attached to the output of the matrix module. All 96 lines are connected to a home-made RC-filter board, attached to the mixing chamber plate inside the fridge. They are filtered with a second-order RC

²For details of this module, see: <http://qwork.tudelft.nl/~schouten/matrix/index-matrix.htm>

³For details, see: <http://qwork.tudelft.nl/~schouten/sampwfilters/index-sampwfilters.htm>

⁴Mini-Circuits SLP-2.5+

filter having cutoff frequency of either 5 Hz (for lines connected to gates) or 150 kHz (for lines connected to reservoirs). The output of this RC-filter board has two 50-pin FFC connectors, one for each PCB in the fridge. Depending on the specific placement of gates and reservoirs in a sample, the filter frequency of each line is chosen. So, a different filter board might be required for a new sample. Each set of lines then goes through a Cu-powder filter⁵, attached to the cold-finger, before connecting to a PCB. The Cu-powder filter is used to filter out signals with very high frequency (from few 10s up to 100s of GHz), where other filters don't work well. 50 pin FFC cables are used to connect the RC filter board to Cu-powder filter and Cu-powder filter to PCB.

3. RF CONTROL ELECTRONICS

In experiments with quantum dots, RF control electronics is typically used for the following purposes:

1. To apply microwave (MW) excitation (up to 40 GHz) to the sample for qubit operations, photon-assisted tunneling etc.
2. To apply fast voltage pulses (with nanoseconds rise-time) on the gates to rapidly change chemical potentials of different dots.
3. To ramp gate voltages (with a time-period of milliseconds) for fast mapping of charge stability diagrams.

Microwave excitations are generally applied with MW-sources. No microwave excitation was required in our experiments. Arbitrary waveform generators (AWG): Tektronix AWG5014C are used for both pulsing and ramping gate voltages. The output of each AWG channel is connected to a flexible coax cable, which is wrapped around a ferrite-core before connecting to an HF line in the fridge. The ferrite-core introduces a high impedance for the ground loop current passing through the coax, while not affecting the signal from the AWG. Generally, a low-pass filter (DC - 200 MHz) is also attached to an AWG output channel, but we often remove it to achieve faster voltage pulses.

The fridge contains sixteen HF lines, equally divided between the two devices. To reduce the thermal noise reaching the sample through these lines, one HF line is made of six coax pieces. Each of these coax pieces connects two consecutive plates of the fridge and one cryo-attenuator is used per plate to improve thermal anchoring of an HF line to each plate. Two different sets of lines with slightly different total attenuation are used for the 2x2 and the eight-dot devices. Fig. 3.7 shows an overview of the attenuator distribution of the two sets of lines. In addition, we use graphite coated CuNi coax cables to reduce vibration-induced electrical noise.

4. RF READOUT

The sensing dots in a device are used to detect movement of charge close to it. By carefully creating sensing dots in the vicinity of the main dot array, we can detect electrons moving between two dots or between a dot and a reservoir. We perform RF-readout by combining each sensing dot to an LCR circuit to increase the measurement bandwidth

⁵For details, see: <http://qwork.tudelft.nl/~schouten/sampwfilters/index-sampwfilters.htm>

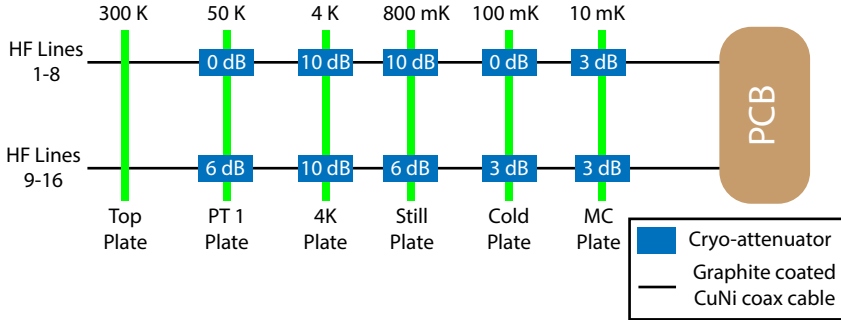


Figure 3.7: Schematic diagram of the high frequency control lines

compared to DC charge-sensing. In this circuit, the R is given by the resistance of the sensing dot used. An external inductor is attached to the PCB to provide the L. Finally, the C is the total parasitic capacitance coming from the inductor, the sample, and the PCB line. Using this RF-readout technique, we could achieve ~ 1 MHz measurement bandwidth. Moreover, an RF-frequency of the order of 100 MHz is typically used as carrier frequency, which is later demodulated to measurement bandwidth around the carrier frequency. This helps us to dramatically reduce the contribution of $1/f$ noise. The details of the RF-readout circuit is described below.

Let Z be the impedance of the sensing dot. The sensing dot has maximum charge sensitivity $\left(\frac{dZ}{dq}\right)$ at the slope of a Coulomb peak, where the resistance (R) is 100 - 200 k Ω . But for a normal RF-circuit, the signal is carried by a coax line with 50 Ω impedance (Z_0). Now the complex voltage reflection coefficient (Γ) for such circuit is given by:

$$\Gamma = \frac{Z_L - Z_0}{Z_L + Z_0} \quad (3.1)$$

For optimal $\frac{dZ}{dq}$, high load resistance ($Z_L = R \sim 100$ k Ω) leads to almost all the signal being reflected ($\Gamma \approx 1$), resulting in a poor signal-to-noise (SNR) ratio. This SNR can be improved by bringing Z_L close to Z_0 ($= 50$ Ω) and thus reducing Γ . One can use the idea of a matching circuit to modify the effective value of Z_L . In a matching LCR circuit, the equivalent impedance at resonance frequency ($f \approx \frac{1}{2\pi\sqrt{LC}}$) is given by:

$$Z_{eq} = \frac{L}{RC} \quad (3.2)$$

Here the only controllable parameter is L, as the values of R and C are set by other experimental considerations. As discussed earlier, R is about 100 k Ω for the most sensitive sensor. The parasitic capacitance, C, has a typical value of 0.7 pF, for the samples measured. Using $L \approx 3$ μ H, the Z_{eq} can be brought close to 50 Ω at the resonance frequency, $f \sim 100$ MHz. To avoid high resistance from the inductors, we use home-made NbTiN spiral inductor on a quartz substrate. As NbTiN is a superconductor at the base temperature of the fridge, the resistance of the inductor goes to zero. Using frequency

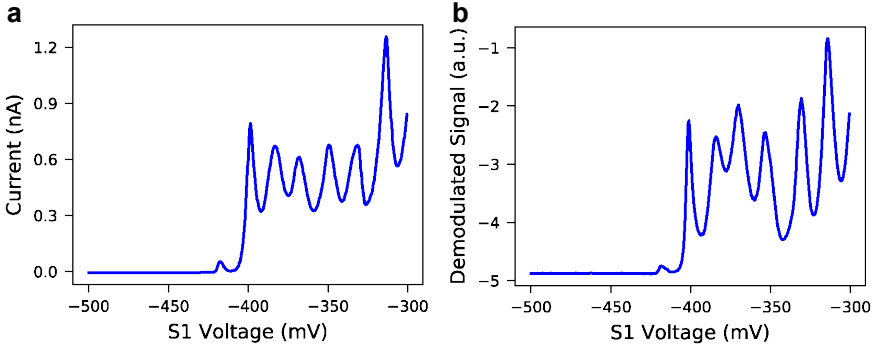


Figure 3.8: (a) Sensing dot signal in transport measurement. (b) Sensing dot signal in RF-reflectometry measurement

multiplexing, a single coax line can be used to perform RF-sensing with multiple sensing channels simultaneously. Appropriate inductors are chosen to bring the Z_{eq} sufficiently close to 50Ω to reduce Γ as much as possible while keeping the corresponding resonance frequencies sufficiently separated compared to the measurement bandwidth of ~ 1 MHz. For the 2×2 device, RF-sensing is performed using two sensing dots with inductors of 4.6 and $2.0 \mu\text{H}$. The resonance frequencies turn out to be 84.6 and 131.5 MHz respectively. Fig. 3.8 (a-b) show a comparison of the DC and the demodulated RF signal through the same sensing dot.

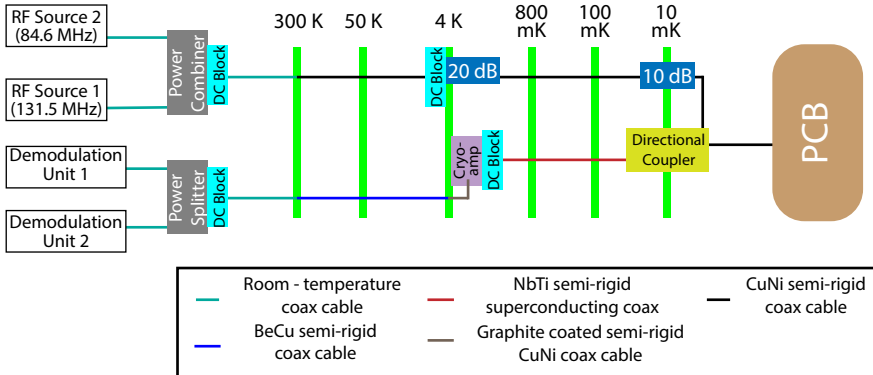


Figure 3.9: Schematic of RF-sensing circuit used for measurement

The details of the RF-reflectometry setup are described below (Fig. 3.9). We use home-made modules⁶ for both RF signal generation and demodulation of the output signal. First, the RF signals of two separate frequencies are coupled using a power split-

⁶For details of these modules, see: <http://qtworck.tudelft.nl/~mtiggelman/modules.html>

ter (combiner)⁷ and transmitted forward through a DC-block⁸. Inside the fridge, the input signal is carried by CuNi semi-rigid coax cable, where the signal goes through a DC-block at the 4K plate and gets attenuated at the 4K and the MC plates by 20 dB and 10 dB respectively. After the mixing chamber attenuator, this signal is carried to the input port of a directional coupler⁹, attached to the MC plate. The coupled port of the directional coupler is connected to the PCB to carry both the input and the reflected output signals. Next, the output signal from the coupler is carried using a NbTi superconducting coax through another DC-block to a low-noise cryogenic amplifier¹⁰, attached to the 4K plate. The output signal from this amplifier is then carried out of the fridge, where the signal is split into two equal parts with a power splitter. Finally, each part of this signal is demodulated with the carrier frequency using a home-made demodulation unit.

BIBLIOGRAPHY

- [1] T. Baart, *CCD operation and long-range coupling of spins in quantum dot arrays*, Ph.D. thesis, Delft University of Technology (2016).
- [2] R. Thalineau, S. Hermelin, A. D. Wieck, C. Bäuerle, L. Saminadayar, and T. Meunier, *Applied Physics Letters* **101**, 103102 (2012).
- [3] T. Baart, P. Eendebak, C. Reichl, W. Wegscheider, and L. Vandersypen, *Applied Physics Letters* **108**, 213104 (2016).
- [4] T. Fujita, T. A. Baart, C. Reichl, W. Wegscheider, and L. M. K. Vandersypen, *npj Quantum Information* **3**, 22 (2017).
- [5] C. Volk, A. M. J. Zwerver, U. Mukhopadhyay, P. T. Eendebak, C. J. van Diepen, J. P. Dehollain, T. Hensgens, T. Fujita, C. Reichl, W. Wegscheider, and L. M. K. Vandersypen, *npj Quantum Information* **5**, 29 (2019).

⁷Mini-Circuits ZFSC-2-5-S+

⁸Pasternack PE8212

⁹Mini-Circuits ZEDC-15-2B

¹⁰Cosmic Microwave Technology CITLF3

4

A 2×2 QUANTUM DOT ARRAY WITH CONTROLLABLE INTER-DOT TUNNEL COUPLINGS

The interaction between electrons in arrays of electrostatically defined quantum dots is naturally described by a Fermi-Hubbard Hamiltonian. Moreover, the high degree of tunability of these systems makes them a powerful platform to simulate different regimes of the Hubbard model. However, most quantum dot array implementations have been limited to one-dimensional linear arrays. In this letter, we present a square lattice unit cell of 2×2 quantum dots defined electrostatically in an AlGaAs/GaAs heterostructure using a double-layer gate technique. We probe the properties of the array using nearby quantum dots operated as charge sensors. We show that we can deterministically and dynamically control the charge occupation in each quantum dot in the single- to few-electron regime. Additionally, we achieve simultaneous individual control of the nearest-neighbor tunnel couplings over a range 0-40 μeV . Finally, we demonstrate fast ($\sim 1 \mu\text{s}$) single-shot readout of the spin state of electrons in the dots, through spin-to-charge conversion via Pauli spin blockade. These advances pave the way for analog quantum simulations in two dimensions, not previously accessible in quantum dot systems.

4.1. INTRODUCTION

Electrostatically defined quantum dots in semiconductors have been proposed as the basic underlying hardware in quantum computation [2], as well as digital and analog quantum simulations [3–6]. This is due to their ease of tunability, control of the relevant parameters, fast measurement of the spin and charge states, and their potential for scalability. In particular, quantum dot arrays are natural candidates for simulating the Fermi-Hubbard model, as they adhere to the same Hamiltonian:

$$\begin{aligned}
 H = & \sum_i U_i n_{i\uparrow} n_{i\downarrow} - \sum_{i,j,\sigma} t_{i,j} \left(c_{i\sigma}^\dagger c_{j\sigma} + h.c. \right) - \sum_i \mu_i n_i \\
 & + \sum_{i,j} V_{i,j} n_i n_j
 \end{aligned} \tag{4.1}$$

The on-site interaction energy U_i corresponds to the quantum dot charging energy on site i and the hopping energy $t_{i,j}$ corresponds to the tunnel coupling between dots i and j . The chemical potential term μ_i controls the electron number in each dot, as well as the relative energy detuning between dots. For quantum dot arrays, there is an additional term $V_{i,j}$ that describes the inter-site Coulomb interaction energy. The operators c_i, c_i^\dagger, n_i in Eqs. 4.1 represent the second quantization annihilation, creation, and number operators, respectively, with the individual spins of the electrons being denoted by the subscript $\sigma = \{\uparrow, \downarrow\}$. For simplicity, we have assumed that no external magnetic field is present in the system.

For the study of Fermi-Hubbard physics, control of the ratio U/t is essential [7–9]. The hopping term can be tuned electrostatically, covering a range $t \approx 0 - 100 \mu\text{eV}$ between nearest neighbors in a linear array [10]. The on-site interaction energy U is set by the shape of the confinement potential and is not freely tunable, but it can be accurately measured with typical values of 1 - 10 meV [11]. Similarly, V is not tunable independently but can be measured precisely.

Quantum simulations of the Fermi-Hubbard model have previously been explored experimentally in cold atom systems [12–16], manipulating arrays of the order of 100 atoms. However, these experiments are often limited by the initial entropy of the system [13–15]. Quantum dot arrays can overcome this problem by operating in dilution refrigerators, where electron temperatures can reach $kT_e \sim 1 \mu\text{eV}$. On the other hand, experiments with quantum dots are still mainly being performed with linear arrays with no more than a few sites [10, 17, 18]. Efforts to go beyond 1D with quantum dot arrays have so far stopped short of achieving well-characterized tunnel couplings in the few-electron regime [19–21].

In this letter, we report on the design, fabrication, and measurement of a quantum-dot plaquette in a 2×2 geometry. We describe a fabrication technique used to implement a two-layer gate structure needed for this device. We then present measurements that demonstrate deterministic filling of electrons in all dots and controllable tunnel coupling over a large range (0 - 40 μeV) between all nearest-neighbor pairs. As the final ingredient for this quantum simulator, we perform single-shot measurements of the two-electron singlet/triplet states ($|S\rangle/|T\rangle$) using two dots in the array.

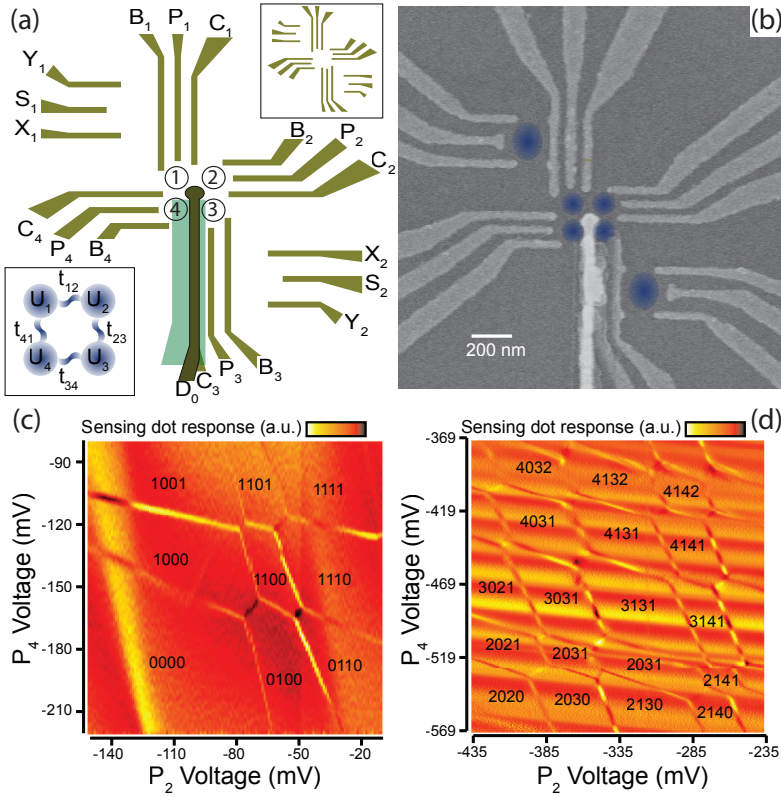


Figure 4.1: (a) Schematic of the gate design, with the dot locations labeled in the center. (The first layer in the top inset and the bottom inset shows a schematic of the dot plaquette, with relevant Hubbard model terms.) (b) SEM image of a device from the same batch as the one used for measurements. The overlaid blue circles are impressions of the dot wave-functions. (c)-(d) Charge stability diagrams showing controlled filling of all four quantum dots in the single- (c) and few- (d) electron regime. The data in (c) and Fig. 4.3 was taken in one device cooldown and the data in panel (d), Table 4.1 and Fig. 4.2 in another cooldown.

4.2. DEVICE DETAILS

The device contains electrostatically defined quantum dots formed by selectively depleting electrons using nano-fabricated gate electrodes on the surface of a GaAs/AlGaAs heterostructure. The gate pattern is designed to form four quantum dots in a 2×2 geometry, where the nearest neighbors are cyclic, i.e. $i + 4 = i$ (Fig. 4.1(a)). The coupling of each of the dots to its own electron reservoir is controlled through the constriction created between the B_{i+1} and the C_i gates. This is designed to allow for operation of the quantum dots in the isolated regime [17, 22]; however, we do not explore this configuration here. Deterministic electron filling of the quantum dots is achieved by adjusting μ_i relative to the Fermi energy of the reservoirs, through the use of the gates P_i . A center gate (D_0) reaches the substrate at the center of the plaquette. Biasing this gate negatively effectively separates the dots from each other. It thereby suppresses tunnel couplings along

Table 4.1: Relevant gate voltages and lever arms

	B1	B2	B3	B4	P1	P2	P3	P4	C1	C2	C3	C4	D0	X1	X2	Y1	Y2	S1	S2
Voltages at 1111 (mV)	-150	-230	-130	-100	-263	-60	-9	-221	-120	-180	-180	-220	-180	-360	-120	-280	-270	-110	-390
Voltages at 3131 (mV)	-100	-20	-90	-194	-169	-335	-30	-469	-188	-141	-37	-57	-135	-343	-95	-310	-274	-429	-504
Bias cooling voltage (mV)	300	250	300	250	150	150	150	150	250	250	250	250	200	350	350	300	300	200	200
Lever Arms ($\mu\text{eV}/\text{mV}$)					39	41	54	31											
(Plungers to dots)					(D1)	(D2)	(D3)	(D4)											

the two diagonals of the array and also influences the nearest-neighbor tunnel couplings (along the perimeter of the array), since the combination of D_0 with a C_i gate controls $t_{i,i+1}$. The device design also includes an extra set of gates (X_i , Y_i , S_i) used to define two larger dots to be operated as charge sensors. The GaAs/ $\text{Al}_x\text{Ga}_{1-x}\text{As}$ heterostructure is Si-doped, with a two-dimensional electron gas at the 90 nm deep interface ($x = 0.314$, mobility = $1.6 \times 10^6 \text{ cm}^2/\text{Vs}$ and electron density = $1.9 \times 10^{11} \text{ cm}^{-2}$). All gates except D_0 are fabricated in the first layer with Ti/Au of thickness 5/20 nm, evaporated on the bare substrate and patterned following standard procedures[23] (the top inset in Fig. 4.1(a) shows the schematic of this layer). The D_0 gate runs above gate C_3 and contacts the substrate at the center of the array with a foot of ~ 50 nm radius. It is fabricated using 10/100 nm evaporated Ti/Au and isolated from the bottom layer gates using a 50 nm thick, 200 nm wide, and $1.5 \mu\text{m}$ long dielectric slab of SiN_x , fabricated using sputtering and lift-off. For this step, an 80 nm thick layer of AR-P 6200[24] is used as the e-beam resist and lift-off is performed in hot (80°C) N-Methyl-2-Pyrrolidone. A scanning electron microscope (SEM) image of a completed device is shown in Fig. 4.1(b).

4.3. CONTROLLABLE CHARGE OCCUPATION

The device was cooled down with positive bias voltages (see values in Table 4.1) on all gates in order to decrease charge noise [25]. All the P_i and C_i gates are connected to high-frequency (~ 1 GHz) lines for pulsing and fast sweeping. One reservoir for each sensing dot is connected to a resonant RF circuit for high-bandwidth (up to 3 MHz) charge sensing. The two readout circuits have resonance frequencies of 84.5 and 130.6 MHz, are connected to a single amplifier chain and are read out simultaneously using frequency multiplexing [26]. By measuring charge stability diagrams using different combinations of gates, we can identify and tune the four dots to the few-electron regime. In Fig. 4.1(c-d), we show examples of two charge stability diagrams, where we have identified the charge states of the four dots, ranging from (0000) to (4142), where ($klmn$) indicate the charge occupation of dots 1 through 4. The different cross-capacitances between the dots and the gates lead to charge transition lines with four different slopes in the charge stability diagrams, corresponding to the filling of the four dots.

Using these diagrams, appropriate voltages can be applied to the gates to achieve deterministic filling of the dots. Although we can reach the regime with one electron in each dot, it was difficult to tunnel couple all neighboring dots. We attribute this to the center gate being slightly too large. To bypass this problem, we keep the first orbital shells of dots 1 and 3 filled with two electrons each. In this configuration, the electron

wavefunction is larger, which facilitates tunnel coupling neighboring dots. However, it is important to note that in this configuration, the unpaired electron occupies an anti-symmetric (2p) orbital [27], which can result in effects such as a sign inversion in the tunnel coupling. The gate voltages needed to achieve (1111) and (3131) charge states are specified in Table 4.1. We perform finite voltage-bias measurements [28, 29] to extract the lever arm (see Table 4.1) between gate voltage and dot chemical potential energy. Using these, the charging energies for the four dots are then estimated from the distance between charge transition lines in the charge stability diagrams [$U_1 = 2.1$ meV, $U_3 = 2.3$ meV (3 electron dots) and $U_2 = 3.4$ meV, $U_4 = 3.3$ meV (1 electron dots)]. From the same diagrams, we also extract the inter-site Coulomb interaction energies $V_{1,2} = 0.67$ meV, $V_{2,3} = 0.55$ meV, $V_{3,4} = 0.47$ meV, $V_{4,1} = 0.39$ meV.

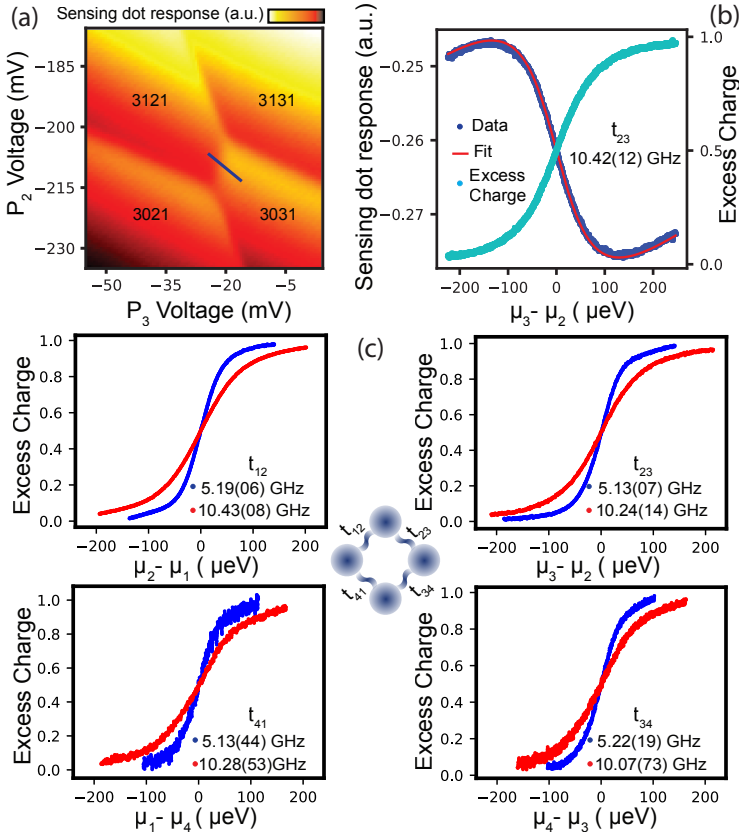


Figure 4.2: (a) Charge stability diagram zoomed in on an inter-dot transition. (b) A line cut of panel (a) along the detuning axis (blue line in (a)) and fitting of the line to get tunnel coupling and excess charge distribution. (c) Excess charge extracted from the sensing dot signal when changing gate voltages along the detuning axis for the four different double dots in the plaquette. The data show controllable tunnel couplings between all nearest-neighbor double-dot pairs. All the curves of the same color were taken using the same global gate configuration.

4.4. CONTROLLABLE NEAREST-NEIGHBOUR TUNNEL COUPLING

We next characterize and control the four inter-dot tunnel couplings. Starting with the array in the (3131) charge state, we measure $t_{i,j}$ by moving to a gate voltage configuration that removes one electron from the system and is centered at $\mu_i = \mu_j$ while keeping the other two dots (slightly) detuned. Around this point, the charge stability diagram shows an inter-dot transition line (Fig. 4.2(a)). As we sweep the voltage along the detuning axis (perpendicular to the inter-dot transition), the charge sensor signal displays a step as the extra electron moves over from one dot to the other. The width of this step is dependent on the tunnel coupling $t_{i,j}$ and the electron temperature T_e [10, 30]. Fig. 4.2(b) shows a sample measurement where the sensor signal is plotted as we sweep the gate voltages across the inter-dot transition. This signal is then fitted to extract $t_{i,j}$ given $T_e \sim 70$ mK ($\sim 6 \mu\text{eV}$). T_e was measured by fitting a similar trace for the case $t \ll T_e$. Note that this measurement of T_e provides an upper bound for the charge noise. From the fits to the current traces, we derive the excess charge as a function of detuning between the two dots (Fig. 4.2(b)).

Nearest-neighbor tunnel couplings can be controlled electrostatically by opening/closing the constrictions created between D_0 and the C_i gates. However, if we vary these gates only, the cross-capacitance between these gates and the dots results in unwanted changes in the chemical potential of the dots. To remedy this, we map out a cross-capacitance matrix that expresses the capacitive coupling between all gates and every dot. For small changes in gate voltage ($< \sim 100$ mV), we can assume these cross-capacitances to remain constant and the changes in the individual dot energies can be expressed as linear combinations of gate voltages:

$$\begin{bmatrix} \delta\mu_1 \\ \delta\mu_2 \\ \delta\mu_3 \\ \delta\mu_4 \end{bmatrix} = \zeta \delta\mathbf{G}, \quad \mathbf{G} = \begin{bmatrix} P_1 \\ P_2 \\ P_3 \\ P_4 \\ C_1 \\ C_2 \\ C_3 \\ C_4 \\ D_0 \end{bmatrix}$$

where ζ is a 4×9 matrix of cross-capacitances: $\zeta_{i,i}$ corresponds to the lever-arm of gate P_i to dot i , and $\zeta_{i,j} = \zeta_{i,i}\eta_{i,j}$, where $\eta_{i,j} = \delta P_i / \delta G_j$ is the slope of the charge transition of dot i , which can be extracted from a charge stability diagram. Once extracted, ζ can then be used to define virtual gates [10] (C'_i or D'_0) that allow us to vary one of the C_i or D_0 gates, while simultaneously adjusting all the P_i gates to keep $\delta\mu_i = 0$. For example, for C'_i the adjustment of P_i can be calculated from:

$$\begin{bmatrix} \delta P_1 \\ \delta P_2 \\ \delta P_3 \\ \delta P_4 \end{bmatrix} = -\delta C_1 \begin{bmatrix} \zeta_{1,1} & \zeta_{1,2} & \zeta_{1,3} & \zeta_{1,4} \\ \zeta_{2,1} & \zeta_{2,2} & \zeta_{2,3} & \zeta_{2,4} \\ \zeta_{3,1} & \zeta_{3,2} & \zeta_{3,3} & \zeta_{3,4} \\ \zeta_{4,1} & \zeta_{4,2} & \zeta_{4,3} & \zeta_{4,4} \end{bmatrix}^{-1} \begin{bmatrix} \zeta_{1,5} \\ \zeta_{2,5} \\ \zeta_{3,5} \\ \zeta_{4,5} \end{bmatrix} \quad (4.2)$$

This technique significantly simplified the process of adjusting the tunnel barriers and was a key element in achieving effective tunnel coupling control. In Fig. 4.2(c) this control is demonstrated by uniformly setting all four tunnel couplings to 5 GHz ($\sim 20 \mu\text{eV}$, blue traces) and 10 GHz ($\sim 40 \mu\text{eV}$, red traces).

The same device can be tuned to different regimes by changing bias-cooling and gate voltages. In subsection 4.7.1, we discuss tuning to achieve controllable tunnel coupling with one electron per dot. The experiment in chapter 5 is performed using this device configuration.

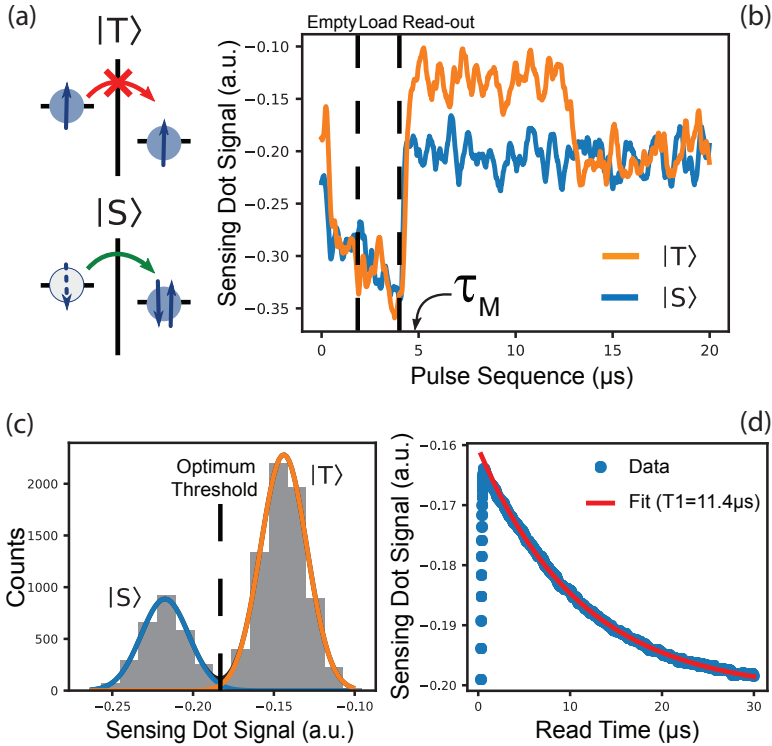


Figure 4.3: (a) Schematic of the spin to charge conversion process used to read out the spin states via Pauli spin blockade. (b) Example single-shot read-out traces for singlet (blue) and triplet (orange) states. (c) A histogram of the current signal at time τ_M constructed from 10000 single-shot measurements. Solid lines are Gaussian fits to the two peaks in the histogram corresponding to singlet (blue) and triplet (orange) states. (d) Average signal obtained from 10000 read-out traces. The solid line is an exponential fit, from which we extract the relaxation time T_1 .

4.5. SINGLE SHOT SPIN READOUT

Finally, we demonstrate single-shot read-out of two-spin states using a three-stage pulse [31]. The Pauli exclusion principle [32] is used to convert a charge measurement into a mea-

surement that distinguishes between singlet and triplet states of two spins occupying neighboring quantum dots. We follow a protocol used previously to read out spins in a double dot [33] where a random two-spin state is loaded in the (1,1) charge configuration. The detuning between the dots is then pulsed to favor tunneling towards the (2,0) charge state. We call this detuning configuration the read-out point. For a singlet ($|S\rangle$), tunneling to (2,0) is allowed. For a triplet ($|T\rangle$) however, the Pauli exclusion principle requires the (2,0) state to occupy the first excited state orbital of the dot, which is energetically inaccessible (~ 0.4 meV away). Therefore, spins in $|T\rangle$ remain in the (1,1) state (Fig. 4.3(a)) until they relax to $|S\rangle$, with rate $1/T_1$. To identify the spin states, we monitor the charge sensor signal at a specific time τ_M after the start of the read-out pulse. We integrate the signal for $0.1 \mu\text{s}$ around τ_M . If the integrated signal exceeds (does not exceed) a fixed threshold, we conclude that the charge state was (1,1) [(2,0)] indicating a $|T\rangle$ ($|S\rangle$) spin state (Fig. 4.3(b)).

4

The read-out fidelity is limited by several factors. A histogram of the integrated sensing dot signal at time τ_M constructed from 10000 single-shot measurements with a random initial spin state shows two peaks, corresponding to the signal measured for each of the spin states (Fig. 4.3(d)). Due to noise in the current traces, there is a small overlap between the two peaks that will lead to spin read-out errors. From a double Gaussian fit to the histograms, we extract an error contribution $e_N = 0.006$. When averaging 10000 complete read-out traces, the sensor signal shows an exponential decay, with a time constant T_1 (Fig. 4.3(c)). The T_1 value varies with inter-dot detuning [33], reaching up to $T_1 = 11.4 \mu\text{s}$. A relaxation event before τ_M leads to a measurement error, and so, it is important to keep τ_M short. In order to achieve a sufficient signal-to-noise ratio, we low-pass filtered the signal with a 1 MHz cut-off, which in turn leads us to choose $\tau_M = 0.8 \mu\text{s}$. The $|T\rangle$ measurement error due to relaxation is then $e_{T1} = 1 - \exp(-\tau_M/T_1) = 0.07$. This is the dominant source of error in this system, with smaller error contributions from thermal excitation, limiting the average measurement fidelity to $F_M \approx 0.96$. Details of this thermal excitation are discussed in subsection 4.7.2.

4.6. DISCUSSION

In summary, we have implemented and operated a quantum dot plaquette with reliable control of electron filling and tunnel coupling, for which we demonstrated single-shot spin measurements. This makes this system a promising analog quantum simulator of Fermi-Hubbard physics. The two-dimensional lattice configuration presents symmetries not accessible in the more common linear arrays, enabling the emulation of phenomena such as Nagaoka ferromagnetism [34] and resonating valence bond states [35], which have been predicted for high-temperature superconductors. Moreover, using the two-layer fabrication technique shown here, the 2×2 geometry can be extended directly to a ladder of quantum dots (size $2 \times N$), which is the smallest system capable of showing pairing in under- or over-doped lattices [36] and other interesting quantum phases [37]. Moreover, leveraging the fabrication experience of the semiconductor industry, quantum dot arrays might be scaled up to $N \times N$ arrays, opening up a host of possibilities.

4.7. ADDITIONAL MATERIAL

4.7.1. CONTROLLABLE NEAREST-NEIGHBOUR TUNNEL-COUPLING WITH ONE ELECTRON PER DOT

The tuning of nearest-neighbour tunnel coupling is an essential step towards successfully simulating the Fermi-Hubbard model in the 2x2 device. We have demonstrated controllable tunnel coupling over a range of 0 to 40 μeV in the (3131) charge state. Although this range itself meets the immediate requirement, having three electrons in a dot could introduce additional challenges for the Hubbard model simulations. The third electron occupies one of the two antisymmetric 2p orbitals of a dot. The energy separation between these 2p orbitals is caused by the asymmetry in the dot shape that is typical of realistic devices. The next electron added to the dot occupies one of these two orbitals depending on this energy separation. To use a three-electron dot to simulate the Hubbard model, the third and the fourth electrons must have opposite spins. This is enforced by Pauli's exclusion principle only if the electrons occupy the same orbital. However, these spins lack any correlation if the third and the fourth electrons occupy different 2p orbitals, which prevents the dot from being used in the Hubbard model simulation. The sign inversion of tunnel coupling, introduced in section 4.3, can further complicate these simulations. This sign inversion is also difficult to measure experimentally.

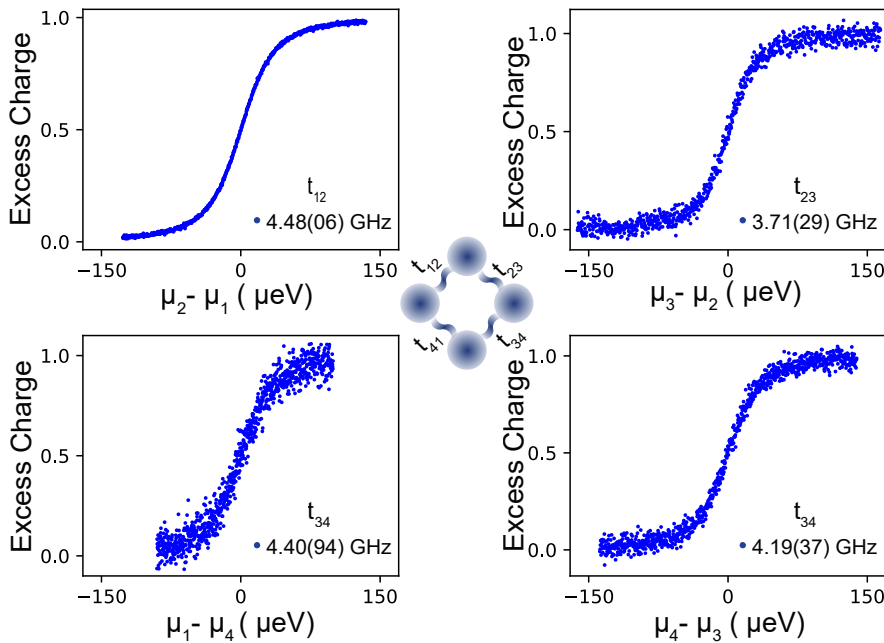


Figure 4.4: Excess charge extracted from the sensing dot signal when changing gate voltages along the detuning axis for the four different double dots in the plaquette. The data is taken in (1111) charge configuration. The different signal-to-noise ratio in these traces arises from the difference in sensitivity of the charge sensors to each inter-dot transition.

Table 4.2: Relevant gate voltages and lever arms for the retuned dot-system

	B1	B2	B3	B4	P1	P2	P3	P4	C1	C2	C3	C4	D0	X1	X2	Y1	Y2	S1	S2
Voltages at 1111 (mV)	-90	-53	-75	-45	-237	-188	-136	-442	-185	-280	-115	-317	-87	-191	-217	-351	-253	-186	-178
Bias cooling voltage (mV)	300	250	300	250	150	150	150	200	250	250	250	250	200	350	350	300	300	200	200
Lever Arms ($\mu\text{eV}/\text{mV}$)					29.5	45	55.4	38											
(Plungers to dots)					(D1)	(D2)	(D3)	(D4)											

We changed the system configuration to obtain tunable tunnel coupling with one electron per dot and avoid the potential problems. This was accomplished using the same device in a different cool-down with slightly modified bias voltages (see Table 4.2). The gate voltages needed to achieve (1111) charge state and the lever arm between gate voltages and dot chemical potential energies for this system are mentioned in Table 4.2. We use charge stability diagrams to estimate the on-site ($[U_1, U_2, U_3, U_4] \approx [2.9, 2.6, 2.9, 3.0]$ meV) and inter-site ($[V_{12}, V_{23}, V_{34}, V_{41}, V_{13}, V_{24}] \approx [0.47, 0.35, 0.43, 0.30, 0.28, 0.18]$ meV) Coulomb interaction energies. The method mentioned in subsection 4.4 is used to estimate the tunnel couplings between nearest-neighbour double dot pairs. These tunnel couplings are found to be controllable, although the range is smaller than what has been achieved in the (3131) charge configuration (see subsection 4.4). We demonstrate this control in Fig. 4.4 by simultaneously setting all four nearest-neighbour tunnel couplings to 4GHz ($\sim 16 \mu\text{eV}$).



Figure 4.5: Example single shot traces showing thermal excitation for both singlet (blue) and triplet (orange) initial spin states.

4.7.2. THERMAL EXCITATION DURING SPIN READOUT

The (2,0) charge state is energetically favored at the read-out point (see section 4.5). So at steady-state (time ($\tau \gg T_1$)), one would expect the two electrons to attain this charge

configuration and remain there until the detuning between the dots is changed. Unfortunately, this is not true in our system. We observe spontaneous excitation from (2,0) to (1,1) charge configuration while waiting at the read-out point. We attribute this phenomenon to thermal excitation, as it appeared only when we removed the mixing chamber radiation shield of the fridge (see subsection 3.2.1 for details).

We note that the thermal excitation does not depend on the initial spin state of the electrons. Fig 4.5 shows this spontaneous excitation in single-shot read-out traces for both singlet (blue) and triplet (orange) initial spin-states. The rate of this excitation is given by $1/T_{th}$. We measure 60000 traces of sensor signal at the read-out point for 960 μs each to determine this T_{th} . Fig. 4.6(a) shows a histogram of time spent by the system in the (2,0) state, before a transition to (1,1) charge state. The value of T_{th} is extracted to be 67.9 μs from a fitted exponential decay to this histogram. Similarly, we estimate $T_1 = 13.1 \mu\text{s}$ from the fit to the histogram of time spent by the system in the (1,1) state (Fig. 4.6(b)). The thermal excitation introduces an error in the spin read-out, but only for singlet state ($|S\rangle$). The $|S\rangle$ measurement error due to this excitation is given by $e_{TH} = 1 - \exp(-\tau_M/T_{th}) \approx 0.01$, which affects the read-out fidelity by less than 1%.

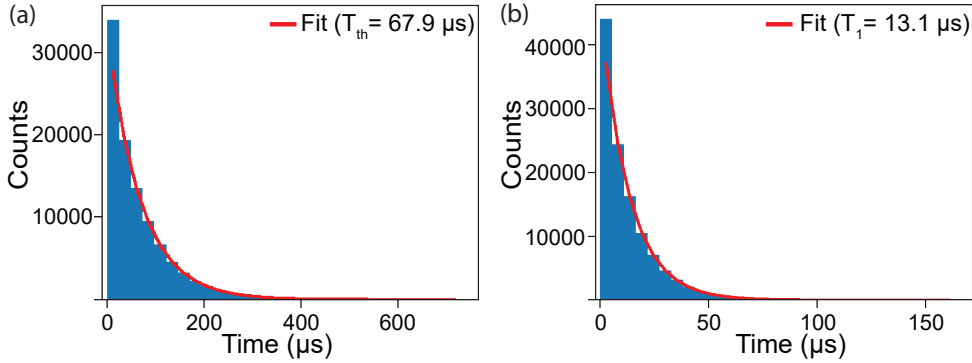


Figure 4.6: (a) A histogram of time spent by the system at (2,0) charge state, before a transition to (1,1) charge state, constructed from 60000 single traces of 960 μs each. The red line is an exponential decay fit to estimate T_{th} . (b) A histogram of time spent by the system at (1,1) charge state, before a transition to (2,0) charge state, constructed from the same dataset, with exponential fit to estimate T_1 (red line).

Finally, we discuss the effect of this thermal excitation on the steady-state ($\tau \gg T_1, T_{th}$) probability of measuring triplet (P_T) ((2,0) charge state) at the read-out point. The steady-state value of P_T (P_T^{SS}) is expected to be 0 without the thermal excitation. The rate equation for the transition to (2,0) charge state in our system is given by

$$\frac{dP_T}{d\tau} = -\Gamma_1 P_T + \Gamma_2 (1 - P_T) \quad (4.3)$$

Where Γ_1 and Γ_2 are given by $1/T_1$ and $1/T_{th}$ respectively. Solving Eqn. 4.3, we get

$$P_T(\tau) = \frac{\Gamma_2}{\Gamma_1 + \Gamma_2} - \left(\frac{\Gamma_2}{\Gamma_1 + \Gamma_2} - P_T^0 \right) e^{-(\Gamma_1 + \Gamma_2)\tau} \quad (4.4)$$

P_T^0 is the initial probability of measuring triplet. The steady-state condition ($\tau \gg T_1, T_{th}$) can be applied on Eqn. 4.4 to estimate

$$P_T^{ss} = \frac{\Gamma_2}{\Gamma_1 + \Gamma_2} = \frac{T_1}{T_1 + T_{th}}$$

Both T_1 and T_{th} depend on the detuning between the dots, and they can be used to estimate the value of P_T^{ss} . Meanwhile, P_T^{ss} can also be measured experimentally, which matches the estimated value very well. For the data shown in Fig. 4.6, $P_T^{ss} = 0.16$.

BIBLIOGRAPHY

- [1] U. Mukhopadhyay, J. P. Dehollain, C. Reichl, W. Wegscheider, and L. M. K. Vandersypen, *Applied Physics Letters* **112**, 183505 (2018) .
- [2] D. Loss and D. P. DiVincenzo, *Phys. Rev. A* **57**, 120 (1998).
- [3] T. Byrnes, N. Y. Kim, K. Kusudo, and Y. Yamamoto, *Phys. Rev. B* **78**, 075320 (2008).
- [4] S. Yang, X. Wang, and S. Das Sarma, *Phys. Rev. B* **83**, 161301 (2011).
- [5] C. A. Stafford and S. Das Sarma, *Phys. Rev. Lett.* **72**, 3590 (1994).
- [6] P. Barthelemy and L. M. K. Vandersypen, *Ann. Phys. (Berl.)* **525**, 808 (2013).
- [7] M. Imada, A. Fujimori, and Y. Tokura, *Rev. Mod. Phys.* **70**, 1039 (1998).
- [8] P. A. Lee, N. Nagaosa, and X.-G. Wen, *Rev. Mod. Phys.* **78**, 17 (2006).
- [9] L. Balents, *Nature* **464**, 199 (2010).
- [10] T. Hensgens, T. Fujita, L. Janssen, X. Li, C. J. Van Diepen, C. Reichl, W. Wegscheider, S. Das Sarma, and L. M. K. Vandersypen, *Nature* **548**, 70 (2017).
- [11] L. P. Kouwenhoven, C. M. Marcus, P. L. McEuen, S. Tarucha, R. M. Westervelt, and N. S. Wingreen, "Electron transport in quantum dots," in *Mesoscopic Electron Transport*, edited by L. L. Sohn, L. P. Kouwenhoven, and G. Schön (Springer Netherlands, Dordrecht, 1997) pp. 105–214.
- [12] R. Jördens, N. Strohmaier, K. Günter, H. Moritz, and T. Esslinger, *Nature* **455**, 204 (2008).
- [13] M. F. Parsons, A. Mazurenko, C. S. Chiu, G. Ji, D. Greif, and M. Greiner, *Science* **353**, 1253 (2016).
- [14] M. Boll, T. A. Hilker, G. Salomon, A. Omran, J. Nespolo, L. Pollet, I. Bloch, and C. Gross, *Science* **353**, 1257 (2016).
- [15] L. W. Cheuk, M. A. Nichols, K. R. Lawrence, M. Okan, H. Zhang, E. Khatami, N. Trivedi, T. Paiva, M. Rigol, and M. W. Zwierlein, *Science* **353**, 1260 (2016).

- [16] A. Mazurenko, C. S. Chiu, G. Ji, M. F. Parsons, M. Kanász-Nagy, R. Schmidt, F. Grusdt, E. Demler, D. Greif, and M. Greiner, *Nature* **545**, 462 (2017).
- [17] H. Flentje, B. Bertrand, P.-A. Mortemousque, V. Thiney, A. Ludwig, A. D. Wieck, C. Bäuerle, and T. Meunier, *Appl. Phys. Lett.* **110**, 233101 (2017).
- [18] F. K. Malinowski, F. Martins, T. B. Smith, S. D. Bartlett, A. C. Doherty, P. D. Nissen, S. Fallahi, G. C. Gardner, M. J. Manfra, C. M. Marcus, and F. Kuemmeth, *Phys. Rev. X* **8**, 011045 (2018).
- [19] M. Seo, H. K. Choi, S.-Y. Lee, N. Kim, Y. Chung, H.-S. Sim, V. Umansky, and D. Mahalu, *Phys. Rev. Lett.* **110**, 046803 (2013).
- [20] R. Thalineau, S. Hermelin, A. D. Wieck, C. Bäuerle, L. Saminadayar, and T. Meunier, *Appl. Phys. Lett.* **101**, 103102 (2012).
- [21] A. Noiri, K. Kawasaki, T. Otsuka, T. Nakajima, J. Yoneda, S. Amaha, M. R. Delbecq, K. Takeda, G. Allison, A. Ludwig, A. D. Wieck, and S. Tarucha, *Semicond. Sci. Technol.* **32**, 084004 (2017).
- [22] B. Bertrand, H. Flentje, S. Takada, M. Yamamoto, S. Tarucha, A. Ludwig, A. D. Wieck, C. Bäuerle, and T. Meunier, *Phys. Rev. Lett.* **115**, 096801 (2015).
- [23] T. Baart, *CCD operation and long-range coupling of spins in quantum dot arrays*, Ph.D. thesis, Delft University of Technology (2016).
- [24] “Csar 62 (**AR – P 6200**),” <http://www.allresist.com/csar-62-ar-p-6200/>.
- [25] M. Pioro-Ladrière, J. H. Davies, A. R. Long, A. S. Sachrajda, L. Gaudreau, P. Zawadzki, J. Lapointe, J. Gupta, Z. Wasilewski, and S. Studenikin, *Phys. Rev. B* **72**, 115331 (2005).
- [26] E. A. Laird, J. M. Taylor, D. P. DiVincenzo, C. M. Marcus, M. P. Hanson, and A. C. Gossard, *Phys. Rev. B* **82**, 075403 (2010).
- [27] L. W. van Beveren, R. Hanson, I. Vink, F. Koppens, L. Kouwenhoven, and L. Vandersypen, *New J. Phys.* **7**, 182 (2005).
- [28] W. G. van der Wiel, S. De Franceschi, J. M. Elzerman, T. Fujisawa, S. Tarucha, and L. P. Kouwenhoven, *Rev. Mod. Phys.* **75**, 1 (2002).
- [29] M. G. House, H. Pan, M. Xiao, and H. W. Jiang, *Appl. Phys. Lett.* **99**, 112116 (2011).
- [30] L. DiCarlo, H. Lynch, A. Johnson, L. Childress, K. Crockett, C. Marcus, M. Hanson, and A. Gossard, *Phys. Rev. Lett.* **92**, 226801 (2004).
- [31] J. M. Elzerman, R. Hanson, L. H. Willems van Beveren, B. Witkamp, L. M. K. Vandersypen, and L. P. Kouwenhoven, *Nature* **430**, 431 EP (2004).
- [32] W. Pauli, *Phys. Rev.* **58**, 716 (1940).

- [33] A. C. Johnson, J. R. Petta, J. M. Taylor, A. Yacoby, M. D. Lukin, C. M. Marcus, M. P. Hanson, and A. C. Gossard, *Nature* **435**, 925 (2005).
- [34] Y. Nagaoka, *Phys. Rev.* **147**, 392 (1966).
- [35] P. W. Anderson, *Science* **235**, 1196 (1987).
- [36] E. Dagotto and T. M. Rice, *Science* **271**, 618 (1996).
- [37] J. Gray, A. Bayat, R. K. Puddy, C. G. Smith, and S. Bose, *Phys. Rev. B* **94**, 195136 (2016).

5

NAGAOKA FERROMAGNETISM OBSERVED IN A QUANTUM DOT PLAQUETTE

The analytical tractability of Nagaoka ferromagnetism makes it a convenient model to explore the capabilities of quantum simulators of collective electron interactions. However, the small ground-to-excited state energy compared to electron interactions, as well as the difficulty of measuring magnetization in few-particle devices, have made the Nagaoka model experimentally unattainable. Here we present experimental signatures of the ferromagnetic ground state, predicted for 3 electrons in a 4 site square plaquette, engineered using electrostatically defined quantum dots. We test the robustness of the Nagaoka condition under different scenarios of lattice topology, device homogeneity and magnetic flux through the plaquette. This long-sought demonstration of Nagaoka ferromagnetism establishes quantum dot systems as prime candidates for quantum simulators of magnetic phenomena driven by electron-electron interactions.

5.1. INTRODUCTION

The emergence of magnetism in itinerant electron systems presents a fascinating and challenging problem at the heart of quantum many-body physics [2, 3]. This may sound surprising since the most common ferromagnetic material—iron—is a metal. However, in iron, as well as many other materials including cobalt, nickel, manganite materials, magnetism is dominated by spins of nearly localized electrons, with conduction band electrons providing indirect exchange interactions. Going back to Stoner [4], simple models have been introduced to provide simple theoretical models for itinerant ferromagnetism. Here, magnetism must emerge from a delicate quantum mechanical interplay between the potential energy that can be saved through building appropriate symmetries and correlations into electronic wave functions, and the corresponding costs in kinetic energy. Despite their simplicity, the existence of ferromagnetic phases in these models remains a subject of considerable controversy [5]. The most recent experimental effort towards observing a ferromagnetic instability in itinerant Fermi systems has been undertaken with ultracold atoms [6], although the interpretation of those experiments has evolved in time [7]. On the theory side, there are only few rigorous theoretical results for itinerant magnetism, for instance in systems with special flat bands and Nagaoka's ferromagnetism (see Ref. [8] and references therein).

The Nagaoka model of ferromagnetism [9] relies on the simplicity of the Hubbard model [10], which captures complex correlations between electrons in a lattice using only two Hamiltonian parameters. Using this single-band model, Nagaoka proved analytically that for some lattice configurations and in the limit of very strong interactions, the presence of a single hole on top of a Mott insulating state with one electron per site renders the ground state ferromagnetic.

This elegant theoretical demonstration of ferromagnetism in the Hubbard model poses the question whether the ferromagnetic ground state will persist in an experimental setting, in the presence of long-range interactions and disorder, as well as additional available orbitals. The feasibility of performing a quantum simulation of Nagaoka ferromagnetism has been explored for quantum dots [11–13] as well as optical superlattices [14]. In spite of the maturity of quantum simulations of the Hubbard model, led by the cold atoms community [15], there has been no experimental observation of a high-spin ground state in an almost half-filled lattice or array of itinerant electrons—the smoking gun of Nagaoka ferromagnetism.

Electrostatically defined semiconductor quantum dots [16–18] have been gaining attention as excellent candidates for quantum simulations of the Hubbard model [19, 20]. Recent results have demonstrated the feasibility to extend these systems into 2D lattices [21–25]. The ability to reach interesting interaction regimes along with low temperatures, as well as the ability to perform spin correlation measurements, make quantum dot arrays particularly appealing for overcoming the challenges of observing evidence of Nagaoka ferromagnetism.

In this article, we present experimental signatures of Nagaoka ferromagnetism, using a quantum dot device designed to host a 2×2 lattice of electrons [24]. Using the high degree of parameter tunability, we study how external magnetic fields and disorder in local potentials affect the ferromagnetic ground state. Furthermore, by effectively tuning the geometry of the system from periodic to open boundary conditions, we experimentally

demonstrate the suppression of magnetism expected from the Lieb-Mattis theorem [26].

5.2. NAGAOKA MODEL IN THE QUANTUM DOT PLAQUETTE

The single-band Hubbard model provides a simple description of interacting electrons in a lattice, through a Hamiltonian that contains competing kinetic energy and electron-electron interaction terms:

$$\mathcal{H}_H = - \sum_{\langle i,j \rangle \sigma} t_{i,j} c_{i\sigma}^\dagger c_{j\sigma} + \sum_i U_i n_{i\uparrow} n_{i\downarrow} - \sum_i \mu_i n_i, \quad (5.1)$$

where $t_{i,j}$ is the matrix element accounting for electron tunneling between sites i and j , U_i is the on-site Coulomb repulsion energy on site i and μ_i is a local energy offset at dot i , which can be electrostatically controlled. The operators $c_{i\sigma}$, $c_{i\sigma}^\dagger$ and $n_{i\sigma}$ represent the second quantization annihilation, creation and number operators for an electron on site i with spin projection $\sigma = \{\uparrow, \downarrow\}$.

To study the conditions under which Nagaoka ferromagnetism can manifest itself on a square plaquette, we restrict the system to 3 electrons (i.e. one less than half filling), with nearest-neighbor only coupling and periodic boundary conditions (see schematic in inset of Fig. 5.1(a)). This case is analytically solvable [11] for homogeneous interactions ($U_i = U$, $t_{i,j} = t$, $\mu_i = 0$) and in the limit $U \gg t$, where the eigenstates have energies:

$$E_{3/2} = -2t \quad \text{and} \quad E_{1/2} = -\sqrt{3}t - \frac{5t^2}{U}, \quad (5.2)$$

where $E_{3/2}$ is the energy of the ferromagnetic quadruplets (with total spin $s = 3/2$ and spin projections $m = \{\pm 1/2, \pm 3/2\}$) and $E_{1/2}$ is the energy of the 2 sets of low-spin $s = 1/2$ doublets, which are degenerate in this model.

The simple Hamiltonian in Eq. (5.1) does not account for some of the essential features of the experimental device. For comparison with experimental results, we employ a more general model Hamiltonian, in which we account for interdot Coulomb repulsion (in Fig. 5.2(a)), spin-orbit and hyperfine interactions (in Fig. 5.3(b)), as well as the effects of external magnetic fields (in Fig. 5.5(a-b)). The implementation of these terms is described in detail in subsection 5.6.2. A detained ab initio calculation based on multiple orbitals solved from a potential landscape with 2x2 minima [1] also shows results very similar to those obtained with Eq. (5.1).

5.3. EXPERIMENTAL ACCESS TO THE NAGAOKA REGIME

The quantum dot plaquette (Fig. 5.1(a)) is formed by biasing metallic gates patterned on top of an AlGaAs/GaAs heterostructure, to control the local density of a 2-dimensional electron gas (2DEG) located 90 nm below the surface of the substrate. We use two additional nearby dots as charge sensors, to measure charge stability diagrams where we can observe charge tunneling events either between an electron reservoir and a dot, or between two dots in the plaquette. These diagrams (such as the one in Fig. 5.2(a)) allow us to map out the charge occupation of the system, as a function of voltage in the gates. The device is tuned to a regime where the system is loaded with 3 electrons, and the charge configuration energies of the electrons are resonant. We set the local energy reference at

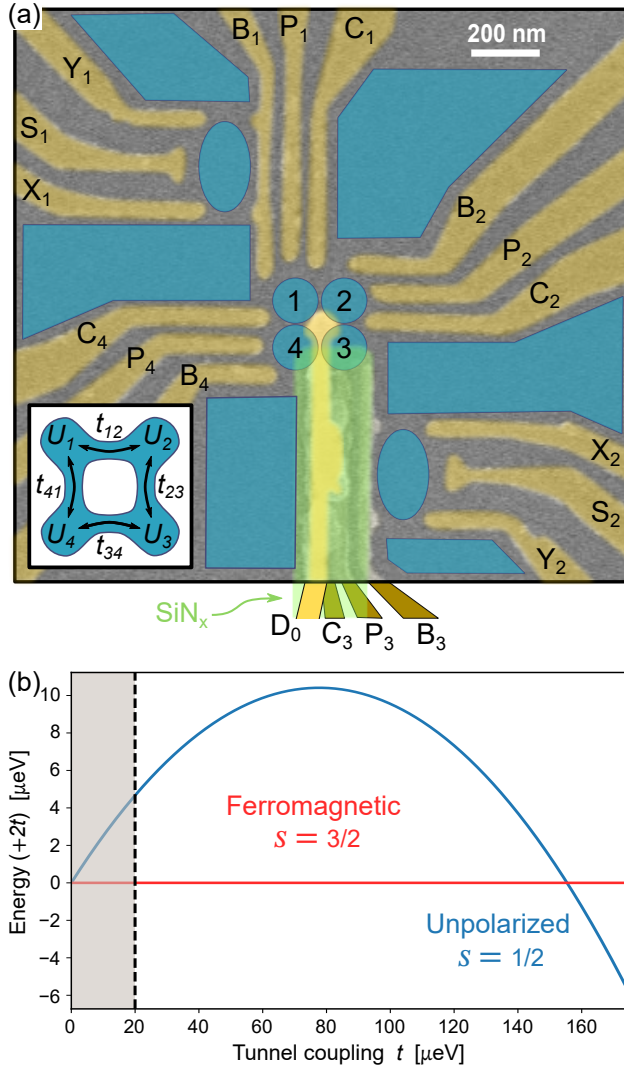


Figure 5.1: (a) False colored SEM image of a device from the same batch as the one used in the experiments. The gate structure used to define the quantum dots is colored in dark gold. A slab of silicon nitride (colored in green) is laid over gates C_3 and P_3 , to electrically isolate those gates from the D_0 gate (colored in bright gold) which runs over them and contacts the substrate at the center of the structure. A sketch of the expected 2DEG density in blue shows the 4 dots forming a plaquette in the center of the device, along with nearby charge sensors and electron reservoirs. (b) Energy spectrum as a function of tunnel coupling using the solution expressed in Eq. (5.2), with $U = 2.9$ meV. Shaded area shows the experimentally accessible range of t in this system.

this regime as $\mu_i(N) = 0$ eV for all dots, and refer to this condition as point N (see inset of Fig. 5.2(a)). Different features of the charge stability diagrams are also used to estimate the effective Hamiltonian parameters in our experimental system. The effective on-site interaction U_i is measured by extracting the local energy offset in dot i required to change the occupation from 1 electron to 2 electrons. The effective tunnel coupling term $t_{i,j}$ is measured by analyzing the width of the step in the charge sensing signal as the detuning between dots i and j is swept to transfer a single electron between them. Virtual gates provide knobs to effectively control the μ_i and $t_{i,j}$ parameters in the experimental system, by canceling the effects of cross-talk between gates. A more detailed description of the fabrication, operation, measurement protocols and implementation of the virtual gates can be found in the subsection 5.6.1 and in Ref. [24].

The simple model described by Eqs. (5.1) and (5.2) already provides some useful insight into the parameter regimes that are relevant to the experiment. The ferromagnetic state is the ground state at large U/t , with a transition to a low-spin ground state occurring at $U/t = 18.7$. The quantum dot array used in this work has an average $U \approx 2.9$ meV across the four sites, with tunable nearest-neighbor tunnel couplings in the range of $0 < t \lesssim 20$ μ eV. Unless otherwise stated, the couplings in these measurements are tuned to $t_{i,i+1} \approx 16$ μ eV. This means that we are probing the regime where the ground state is expected to be ferromagnetic and the transition to the low-spin state is out of experimental reach (see Fig. 5.1(b)). Moreover, the expected energy gap between the ferromagnetic and low-spin states in the system is $E_{1/2} - E_{3/2} \approx 4$ μ eV, which is comparable to the measured electron temperature $k_B T_e \approx 6$ μ eV (70 mK) [24]. This complicates the measurement, because we cannot distinguish the ground state of the system at equilibrium. Instead, we need to drive the system out of equilibrium in order to try to amplify the probability in the ground state. To this end, we have developed techniques to probe the different energy levels and probe the spin state of the system on timescales faster than the thermal relaxation.

Measurement protocol. Since the sensing dots are only sensitive to charge tunneling events, a spin-to-charge conversion protocol is needed in order to perform measurements of the spin state of the system. We do this at point M , where $\mu_i^M \approx [-2.5, 0.0, 1.0, -0.5]$ meV (see inset of Fig. 5.2(a)). There, the ground charge state is $[2, 0, 0, 1]$ (where $[n_1, n_2, n_3, n_4]$ corresponds to the number of electrons with dot number in the subscript), while the first excited charge state is $[1, 1, 0, 1]$. These states have an uncoupled spin in dot 4, with the remaining 2 spins in a singlet $|S\rangle$ (triplet $|T\rangle$) configuration for the ground (first excited) state. The charge stability diagram in Fig. 5.2(a) is simulated and measured (inset) using a gate combination that allows one to see both points N and M in the same diagram.

Fig. 5.2(b) shows the lowest three multiplets of the energy spectrum of the 3-electron system, along the line that connects point M to point N . Close to point M we see a typical double quantum dot spectrum corresponding to the $[2, 0, 0, 1] \leftrightarrow [1, 1, 0, 1]$ charge transition with the $|S\rangle$ and $|T\rangle$ branches, while in the region around point N the spins delocalize and we see branches corresponding to the quadruplets and doublets of the 3-electron system.

With this device, we can probe the spin state of the 3-electron system using the following protocol: 1 - repeatedly (10000 times) pulse rapidly from point N to point M , 2

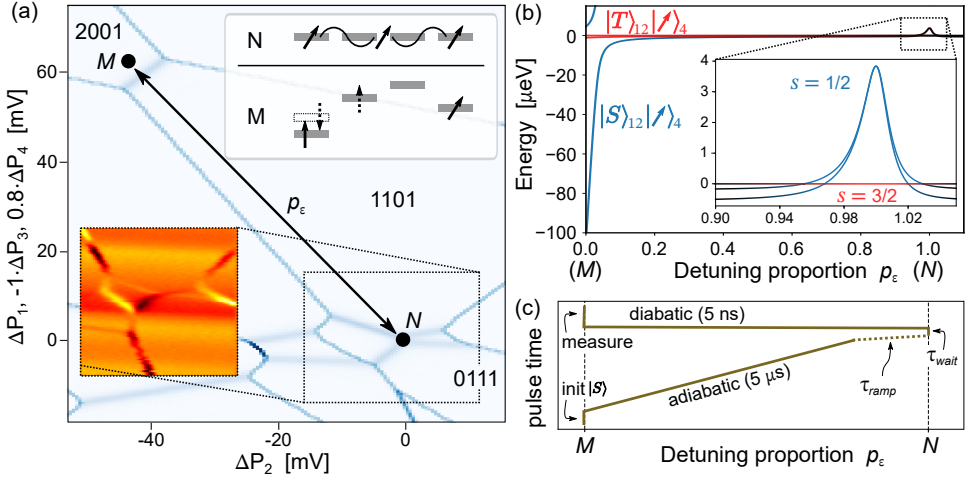


Figure 5.2: (a) Simulated charge stability diagram showing the approximate gate space used in the experiment. In the experiment we pulse in a straight line in gate space from point M to point N and back. Top-right inset shows a schematic of the local energies at points N and M , highlighting in the latter how the measurement of 2 spins in the singlet-triplet basis is performed through spin-to-charge conversion. Lower-left inset shows a measured charge stability diagram of the dotted region, with the same gate voltage ratios as the simulation, which we use in the experiment to calibrate the gate voltages at point N . (b) Calculated energy spectrum as a function of detuning proportion, using the theoretical model (Eq. (5.1) and supplementary text) without spin-coupling effects. Parameter values were set to $U_i = [2.9, 2.6, 2.9, 3.0]$ meV and $t_{i,j} = 16$ μeV , as extracted from the experiment. Inset shows a zoomed-in spectrum of the region where the 3 spins are delocalized on all 4 dots, where there are a total of 8 states: the $s = 3/2$ quadruplets (red) and the 2 sets of $s = 1/2$ doublets (blue), of which one set connects with the $|T\rangle$ branch and the other with the $|S\rangle$ branch at point M . Line colors represent the spin state of the system in each region, denoted by the labels in the figure. The energies extracted from the numerical solutions are offset by the energy of $|s, m\rangle = |3/2, +3/2\rangle$. (c) Pulse sequence used in the experiment (see main text for detailed description).

- for each repetition, perform single-shot $|S\rangle/|T\rangle$ measurements using dots 1 and 2 and taking 2 out of the 3 electrons, and 3 - extract the triplet probability P_T . Under ideal conditions, this constitutes a 2-spin projective measurement of the 3-electron system, resulting in $P_T^{(3/2)} = 1$ when the 3-electron system is in a ferromagnetic state (any of the $s = 3/2$ quadruplets). In the low-spin sector ($s = 1/2$), there are two sets of doublet states available, one of which projects 2 spins to $|S\rangle$, while the other projects to $|T\rangle$. In this system the doublets are effectively degenerate (see Fig. 5.2(b)), and their hybridization will result in $P_T^{(1/2)} = 0.5$ (see subsection 5.6.3 for detailed calculation).

Due to the low ratio of energy level splitting to temperature at point N , we cannot probe the ground state of the system by way of relaxation. Instead, we apply a gate pulse sequence that follows the detuning range shown in the energy spectrum plotted in Fig. 5.2(b). Using the pulse sequence drawn in Fig. 5.2(c), a 2-spin singlet state with a third, free spin sitting on dot 4, is initialized by waiting at point M for 500 μs . Next we apply simultaneous pulses to the P_i gates of different amplitudes, such that we effectively pulse along the ‘detuning proportion’ p_ϵ axis in Fig. 5.2(b) (see also the line along the charge stability diagram in Fig. 5.2(a)), defined such that $\mu_i(p_\epsilon) = (1 - p_\epsilon)\mu_i^M$. We then wait a time τ_{wait} at $\mu_i(p_\epsilon)$, before finally pulsing back to point M to perform

the measurement. Importantly, the level crossings seen in Fig. 5.2(b) are in fact avoided level crossings with spin-orbit and nuclear hyperfine mediated coupling between the spin states (see subsection 5.6.2). This avoided level crossing allows to probe the different states in the region around $p_e = 1$, by varying the ramp rate in the pulse sequence: a slow (fast) ramp rate results in an adiabatic (diabatic) passage through the avoided level crossings, so the ground (excited) state is reached. In practice, in order to avoid leakage to excited states along the way, 80% of the pulse is performed adiabatically, with the variable ramp time τ_{ramp} only for the remaining 20%. Varying τ_{wait} allows us to study the relaxation dynamics in the system. As long as τ_{wait} is shorter than the thermal relaxation time-scale, the measurement of P_T will be able to distinguish between ferromagnetic and low-spin states at point N .

5.4. MEASUREMENT RESULTS

Fig. 5.3(a) shows plots of $P_T(p_e)$ when we apply the experimental protocol described above. The inset of the figure shows the entire range of p_e , highlighting that P_T remains at a low value for most of the range, with a sharp increase as p_e approaches 1 (point N). This is consistent with expectation based on the energy spectrum plotted in Fig. 5.2(b), where the initialized singlet state is not subject to any energy-level crossing until the region close to point N , where the levels cross and the electrons become delocalized in the array, leading to a sharp increase in the observed P_T . The non-zero triplet fraction at low values of p_e is attributed partly to infrequent thermal excitations during the initialization stage—as a consequence of the finite electron temperature—and partly to a small probability of leakage to excited states during the pulse.

The main figure shows the measurement around point N , for a range of τ_{ramp} . In the region where $0.99 < p_e < 1.03$, a clear increase of P_T is observed as τ_{ramp} is increased, consistent with a gradual transition from diabatically pulsing into the low-spin state, to adiabatically pulsing into the ferromagnetic state, where P_T is maximum. For the faster pulses, we see ‘peaks’ of P_T at $p_e = 0.99$ and 1.03 , where the pulse reaches the energy-level crossings, as all the spin states can be expected to quickly (i.e., much faster than the experimental timescales) mix by the nuclear hyperfine fields and spin-orbit coupling [27–29].

From the τ_{ramp} timescale for the diabatic to adiabatic transition (see Fig. 5.3(b)) we can extract information about the spin-coupling mechanisms at the avoided crossings. To this end we have expanded the model in Eq. (5.1), to include the effects of spin-orbit interaction and the hyperfine induced magnetic field gradients (see subsection 5.6.2). The model suggests that the random hyperfine field gradients dominate the spin coupling present at the avoided level crossing (i.e., around $p_e \approx 0.97$). We can use the model to fit the data in Fig. 5.3(b), through time-evolution simulations (for details see subsection 5.6.2), from which we estimate a hyperfine coupling parameter $\delta_N = 73 \pm 3$ neV, defined as the standard deviation of the Gaussian probability distribution of the hyperfine field in each dot. The extracted δ_N is in agreement with previous observations and calculations, which have estimated 70 neV to 120 neV in similar GaAs quantum dot systems [29–31]. We note that the observed behavior can be qualitatively captured by a simple two-level Landau-Zener model (for details see subsection 5.6.2).

If we keep $p_e = 1$ fixed and vary the wait time τ_{wait} spent at point N , we observe

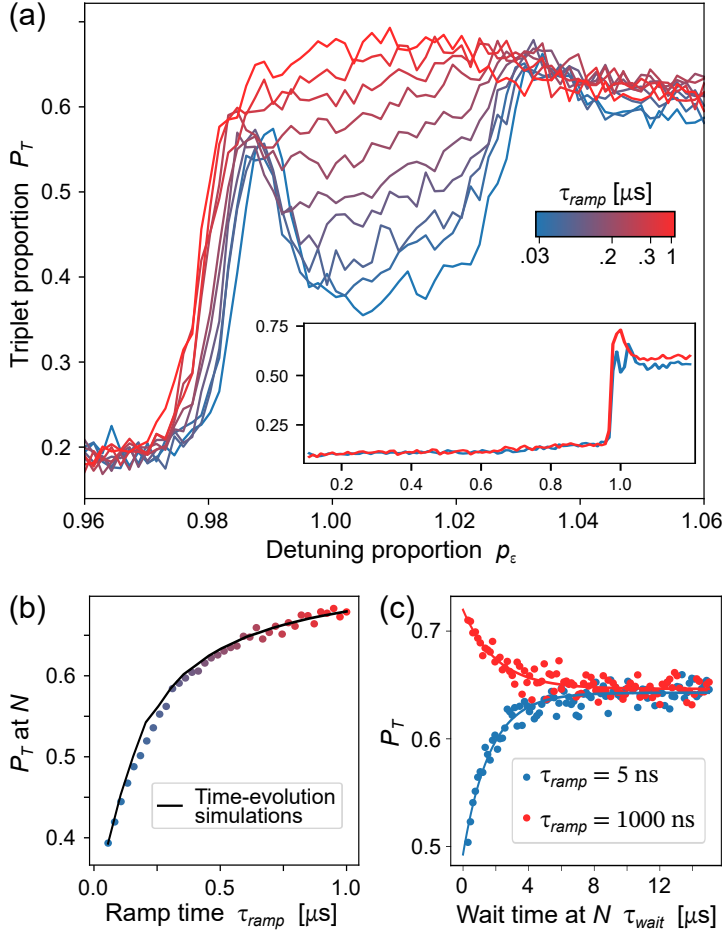


Figure 5.3: (a) Measured P_T vs p_ϵ using the protocol described in the main text. Different curves correspond to different values of τ_{ramp} . The main figure focuses on the region close to point N , while the inset is zoomed out to the entire detuning range, for the 2 extreme values of τ_{ramp} . τ_{wait} is fixed to 50 ns (500 ns) for the main figure (inset). (b) Average P_T in the detuning region $1.00 < p_\epsilon < 1.01$ for a set of 40 measurements within the same τ_{ramp} range shown in (a). The black line is a fit made via time evolution simulations in which we initialize a statistical mixture of the two lowest energy eigenstates at $p_\epsilon = 0.8$ and sweep the potentials to $p_\epsilon = 1$ at different rates. The fit has the hyperfine coupling parameter δ_N as a free fitting parameter, and the extracted P_T curve from the model is scaled and offset to match the data at the minimum and maximum value of τ_{ramp} , to account for measurement imperfections (see subsection 5.6.2 for details). (c) Thermal relaxation measurements. P_T is measured for increasing wait times at point N , for diabatic (dark) and adiabatic (light) passages. Solid lines are exponential fits as a guide to the eye.

relaxation of the $s = 1/2$ and $s = 3/2$ states, reflected in the decay of P_T to an intermediate level between the P_T observed for slow and rapid sweeps, at the shortest τ_{wait} (see Fig. 5.3(c)). This is consistent with thermal equilibration in the system, in which the electron temperature is comparable to the energy gap between the $s = 1/2$ and $s = 3/2$ states at point N . The thermal equilibration occurs on a timescale $\tau_{relax} \sim 2 \mu\text{s}$. We note that we cannot directly assign the values of P_T to $s = 1/2$ and $s = 3/2$ populations, because the observed P_T is subject to measurement imperfections caused by mechanisms that are difficult to disentangle, such as the finite measurement bandwidth, the signal to noise ratio and $|T\rangle$ to $|S\rangle$ relaxation, as well as unwanted leakage to other states during the pulsed passages.

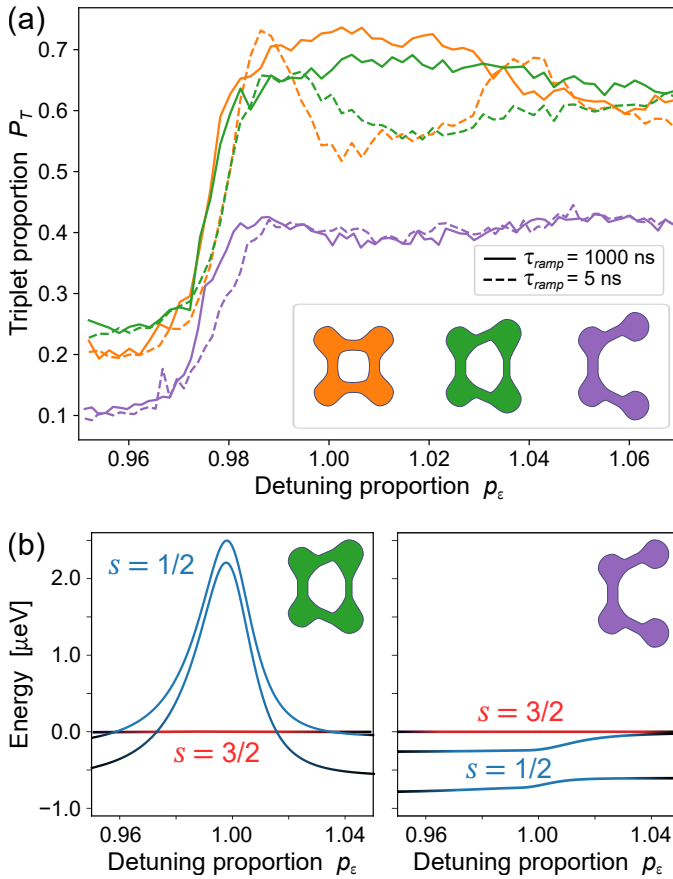


Figure 5.4: (a) Comparison of 3 measurements with the following values of tunnel couplings $[t_{12}, t_{23}, t_{34}, t_{41}]$ (in μeV): [18.6, 15.3, 17.4, 18.6](orange); [15.7, 7.9, 20.3, 19.0](green); [18.2, 0.0, 21.1, 20.7](purple). The offsets between the curves are not attributed to the topology, but are due to small measurement-to-measurement variations in the thermal excitation rate during the initialization stage of the protocol. (b) Calculated energy spectrum as a function of detuning proportion, using the tunnel coupling values corresponding to the green (left) and purple (right) plots from (a).

Boundary conditions and the Lieb-Mattis theorem. Considering that the square plaquette can be thought of as a 1D ring, the observation of a ferromagnetic ground state may appear to be in contradiction with the *Lieb-Mattis theorem* [26] which states that the ground state of a 1D array of electrons has the lowest possible spin. However, as later pointed out by Mattis himself [11] the Lieb-Mattis theorem was only proven for 1D chains with open boundary conditions, explicitly excluding arrays with periodic boundary conditions such as the case of the plaquette. We can intuitively understand the difference between these two configurations when we consider how the hole tunnels to its next-nearest neighbor [32]. In a 2D plaquette, the hole has 2 possible paths to the next-nearest neighbor. If the system is initialized in any of the $s = 1/2$ configurations, the 2 paths will leave the system in 2 different configurations. On the other hand, for an $s = 3/2$ system the 2 paths are identical, and interfere constructively to lower the kinetic energy of the system. In contrast, in an open boundary 1D array, the kinetic energy of the hole is independent of the spin configurations of the neighboring electrons (i.e., there is only one path for the hole to follow through the array), therefore the total energy of the system will obey the Lieb-Mattis theorem.

5

One powerful feature of the quantum dot system is that the tunnel barriers can be tuned independently, allowing us to test different array topologies. In Fig. 5.4 we compare diabatic and adiabatic sweeps, as we raise the tunnel barrier that controls t_{23} , effectively transforming the plaquette into a system that behaves more like the 1D system described by Mattis. In the latter regime, we see that P_T becomes insensitive to sweep rate. Additionally, we no longer observe the peaks of P_T for the fast sweep rate, which we had associated with mixing at the avoided level crossings. From these observations we infer that for the open chain, the instantaneous ground state does not exhibit an avoided crossing between an $s = 1/2$ state and an $s = 3/2$ state as the system is taken to point N. This interpretation is also consistent with the numerical simulations of the energy spectrum shown in Fig. 5.4(b).

Destroying ferromagnetism with magnetic fields. Given that Nagaoka ferromagnetism can be explained through interference effects due to the trajectories of the hole around the ring, it then follows that a magnetic flux through the plaquette will add an Aharonov-Bohm phase [33] that disturbs the interference effects. We capture this effect in the theoretical model by modifying the second term in Eq. (5.1) as : $-\sum_{\langle j,k \rangle \sigma} t_{j,k} \exp(-i\varphi_{jk}) c_{j\sigma}^\dagger c_{k\sigma}$ (see subsection 5.6.2). We use the gauge in which $\varphi_{41} = \frac{2\pi\Phi}{\Phi_0}$, where $\Phi = B\ell^2$ is the flux generated by a magnetic field B through the plaquette with estimated distance between nearest-neighbor dots ℓ , and $\Phi_0 = h/e$ is the flux quantum. Using this gauge, the phases for the other links vanish. In addition, the application of an external field subjects the system to the Zeeman effect, causing a spin-dependent energy offset $E_Z = g\mu_B B m$ to each eigenstate, where $g = -0.4$ is the electron g -factor in GaAs and μ_B is the Bohr magneton.

Fig. 5.5(a) shows the effect of the magnetic flux on the spectrum, ignoring the Zeeman effect. The lowest $s = 1/2$ and $s = 3/2$ levels at point N are shown as a function of the applied field, where periodic crossings can be observed. In the range $30 < B < 160$ mT, the system ground state transitions to the low-spin state, with the – perhaps counterintuitive – implication that we can destroy the ferromagnetic state by applying a magnetic

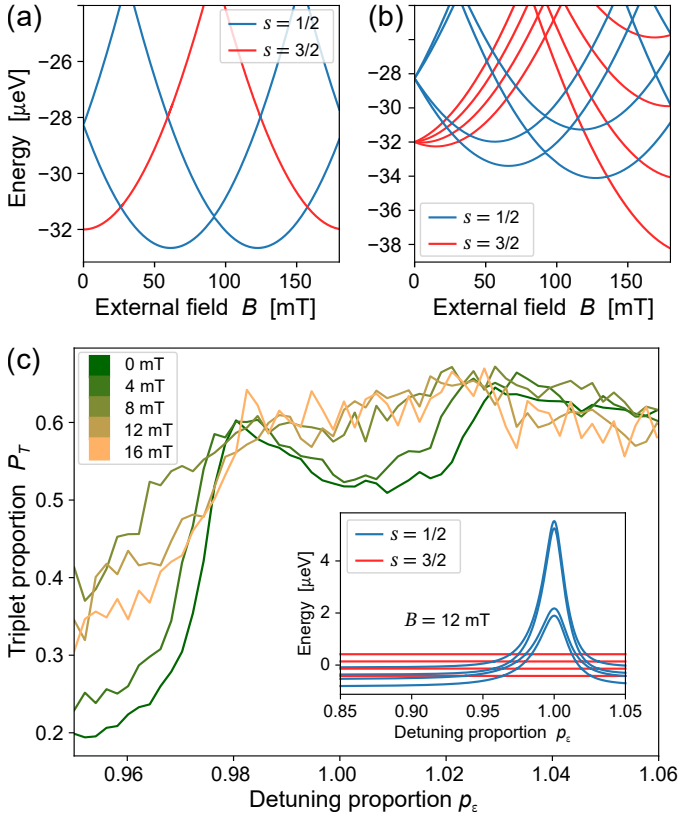


Figure 5.5: (a) Lowest eigenenergies of the $s = 1/2$ (blue) and $s = 3/2$ (red) states at point N as a function of the magnetic field, obtained from the numerical model after including the effect of an Aharonov-Bohm phase (details in subsection 5.6.2). (b) Same as (a) but with the addition of the Zeeman effect, and the lowest 4 eigenenergies of each s states are shown. (c) Experimental measurement using diabatic passage, for different fields in the range of 0 to 16 mT. Inset shows a numerically calculated spectrum at 12 mT, with the Aharonov-Bohm phase and Zeeman effect included in the model.

field. Additionally, this effect highlights that the ferromagnetic state in this system is dominated by the Nagaoka effect and not by long-range interactions. Indeed, the ab initio calculations suggest that long-range interactions only account for $\sim 20\%$ of the ferromagnetic polarization. When we include the Zeeman effect (see Fig. 5.5(b)) the picture becomes more complicated, because both Zeeman and orbital effects cause perturbations of similar energy scales.

From this initial numerical analysis, it is clear that the experimental characterization of the applied external field will be challenging, due to the increased complexity of the spectral structure of the spin states as a function of field. The small energy splittings that appear both at point N , as well as at lower p_e values (see inset of Fig. 5.5(c)) are expected to cause mixing of the spin states during the adiabatic pulses. To minimize this mixing, we adjusted the pulsing protocol such that we pulse adiabatically ($1 \mu\text{s}$ ramp) to $p_e = 0.2$,

then pulse diabatically (5 ns ramp) the rest of the way. The results in Fig. 5.5(c) show that from 4 to 8 mT P_T increases at point N, and we stop observing the characteristic dip. Note that the range of field that we were able to probe is still below the estimated ground state transition point (~ 30 mT). Therefore, we infer that the observed increase in P_T is the effect of hybridization of the $s = 1/2$ and $s = 3/2$ states as their energy gap reduces. We cannot claim that the observed hybridization of states is occurring solely at point N, as it is evident from the increase in P_T at $p_\epsilon < 0.97$ (i.e. prior to the energy-level crossings) that some of the mixing is occurring during the pulse. However, we do see that P_T in all plots converge at the energy-level crossings ($p_\epsilon \approx 0.97$ and $p_\epsilon \approx 1.03$) suggesting that the Aharonov-Bohm orbital effects are partly responsible for the additional mixing in the region around point N.

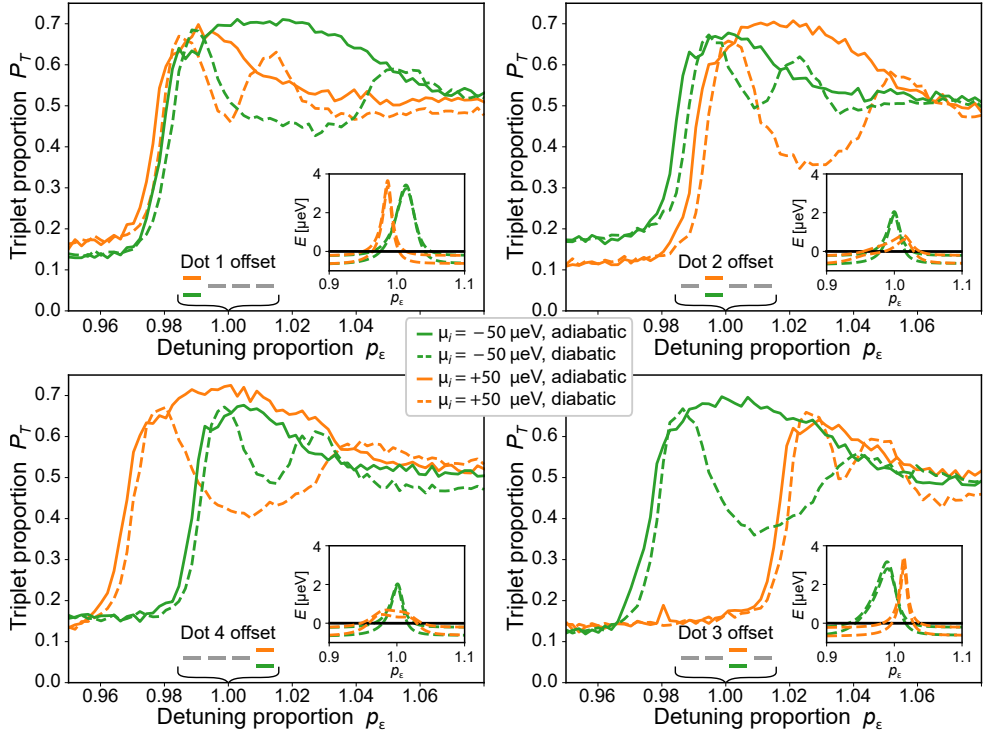


Figure 5.6: Experimental measurements with point N purposefully redefined to have a $\pm 50 \mu\text{eV}$ offset on each of the 4 dots. Panels correspond to offsets in dots 1 to 4, clockwise from the top-left. Insets show numerically calculated spectra for the same experimental condition.

Sensitivity to local energy offsets. We also use the tunability available in quantum dot systems to study the effects of disorder of the local potential present in each dot. For the plots in Fig. 5.6, we modified the experimental protocol used to probe the states at point N, pulsing instead to a point N' , where the local energy of one of the dots is offset by $\pm 50 \mu\text{eV}$. We can do this by employing the *virtual gates* technique [20, 24], which gives

access to control knobs that map a linear combination of P_i gates onto local dot energy offsets. The insets of the panels in Fig. 5.6 show the expected energy spectra when we simulate the experimental conditions using the model in Eq. (5.1). The spectra show that for all cases there remains a region in the detuning trajectory where the ferromagnetic state is the ground state, but both the width and the position of this region around point N' varies with the different local offsets applied. The experimental results in the main panels show excellent qualitative agreement with the variations observed in the calculated spectra, further confirming the validity of the experimental protocol. Remarkably, we have also pushed the offset of dot 1 to the range 100 to $-800 \mu\text{eV}$ and the system still shows signs of the ferromagnetic ground state (Fig. 5.7).

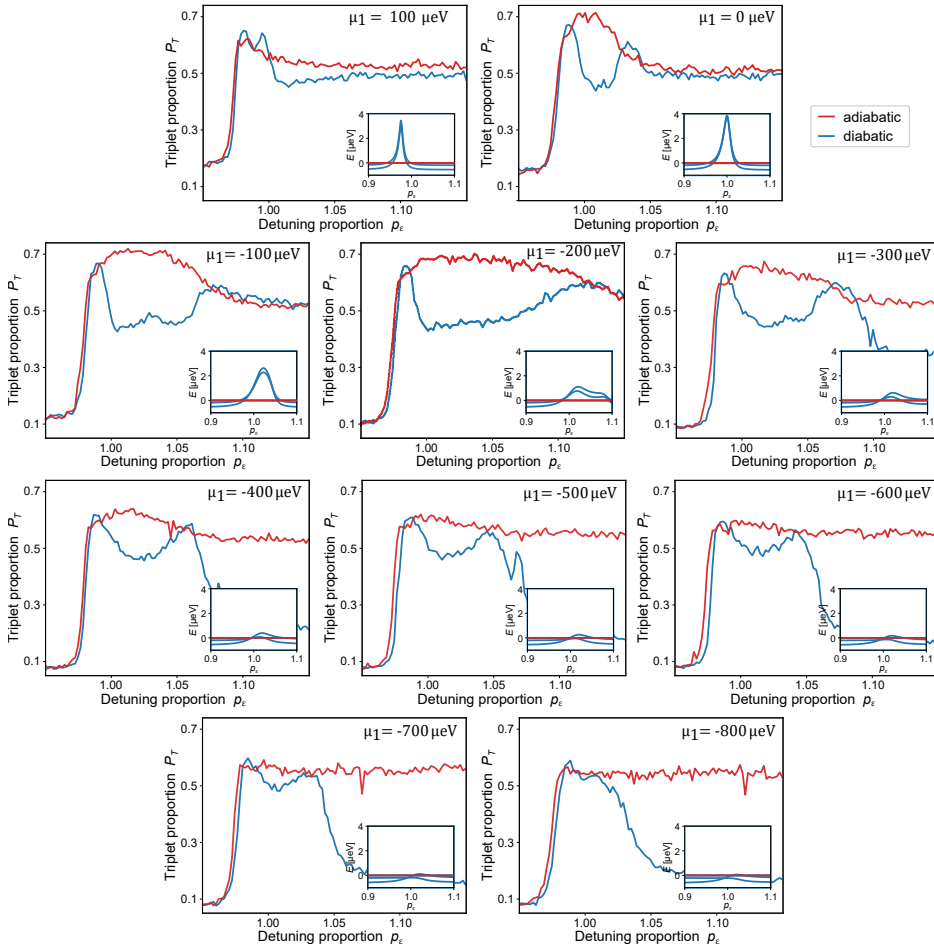


Figure 5.7: Each panel experimental measurements comparing adiabatic and diabatic passages (as explained in the main text), where point N has been redefined such that the chemical potential of dot 1 is offset by the amount shown on the top right of each panel. Insets show simulated spectra using the same local offset conditions as the experiment of the corresponding panel.

5.5. DISCUSSION

In this work, we have presented the first measurements showing experimental evidence of Nagaoka's 50-year old theory in a small scale system. The large degree of tunability, high ratio of interaction strength to temperature, and fast measurement techniques available to quantum dot systems allowed observing both the ferromagnetic ground state and the low-spin excited state of an almost-half-filled lattice of electrons. Even though the problem of 3 electrons in a 4-site plaquette can be solved analytically using the Hubbard picture, a complete description of this experimental system that includes all its available orbitals is not easily tractable, analytically or numerically. Indeed, the computational cost of the *ab initio* calculation [1], with all interaction terms being considered, is on the order of 10000 CPU hours. In addition, this small scale quantum simulation provides value beyond proof-of-principle in two important ways. First, by performing a quantum simulation involving charge and spin states, it builds on previous demonstrations [20] that quantum dot systems can be useful simulators of the Hubbard model, despite their inhomogeneities in the potential shape and local energies. Additionally, small scale simulations on tractable models can be used to systematically benchmark the performance of devices as the scale-up technology develops towards devices that can perform classically intractable simulations. Finally, in this work, we showed a flavor of the capabilities for studying the sensitivity to disorder, and these experiments already revealed some surprising effects, when we found that the Nagaoka condition can still be observed after offsetting a local energy by amounts much larger than the tunnel coupling. This can readily be studied in further detail, along with other possibilities for exploring the effects of disorder, which could bring insights into e.g., the stability of the ferromagnetic state.

This experiment is an important step forward in answering the question of whether itinerant magnetism can occur in real systems. Larger realizations of similar quantum dot systems (or any other experimentally controllable system), such as $2 \times N$ or $M \times N$ arrays can shed more light on the discussion. As the system becomes larger the exchange interaction grows proportionally to the system size, creating a competition against the hopping energy that is characteristic of Nagaoka ferromagnetism, and leaving the fate of the Nagaoka mechanism in larger systems in the realm of the unknown.

5.6. ADDITIONAL MATERIAL

5.6.1. DEVICE FABRICATION AND METHODS

The experiment was performed using an array of four gate-defined quantum dots in a 2×2 geometry. We employed a double-layer gate-structure to form this dot array. The first layer of gates—which includes all gates except D_0 —was created using electron-beam lithography, evaporation, and lift-off of Ti/Au with 5/20 nm thickness (see Fig. 1(a) of the main text). We then fabricate a $1.5 \times 0.2 \mu\text{m}$ dielectric slab on top of the gates C_3 and P_3 , using electron-beam lithography, sputtering and lift-off of SiN_x slab with 50 nm thickness. Finally, the D_0 gate is created using the same process as the other gates, with 10/100 nm thick Ti/Au. This gate runs over the gate C_3 before contacting the substrate at the center of the dot array. The gates created in the first layer are 30 nm wide, whereas the width of the D_0 gate is 100 nm.

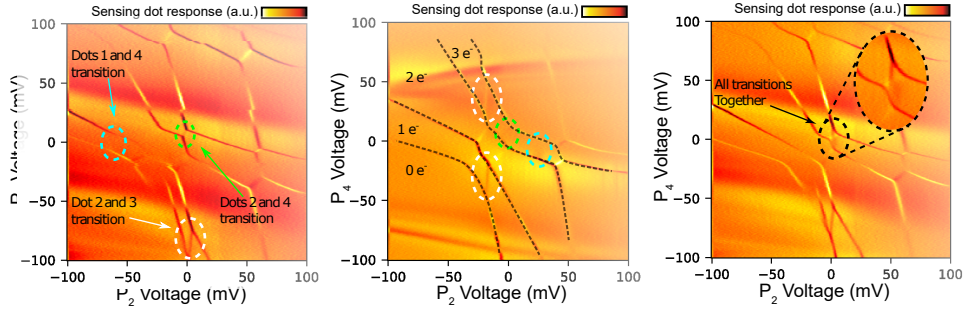


Figure 5.8: Sample stability diagrams showing how we tune to the Nagaoka condition. We have highlighted the visible interdot transitions (identified in the right panel), where the electrochemical potentials of two dots become resonant (i.e., an electron is allowed tunnel between the two dots). In the center panel, dashed black lines delimit the regions with a fixed total electron occupation in the system. From the left to right panels, we gradually tune the gate voltages in order to reach the Nagaoka condition, where the three visible interdot transitions are aligned in the three-electron configuration (right panel). The intersite interaction in the system provides an effective isolation from the reservoirs for a narrow range of gate voltages, such that the system can remain stable with three electrons in the resonant configuration.

Different parameters of the dot array can be controlled using voltages on different gates. The P_i gates are designed to control the electron filling of dot i by adjusting the dot chemical potential μ_i . Gates D_0 and C_i are designed to control the tunnel coupling $t_{i,j}$, while gates B_i and C_{i+1} are designed to control the coupling between dot i and its reservoir. In reality, the proximity between the gates causes non-negligible cross capacitances, preventing independent control of the parameters that the gates were designed to control. For some of the tuning stages, we make use of linear combination of gate voltages – known as *virtual gates* [20, 24] – to provide a direct experimental knob to the parameter of interest. We use charge stability diagrams [17] to identify the charge state of the system as a function of different P_i voltages. These diagrams are also used to measure and tune the effective $t_{i,j}$ parameters independently, using the technique described in detail in Refs. [20, 24], which requires analyzing the interdot transition of a single electron across dots i and j .

In order to observe signatures of Nagaoka ferromagnetism, we need to tune the system such that it is loaded with three electrons isolated from the reservoirs and these three electrons must be itinerant in the four dot system. In Fig. 5.8, we show some sample charge stability diagrams and describe the tuning method used to tune the gate voltages to identify point N . To tune $t_{i,i+1}$ close to point N , we first localize 2 of the electrons in dots $i+2, i+3$ (i.e. by slightly lowering μ_{i+2}, μ_{i+3}), and keep dots $i, i+1$ resonant using the remaining electron to measure their tunnel coupling. Here we use cyclic dot indices with $i = \{1, 2, 3, 4\}$.

Next, we identify the gate voltages suitable to perform the two spin projection measurement (point M in Fig. 2(a) in the main text). Once we have identified point M and fine-tuned the gates to optimize the spin-readout fidelity, we define a linear combination of P_i voltages that joins the points M and N by a straight line in gate voltage space. This virtual gate enables us to probe the system along the ‘detuning proportion’ p_c axis

in Fig. 2(b) in the main text.

5.6.2. EXTENDED FERMI-HUBBARD MODELS USED TO SIMULATE DIFFERENT EXPERIMENTS IN THE MAIN TEXT

In this section we will describe the different parameters that are included in the model Hamiltonians that we refer to in the main text for analytical and numerical simulations. We begin with the simplest Fermi-Hubbard model of a 2×2 site plaquette with 3 electrons, and add from there different parameters as we increase the complexity of the model. The simplest Hamiltonian we describe (\mathcal{H}_0) has been solved analytically with the aid of *Mathematica*. The more complex Hamiltonians in the following subsections were solved numerically, using mainly the eigensolvers from the *Python*-based *Scipy* package, with the exception of the time-evolution simulations, which were solved using an in-house solver package [34].

Representation of the quantum states. We represent the quantum states on the 2×2 plaquette as

$$|\psi\rangle = \sum_{\{n_{i\sigma}\}} a(\{n_{i\sigma}\}) |\{n_{i\sigma}\}\rangle. \quad (5.3)$$

The basis consists of the states specified by the occupations of the electrons on the lattice and their spin projections:

$$|\{n_{i\sigma}\}\rangle = |n_{1\uparrow} n_{2\uparrow} n_{3\uparrow} n_{4\uparrow} n_{1\downarrow} n_{2\downarrow} n_{3\downarrow} n_{4\downarrow}\rangle, \quad (5.4)$$

with $n_{i\sigma} = 0$ or 1. For N electrons on the plaquette we have $\sum_{i\sigma} n_{i\sigma} = N$ and the basis states consist of all combinations of the occupations at fixed N . Hence $N = 3$ corresponds to a space of the quantum states of dimension $8!/5!3! = 56$.

The on-site energy and the Coulomb repulsion terms of the Hamiltonian $\sum_i U_i n_{i\uparrow} n_{i\downarrow} - \sum_i \mu_i n_i$ are diagonal in this basis. Tunneling involves the off-diagonal matrix elements [35]:

$$\langle \dots 1_{i\sigma} \dots 0_{j\sigma'} \dots | c_{i\sigma}^\dagger c_{j\sigma'} | \dots 0_{i\sigma} \dots 1_{j\sigma'} \dots \rangle = (-1)^{\sum_{\ell=i\sigma+1}^{j\sigma'-1} n_\ell}, \quad (5.5)$$

where ℓ goes over the elements between $i\sigma$ and $j\sigma'$ (exclusive) in the list (5.4). The Hamiltonian commutes with the spin operators \mathbf{S}^2 and S_z and its eigenstates are also spin eigenstates $|s, m\rangle_\alpha$:

$$\begin{aligned} \mathbf{S}^2 |s, m\rangle_\alpha &= s(s+1) |s, m\rangle_\alpha, \\ S_z |s, m\rangle_\alpha &= m |s, m\rangle_\alpha, \quad m = -s, -s+1, \dots, s. \end{aligned} \quad (5.6)$$

The spin operators are $\mathbf{S}^2 = S_z^2 + \frac{1}{2}(S_+ S_- + S_- S_+)$, $S_z = \frac{1}{2} \sum_i (n_{i\uparrow} - n_{i\downarrow})$, $S_+ = \sum_i c_{i\uparrow}^\dagger c_{i\downarrow}$, and $S_- = \sum_i c_{i\downarrow}^\dagger c_{i\uparrow}$. The label α distinguishes between the states with the same quantum numbers s and m . For three electrons in the absence of a magnetic field those states consist of energy degenerate $s = 3/2$ quadruplets and two sets of energy degenerate $s = 1/2$ doublets. In the low-energy sector relevant to the study, α distinguishes between the two sets of $s = 1/2$ doublets.

Basic construction of the 3-electron filled plaquette Fermi-Hubbard Hamiltonian. In the simplest version of the model, the system is constrained to having 3 electrons and each dot can be occupied with at most 2 electrons, subject to Pauli exclusion (i.e. double occupation of a dot must be of opposite spin). For this section, the on-site interaction U and tunnel coupling t are taken to be equal for all sites. For now we do not consider any spin coupling or spin-dependent splitting, therefore the Hamiltonian can be divided into two independent blocks, one for the $m = \pm 3/2$ states (parallel spins) and another for the $m = \pm 1/2$ states (one flipped spin):

$$\mathcal{H}_0 = \mathcal{H}_{3/2} + \mathcal{H}_{1/2} \quad (5.7)$$

and for each block it is sufficient to solve for one of the m projections and assume another degenerate set of states for the opposite m projection. As will be shown, these assumptions reduce the dimensions of the Hamiltonians to 4 for $\mathcal{H}_{3/2}$ and 24 for $\mathcal{H}_{1/2}$, making them simpler to solve analytically.

The quantum states for $\mathcal{H}_{3/2}$ will be

$$|\psi_{3/2}\rangle = a_1|0\uparrow\uparrow\rangle + a_2|\uparrow 0\uparrow\rangle + a_3|\uparrow\uparrow 0\rangle + a_4|\uparrow\uparrow\uparrow 0\rangle \quad (5.8)$$

with the Hamiltonian

$$\mathcal{H}_{3/2} = \begin{bmatrix} 0 & -t & 0 & -t \\ -t & 0 & -t & 0 \\ 0 & -t & 0 & -t \\ -t & 0 & -t & 0 \end{bmatrix} \quad (5.9)$$

with eigenvalues $\{-2t, 0, 2t\}$.

For the block with $m = \pm 1/2$, double occupation is allowed, therefore we need to consider more available states. We construct the Hamiltonian by first fixing the flipped spin in one dot and working out all the possible states in the basis. For example, a down spin in dot 1 results in the basis sub-set

$$|\psi'_{1/2}\rangle = a_1|2\uparrow 00\rangle + a_2|20\uparrow 0\rangle + a_3|200\uparrow\rangle + a_4|\downarrow 0\uparrow\rangle + a_5|\downarrow\uparrow 0\rangle + a_6|\downarrow\uparrow\uparrow 0\rangle \quad (5.10)$$

from which we then construct

$$\mathcal{H}'_{1/2} = \begin{bmatrix} U & -t & 0 & 0 & t & 0 \\ -t & U & -t & -t & 0 & t \\ 0 & -t & U & 0 & -t & 0 \\ 0 & -t & 0 & 0 & -t & 0 \\ t & 0 & -t & -t & 0 & -t \\ 0 & t & 0 & 0 & -t & 0 \end{bmatrix} \quad (5.11)$$

The same matrix can be used for the subspace with the flipped spin on each of the other dots. To finish constructing the 24-dimensional Hamiltonian, we need to then work out

the hopping matrices for the spin down, which results in the full Hamiltonian:

$$\mathcal{H}_{1/2} = \begin{bmatrix} \mathcal{H}'_{1/2} & \mathbf{T} & 0 & \mathbf{T}^\top \\ \mathbf{T}^\top & \mathcal{H}'_{1/2} & \mathbf{T} & 0 \\ 0 & \mathbf{T}^\top & \mathcal{H}'_{1/2} & \mathbf{T} \\ \mathbf{T} & 0 & \mathbf{T}^\top & \mathcal{H}'_{1/2} \end{bmatrix} \quad \text{where} \quad \mathbf{T} = \begin{bmatrix} 0 & 0 & t & 0 & 0 & 0 \\ 0 & 0 & 0 & 0 & t & 0 \\ 0 & 0 & 0 & 0 & 0 & t \\ -t & 0 & 0 & 0 & 0 & 0 \\ 0 & -t & 0 & 0 & 0 & 0 \\ 0 & 0 & 0 & -t & 0 & 0 \end{bmatrix} \quad (5.12)$$

The lowest two eigenvalues of this Hamiltonian are $-2t$ (two states) and $-\sqrt{3}t - \frac{5t^2}{U}$ (four states). The former correspond to the $m = \pm 1/2$ states of the quadruplets with total spin $s = 3/2$. The remaining four states correspond to the two $s = 1/2$ doublets (with $m = \pm 1/2$).

As expected for a 3-spin system, the 8 lowest eigenenergies of this Hamiltonian contain 4 degenerate ferromagnetic quadruplets and the 2 sets of degenerate low-spin doublets.

5

Site specific parameters and local energy offsets. The first increase in the level of complexity for the model is to make the parameters site specific (U_i and $t_{i,j}$), as well as to add site specific local energy offsets μ_i . The resulting Hamiltonian

$$\mathcal{H}_1 = - \sum_{\langle i,j \rangle \sigma} t_{i,j} c_{i\sigma}^\dagger c_{j\sigma} + \sum_i U_i n_{i\uparrow} n_{i\downarrow} - \sum_i \mu_i n_i \quad (5.13)$$

can be constructed in similar way as described above, with the addition of the corresponding diagonal μ_i elements. We numerically solve this Hamiltonian to obtain the p_e dependent energy spectra shown in the main manuscript.

Spin coupling terms. In order to capture the τ_{ramp} dependence of our experiments, we have added to the model the effects of spin-orbit coupling and hyperfine interactions, the two most important mechanisms that lead to spin flipping in GaAs [36]. Since we are now considering spin coupling, we need the full quantum state representation with the 56-dimensional Hamiltonian.

For the quantum dot plaquette we have computed the matrix elements of the spin-orbit coupling Hamiltonian that accounts for the Bychkov-Rashba and the Dresselhaus effects for GaAs grown in the the crystallographic direction [001]:

$$\mathcal{H}_{so} = \alpha(p_x \sigma_y - p_y \sigma_x) + \beta(-p_x \sigma_x + p_y \sigma_y). \quad (5.14)$$

here $\alpha = e\gamma_b \langle \mathcal{E} \rangle / \hbar$ and $\beta = \gamma_d \langle k_z^2 \rangle / \hbar$ where $e > 0$ is the elementary charge, and \mathcal{E} is the electric field at the interface of the structure. For GaAs $\gamma_b \approx 5.2 \times 10^{-2} \text{ nm}^2$ and $\gamma_d \approx 27.6 \text{ meV.nm}^3$ [37]. The axes of the coordinate system x and y correspond to the directions [100] and [010]. When spin-orbit coupling is weak we may take as a basis the Wannier states $|j\rangle$ that are localized on the dots indexed by j . In this basis the matrix elements of Eq. (5.14) are

$$\langle j | \mathcal{H}_{so} | k \rangle = \alpha(p_x^{jk} \sigma_y - p_y^{jk} \sigma_x) + \beta(-p_x^{jk} \sigma_x + p_y^{jk} \sigma_y), \quad (5.15)$$

where $p_a^{jk} = \langle j|p_a|k\rangle$, $a = x, y$. Those matrix elements vanish if $j = k$. Then in the second quantized form Eq. (5.14) reads

$$\mathcal{H}_{so} = \sum_{jk\sigma\sigma'} c_{j\sigma}^\dagger \omega^{jk} \cdot \sigma^{\sigma\sigma'} c_{k\sigma'}, \quad (5.16)$$

with $\omega^{jk} \cdot \sigma^{\sigma\sigma'} = (-\alpha p_y^{jk} - \beta p_x^{jk})\sigma_x^{\sigma\sigma'} + (\alpha p_x^{jk} + \beta p_y^{jk})\sigma_y^{\sigma\sigma'}$. The unit vector in the direction of the dots j and k is $\hat{\ell}_{jk} = \cos(\theta_{jk})\hat{x} + \sin(\theta_{jk})\hat{y}$. Eliminating the matrix elements of the momentum in the direction perpendicular to $\hat{\ell}_{jk}$, Eq. (5.16) becomes

$$\mathcal{H}_{so} = \sum_{jk\sigma\sigma'} c_{j\sigma}^\dagger p_\ell^{jk} ((-\alpha \sin(\theta_{jk}) - \beta \cos(\theta_{jk}))\sigma_x^{\sigma\sigma'} + (\alpha \cos(\theta_{jk}) + \beta \sin(\theta_{jk}))\sigma_y^{\sigma\sigma'}) c_{k\sigma'}. \quad (5.17)$$

Here $p_\ell^{jk} = m\langle j|\ell|k\rangle = imt_{jk}\ell_{jk}/\hbar$, where m is the effective mass of the electron, $\ell_{jk} = \ell_j - \ell_k$ with ℓ_j the coordinate of dot j on the (jk) axis, and t_{jk} equals minus the matrix element of the one-electron Hamiltonian. Therefore

$$\mathcal{H}_{so} = \sum_{(j,k)} t_{jk} c_{j\uparrow}^\dagger \left(\frac{\ell_{jk}}{\lambda_b} e^{-i\theta_{jk}} - i \frac{\ell_{jk}}{\lambda_d} e^{i\theta_{jk}} \right) c_{k\downarrow} + h.c., \quad (5.18)$$

where jk are restricted to neighboring dots and we define the length scales $\lambda_b = \hbar/m\alpha$ and $\lambda_d = \hbar/m\beta$. Typically $\langle k_z^2 \rangle \sim 0.02 \text{ nm}^{-2}$ and $\langle e\mathcal{E} \rangle \sim 3 \text{ meV/nm}$. So $\lambda_b \approx 7 \mu\text{m}$ and $\lambda_d \approx 2 \mu\text{m}$, for neighbor quantum dots ($\ell_{jk} \approx 0.15 \mu\text{m}$), giving $\ell_{jk}/\lambda_b \sim 0.02$ and $\ell_{jk}/\lambda_d \sim 0.08$.

The large abundance of nuclear spins in the GaAs crystal means that each site in the plaquette will be hyperfine coupled to a number of randomly oriented nuclear spins, causing each site to experience a slightly different Overhauser field. This interaction is described by the hyperfine coupling Hamiltonian [18, 27, 28]:

$$\mathcal{H}_{hf} = \mathbf{S} \cdot \mathbf{h}_N. \quad (5.19)$$

Here $\mathbf{S} = (\sigma_x, \sigma_y, \sigma_z)/2$ is the electron spin operator, $\mathbf{h}_N = \sum_i A_i \mathbf{I}_i$, $A_i = Av_0|\psi(\mathbf{r}_i)|^2$ is the coupling parameter with nucleus i having spin operator \mathbf{I}_i , $\psi(\mathbf{r}_i)$ is the electron envelope wave function at the nuclear site \mathbf{r}_i , and v_0 is the volume of the crystal cell. Hence $\mathbf{B}_N = \mathbf{h}_N/g\mu_B$ is the nuclear magnetic field acting on the electron with g -factor g , and μ_B is the Bohr magneton.

The classical probability distribution of h_{Na} ($a = x, y$ or z) is normal [27, 28]: $P(h_{Na}) = \frac{1}{\sqrt{2\pi\delta_N^2}} \exp(-h_{Na}^2/2\delta_N^2)$. The typical magnitude of the field component is $\delta_N \sim A/\sqrt{N} \ll h_{N\text{max}} \sim A$, with N the number of nuclei covered by the envelope function of the electron and $h_{N\text{max}}$ the magnitude of the field when the nuclear spins are fully polarized. For GaAs: $N \sim 10^6$ and $B_{N\text{max}}/\sqrt{N}$ is of the order of a few mT [18], hence $h_{N\text{max}}/\sqrt{N} \sim 0.1 \mu\text{eV}$.

Since our basis states are eigenstates of the Pauli matrix σ_z , we express Eq. (5.19) as:

$$\mathcal{H}_{hf} = \frac{1}{2} (\sigma_z h_{Nz} + \sigma_+ (h_{Nx} - ih_{Ny}) + \sigma_- (h_{Nx} + ih_{Ny})), \quad (5.20)$$

where $\sigma_{\pm} = (\sigma_x \pm i\sigma_y)/2$. We numerically implement Eq. (5.20) and the nuclear fields of the four quantum dots are taken to be independent. In Fig. 5.9(a-c) we show that the effect of the hyperfine coupling dominates over spin-orbit coupling, in the detuning region of the energy level crossings.

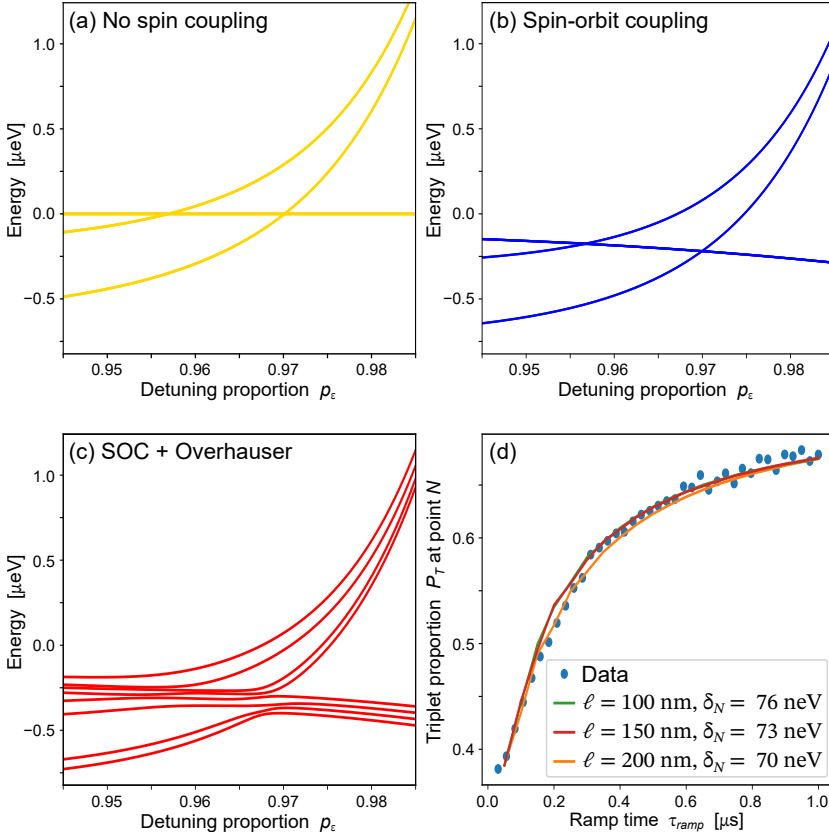


Figure 5.9: (a)-(c) Calculated spectra of the experimental system as function of detuning proportion, comparing the effects of different mechanisms for spin coupling: (a) spectrum without any spin coupling effects; (b) spectrum including spin-orbit coupling effects calculated for this system as described in subsection 5.6.2; (c) Sample spectrum with both spin-orbit and hyperfine induced Overhauser field gradients, using a single combination of h_{Nd} fields selected from a normal distribution with standard deviation $\delta_N = 73$ neV. (d) Fits to the experimental data from Fig. 3b, using the time evolution simulations described in subsection 5.6.2, for different values of distance between neighboring dots.

Time evolution simulations Using the full Hamiltonian with spin-coupling, we perform time evolution calculations to simulate the conditions in the p_ϵ pulsing experiments. In the experiment, we initialize the ground state at point M and ramp adiabatically to $p_\epsilon = 0.8$, before pulsing to point N with a variable ramp time τ_{ramp} .

We use an in-house solver package [34] to simulate the evolution of the initialized state for the last 20% of p_ϵ with varying ramp times. At $p_\epsilon = 0.8$, we consider the ini-

tialized state as a statistical mixture of the two lowest energy eigenstates, both of which are $s = 1/2$ states at $p_e = 0.8$. We consider 20 values of τ_{ramp} in the range from 50 ns to 1 μ s, taking 10000 time-steps for each ramp. We then add the overlaps of the averaged density matrix with each of the four lowest energy eigenstates at point N (i.e., the eigenstates with $s = 3/2$). This overlap can be mapped to an ideal P_T measurement with the method described two sections below. For each value of τ_{ramp} , we repeat the evolution 350 times, drawing different values of h_{Na} , and compute the average P_T for the final state. To account for imperfections of the experimental measurement of P_T —caused by the finite measurement bandwidth, the signal to noise ratio and $|T\rangle$ to $|S\rangle$ relaxation, as well as unwanted leakage to other states during the pulsed passages—we scale the ideal calculated values of $P_T(\tau_{ramp})$ to match the experimental P_T at the minimum and maximum value of τ_{ramp} .

We vary the parameter δ_N and use the method above to get the best fit to our experimental data. Additionally, the spin-orbit term requires an estimate of the distance between neighboring dots, which was lithographically designed to be $\ell = 150$ nm. We consider a conservative range of ℓ from 100 to 200 nm (see Fig. 5.9(d)), from which we extract the estimate for $\delta_N = 73 \pm 3$ neV quoted in the main text.

Extracting δ_N using the Landau-Zener model. The nuclear fields lead to the lifting of the spin degeneracies of the $s = 3/2$ quadruplet and the $s = 1/2$ doublets and multiple avoided crossings of the order of δ_N . A simple estimate of the characteristic time-scale of crossover between the diabatic and the adiabatic regimes of voltage tuning can be obtained by using the Landau-Zener formula for a two-level system [35]. Then the characteristic ramp time is

$$\tau_{ramp}^* = \frac{\hbar \Delta p_e}{2\pi \delta_N^2} \frac{d\Delta E}{dp_e}. \quad (5.21)$$

For $\Delta p_e = 0.2$ this gives $\tau_{ramp}^* \sim 100$ ns, which is consistent with the time scale obtained by the time-dependent numerical simulation of the model.

External magnetic field. To capture the orbitals effects resulting from a magnetic flux through the square plaquette, we modify the tunneling term in Eq. (5.13) as:

$$- \sum_{\langle j,k \rangle \sigma} t_{jk} e^{-i\varphi_{jk}} c_{j\sigma}^\dagger c_{k\sigma},$$

with the Peierls phase:

$$\varphi_{jk} = \frac{e}{\hbar} \int_{\mathbf{r}_k}^{\mathbf{r}_j} d\mathbf{r} \cdot \mathbf{A}(\mathbf{r}) = \frac{2\pi}{\Phi_0} \int_{\mathbf{r}_k}^{\mathbf{r}_j} d\mathbf{r} \cdot \mathbf{A}(\mathbf{r}), \quad (5.22)$$

where $e > 0$ is the elementary charge, \hbar is the reduced Planck constant, $\Phi_0 = h/e$ is the flux quantum, and $\mathbf{A}(\mathbf{r})$ is the magnetic vector potential. We use the gauge for which $\varphi_{41} = 2\pi\Phi/\Phi_0$, with $\Phi = B\ell^2$ the magnetic flux through the plaquette and ℓ the length of the side of the plaquette, and the phases for the other links vanish.

The Zeeman contribution is:

$$\mathcal{H}_Z = g\mu_B \mathbf{B} \cdot \mathbf{S}, \quad (5.23)$$

where \mathbf{B} is the external magnetic field.

Charge stability simulations. In this work we use charge stability diagrams to identify different charge occupation regimes and charge transitions as function of gate voltages. To accurately simulate the charge stability diagrams, we modify our model to expand the number of basis states such that the system is no longer constrained to a total of 3 electrons, while each dot can still be occupied by 0 to 2 electrons, and we include the effect of intersite Coulomb repulsion, by adding a $\sum_{i<j} V_{i,j} n_i n_j$ term to Eq. (5.13). Additionally, we use gate to local energy lever arms and a cross-capacitance matrix measured from experiment to implement gate voltages P_i into the model and calculate their effect on local energies μ_i . We use this model to calculate charge occupation as a function of gate voltages. We used the simulation toolbox in the Python based package *qtt* [38] to run these simulations.

5.6.3. MAPPING 3-SPIN STATES ONTO 2-SPIN MEASUREMENTS

In the main text, we state that we can distinguish between the 3-spin $s = 1/2$ and $s = 3/2$ states through a projective singlet/triplet ($|S\rangle/|T\rangle$) measurement on 2 random spins. Here we show this in the first-quantization formulation of the spin states. We use the following 8 basis states of the system with 3 spin- $\frac{1}{2}$ particles:

$$\begin{aligned}
 \left|\frac{3}{2}, +\frac{3}{2}\right\rangle &= |\uparrow\uparrow\uparrow\rangle \\
 \left|\frac{3}{2}, +\frac{1}{2}\right\rangle &= \frac{1}{\sqrt{3}} (|\uparrow\uparrow\downarrow\rangle + |\uparrow\downarrow\uparrow\rangle + |\downarrow\uparrow\uparrow\rangle) \\
 \left|\frac{3}{2}, -\frac{1}{2}\right\rangle &= \frac{1}{\sqrt{3}} (|\downarrow\downarrow\uparrow\rangle + |\downarrow\uparrow\downarrow\rangle + |\uparrow\downarrow\downarrow\rangle) \\
 \left|\frac{3}{2}, -\frac{3}{2}\right\rangle &= |\downarrow\downarrow\downarrow\rangle \\
 \left|\frac{1}{2}, +\frac{1}{2}\right\rangle_1 &= \frac{1}{\sqrt{3}} \left(-|\uparrow\uparrow\downarrow\rangle + e^{i\pi/3} |\uparrow\downarrow\uparrow\rangle + e^{-i\pi/3} |\downarrow\uparrow\uparrow\rangle \right) \\
 \left|\frac{1}{2}, -\frac{1}{2}\right\rangle_1 &= \frac{1}{\sqrt{3}} \left(-|\downarrow\downarrow\uparrow\rangle + e^{i\pi/3} |\downarrow\uparrow\downarrow\rangle + e^{-i\pi/3} |\uparrow\downarrow\downarrow\rangle \right) \\
 \left|\frac{1}{2}, +\frac{1}{2}\right\rangle_2 &= \frac{1}{\sqrt{3}} \left(-|\uparrow\uparrow\downarrow\rangle + e^{-i\pi/3} |\uparrow\downarrow\uparrow\rangle + e^{i\pi/3} |\downarrow\uparrow\uparrow\rangle \right) \\
 \left|\frac{1}{2}, -\frac{1}{2}\right\rangle_2 &= \frac{1}{\sqrt{3}} \left(-|\downarrow\downarrow\uparrow\rangle + e^{-i\pi/3} |\downarrow\uparrow\downarrow\rangle + e^{i\pi/3} |\uparrow\downarrow\downarrow\rangle \right)
 \end{aligned} \tag{5.24}$$

The 2-spin system has one singlet ($|S\rangle$) and three triplet states ($|T_+\rangle, |T_0\rangle, |T_-\rangle$), given by:

$$\begin{aligned}
 |S\rangle &= |0, 0\rangle = \frac{1}{\sqrt{2}} (|\uparrow\downarrow\rangle - |\downarrow\uparrow\rangle) \\
 |T_+\rangle &= |1, +1\rangle = |\uparrow\uparrow\rangle \\
 |T_0\rangle &= |1, 0\rangle = \frac{1}{\sqrt{2}} (|\uparrow\downarrow\rangle + |\downarrow\uparrow\rangle) \\
 |T_-\rangle &= |1, -1\rangle = |\downarrow\downarrow\rangle
 \end{aligned} \tag{5.25}$$

To obtain the 2-spin projection on the 3-spin system, we take partial inner products of each of the eight basis states with singlet and triplet states in the first two spins. First, we

take the basis state $|\frac{3}{2}, +\frac{3}{2}\rangle$:

$$\begin{aligned}
 \langle S|\frac{3}{2}, +\frac{3}{2}\rangle &= \frac{1}{\sqrt{2}} [\langle \uparrow\downarrow| - \langle \downarrow\uparrow|] |\uparrow\uparrow\uparrow\rangle = 0 \\
 \langle T_0|\frac{3}{2}, +\frac{3}{2}\rangle &= \frac{1}{\sqrt{2}} [\langle \uparrow\downarrow| + \langle \downarrow\uparrow|] |\uparrow\uparrow\uparrow\rangle = 0 \\
 \langle T_+|\frac{3}{2}, +\frac{3}{2}\rangle &= \langle \uparrow\uparrow\uparrow\uparrow\rangle = |\uparrow\rangle \\
 \langle T_-|\frac{3}{2}, +\frac{3}{2}\rangle &= \langle \downarrow\downarrow\uparrow\uparrow\rangle = 0
 \end{aligned} \tag{5.26}$$

The probability of a $|S\rangle$ measurement outcome in a 2-spin projective measurement of the $|\frac{3}{2}, +\frac{3}{2}\rangle$ basis state is $\|\langle S|\frac{3}{2}, +\frac{3}{2}\rangle\|^2 = 0$. Similarly, the probability of a $|T\rangle$ measurement outcome is

$$\|\langle T_+|\frac{3}{2}, +\frac{3}{2}\rangle\|^2 + \|\langle T_0|\frac{3}{2}, +\frac{3}{2}\rangle\|^2 + \|\langle T_-|\frac{3}{2}, +\frac{3}{2}\rangle\|^2 = 1 + 0 + 0 = 1.$$

Following similar derivations, we find that also for the other three basis states with $s = 3/2$, the probabilities of obtaining $|S\rangle$ and $|T\rangle$ upon measurement are 0 and 1 respectively.

Next, we take the basis state $|\frac{1}{2}, +\frac{1}{2}\rangle_1$:

$$\begin{aligned}
 \langle S|\frac{1}{2}, +\frac{1}{2}\rangle_1 &= \frac{1}{\sqrt{2}} [\langle \uparrow\downarrow| - \langle \downarrow\uparrow|] \frac{1}{\sqrt{3}} [-|\uparrow\uparrow\downarrow\rangle + e^{i\pi/3}|\uparrow\downarrow\uparrow\rangle + e^{-i\pi/3}|\downarrow\uparrow\uparrow\rangle] \\
 &= \frac{1}{\sqrt{6}} [e^{i\pi/3} - e^{-i\pi/3}] |\uparrow\rangle = \frac{i}{\sqrt{2}} |\uparrow\rangle \\
 \langle T_0|\frac{1}{2}, +\frac{1}{2}\rangle_1 &= \frac{1}{\sqrt{2}} [\langle \uparrow\downarrow| + \langle \downarrow\uparrow|] \frac{1}{\sqrt{3}} [-|\uparrow\uparrow\downarrow\rangle + e^{i\pi/3}|\uparrow\downarrow\uparrow\rangle + e^{-i\pi/3}|\downarrow\uparrow\uparrow\rangle] \\
 &= \frac{1}{\sqrt{6}} [e^{i\pi/3} + e^{-i\pi/3}] |\uparrow\rangle = \frac{1}{\sqrt{6}} |\uparrow\rangle \\
 \langle T_+|\frac{1}{2}, +\frac{1}{2}\rangle_1 &= \langle \uparrow\uparrow| \frac{1}{\sqrt{3}} [-|\uparrow\uparrow\downarrow\rangle + e^{i\pi/3}|\uparrow\downarrow\uparrow\rangle + e^{-i\pi/3}|\downarrow\uparrow\uparrow\rangle] = -\frac{1}{\sqrt{3}} |\downarrow\rangle \\
 \langle T_-|\frac{1}{2}, +\frac{1}{2}\rangle_1 &= \langle \downarrow\downarrow| \frac{1}{\sqrt{3}} [-|\uparrow\uparrow\downarrow\rangle + e^{i\pi/3}|\uparrow\downarrow\uparrow\rangle + e^{-i\pi/3}|\downarrow\uparrow\uparrow\rangle] = 0
 \end{aligned} \tag{5.27}$$

This results in 2-spin measurement probabilities of:

$$\begin{aligned}
 \|\langle S|\frac{1}{2}, +\frac{1}{2}\rangle_1\|^2 &= \frac{1}{2} \quad \text{and} \\
 \|\langle T_+|\frac{1}{2}, +\frac{1}{2}\rangle_1\|^2 + \|\langle T_0|\frac{1}{2}, +\frac{1}{2}\rangle_1\|^2 + \|\langle T_-|\frac{1}{2}, +\frac{1}{2}\rangle_1\|^2 &= \frac{1}{3} + \frac{1}{6} + 0 = \frac{1}{2}.
 \end{aligned}$$

Similar calculations for the other three basis states with $s = 1/2$ show $|S\rangle$ and $|T\rangle$ measurement probabilities of 0.5 each. Although we have used the 2 spin singlet and triplet states for the first two spins for the calculations, same results hold for any other two spin combinations.

Assuming statistical mixing of the 8 basis states with 3 spin-1/2 particles, the probability of a two-spin singlet measurement outcome is given by:

$$P_S = \sum_{s,m} P(s, m) |\langle S | s, m \rangle|^2 \quad (5.28)$$

where $P(s, m)$ is the probability of occupation of the three-electron spin state $|s, m\rangle$. Similarly the probability of a two-spin triplet measurement outcome is given by:

$$P_T = \sum_{s,m} P(s, m) [|\langle T_+ | s, m \rangle|^2 + |\langle T_0 | s, m \rangle|^2 + |\langle T_- | s, m \rangle|^2] \quad (5.29)$$

As we have seen before, for any basis state with $s = 3/2$, the probability two-spin triplet measurement outcome is 1. So, for any statistical mixture of $s = 3/2$ basis states, the probability a two-spin triplet measurement outcome is also 1. Similarly, for any statistical mixture of $s = 1/2$ basis states, the probability a two-spin triplet measurement outcome is 0.5. So in our experiment the expected values of $P_T^{3/2}$ and $P_T^{1/2}$ are 1 and 0.5, where $P_T^{3/2}$ ($P_T^{1/2}$) is the probability a two-electron triplet state measurement outcome from the quadruplet (doublet) configuration.

BIBLIOGRAPHY

- [1] J. P. Dehollain, U. Mukhopadhyay, V. P. Michal, Y. Wang, B. Wunsch, C. Reichl, W. Wegscheider, M. S. Rudner, E. Demler, and L. M. K. Vandersypen, arXiv e-prints , arXiv:1904.05680 (2019), arXiv:1904.05680 [cond-mat.mes-hall] .
- [2] A. Auerbach, *Interacting Electrons and Quantum Magnetism* (Springer New York, 1994).
- [3] D. C. Mattis, *The Theory of Magnetism Made Simple* (World Scientific, 2006).
- [4] E. C. Stoner, Proceedings of the Royal Society of London. Series A. Mathematical and Physical Sciences **165**, 372 (1938).
- [5] P. Fazekas, *Lecture notes on electron correlation and magnetism* (World Scientific, 1999).
- [6] G.-B. Jo, Y.-R. Lee, J.-H. Choi, C. A. Christensen, T. H. Kim, J. H. Thywissen, D. E. Pritchard, and W. Ketterle, Science **325**, 1521 (2009).
- [7] D. Pekker, M. Babadi, R. Sensarma, N. Zinner, L. Pollet, M. W. Zwierlein, and E. Demler, Physical review letters **106**, 050402 (2011).
- [8] H. Tasaki, Progress of Theoretical Physics **99**, 489 (1998).
- [9] Y. Nagaoka, Physical Review **147**, 392 (1966).
- [10] J. Hubbard, Proceedings of the Royal Society of London. Series A. Mathematical and Physical Sciences **276**, 238 (1963).
- [11] D. C. Mattis, International Journal of Nanoscience **02**, 165 (2003).

- [12] E. Nielsen and R. N. Bhatt, *Physical Review B* **76**, 161202(R) (2007).
- [13] A. Oguri, Y. Nisikawa, Y. Tanaka, and T. Numata, *Journal of Magnetism and Magnetic Materials* **310**, 1139 (2007).
- [14] J. von Stecher, E. Demler, M. D. Lukin, and A. M. Rey, *New Journal of Physics* **12**, 055009 (2010).
- [15] I. Bloch, J. Dalibard, and S. Nascimbène, *Nature Physics* **8**, 267 (2012).
- [16] L. P. Kouwenhoven, D. G. Austing, and S. Tarucha, *Reports on Progress in Physics* **64**, 701 (2001).
- [17] W. G. van der Wiel, S. D. Franceschi, J. M. Elzerman, T. Fujisawa, S. Tarucha, and L. P. Kouwenhoven, *Rev. Mod. Phys.* **75**, 1 (2002).
- [18] R. Hanson, L. Kouwenhoven, J. Petta, S. Tarucha, and L. Vandersypen, *Rev. Mod. Phys.* **79**, 1217 (2007).
- [19] P. Barthelemy and L. M. K. Vandersypen, *Annalen der Physik* **525**, 808 (2013).
- [20] T. Hensgens, T. Fujita, L. Janssen, X. Li, C. J. V. Diepen, C. Reichl, W. Wegscheider, S. D. Sarma, and L. M. K. Vandersypen, *Nature* **548**, 70 (2017), 1702.07511v1 .
- [21] R. Thalineau, S. Hermelin, A. D. Wieck, C. Bäuerle, L. Saminadayar, and T. Meunier, *Appl. Phys. Lett.* **101**, 103102 (2012).
- [22] M. Seo, H. K. Choi, S.-Y. Lee, N. Kim, Y. Chung, H.-S. Sim, V. Umansky, and D. Mahalu, *Phys. Rev. Lett.* **110** (2013), 10.1103/physrevlett.110.046803.
- [23] A. Noiri, K. Kawasaki, T. Otsuka, T. Nakajima, J. Yoneda, S. Amaha, M. R. Delbecq, K. Takeda, G. Allison, A. Ludwig, A. D. Wieck, and S. Tarucha, *Semicond. Sci. Technol.* **32**, 084004 (2017).
- [24] U. Mukhopadhyay, J. P. Dehollain, C. Reichl, W. Wegscheider, and L. M. K. Vandersypen, *Appl. Phys. Lett.* **112**, 183505 (2018).
- [25] P.-A. Mortemousque, E. Chanrion, B. Jadot, H. Flentje, A. Ludwig, A. D. Wieck, M. Urdampilleta, C. Bäuerle, and T. Meunier, *arXiv e-prints*, arXiv:1808.06180 (2018), arXiv:1808.06180 [cond-mat.mes-hall] .
- [26] E. Lieb and D. Mattis, *Phys. Rev.* **125**, 164 (1962).
- [27] A. V. Khaetskii, D. Loss, and L. Glazman, *Phys. Rev. Lett.* **88**, 186802 (2002).
- [28] I. A. Merkulov, A. L. Efros, and M. Rosen, *Phys. Rev. B* **65**, 205309 (2002).
- [29] E. A. Chekhovich, M. N. Makhonin, A. I. Tartakovskii, A. Yacoby, H. Bluhm, K. C. Nowack, and L. M. K. Vandersypen, *Nature Materials* **12**, 494 (2013).
- [30] J. R. Petta, *Science* **309**, 2180 (2005).

- [31] F. H. L. Koppens, *Science* **309**, 1346 (2005).
- [32] D. C. Mattis, *The theory of magnetism I: statics and dynamics*, Springer series in solid-state sciences (Springer, 1981).
- [33] Y. Aharonov and D. Bohm, *Phys. Rev.* **115**, 485 (1959).
- [34] https://github.com/stephanlphilips/dm_solver.
- [35] L. D. L. Landau and E. M. Lifshitz, *Quantum Mechanics* (Elsevier Science, 2013).
- [36] D. Stepanenko, M. Rudner, B. I. Halperin, and D. Loss, *Phys. Rev. B* **85**, 075416 (2012).
- [37] R. Winkler, *Spin-orbit coupling effects in two-dimensional electron and hole systems* (Springer Berlin Heidelberg, 2003).
- [38] <https://github.com/QuTech-Delft/qtt>.

6

A CAPACITANCE SPECTROSCOPY-BASED PLATFORM FOR REALIZING GATE-DEFINED ELECTRONIC LATTICES

Electrostatic confinement in semiconductors provides a flexible platform for the emulation of interacting electrons in a two-dimensional lattice, including in the presence of gauge fields. This combination offers the potential to realize a wide host of quantum phases. Capacitance spectroscopy provides a technique that allows one to directly probe the density of states of such two-dimensional electron systems. Here, we present a measurement and fabrication scheme that builds on capacitance spectroscopy and allows for the independent control of density and periodic potential strength imposed on a two-dimensional electron gas. We characterize disorder levels and (in)homogeneity and develop and optimize different gating strategies at length scales where interactions are expected to be strong. A continuation of these ideas might see to fruition the emulation of interaction-driven Mott transitions or Hofstadter butterfly physics.

6.1. INTRODUCTION

Artificial lattice structures have the potential for realizing a host of distinct quantum phases[2]. Of these, the inherent length scale of optical platforms allows for a clean emulation of quantum mechanical band physics, but also means interactions are rather weak [3, 4]. For electronic implementations in solid-state, interactions can be made non-perturbatively strong, potentially leading to a host of emergent phenomena. An example is shown in graphene superlattices, where not only Hofstadter’s butterfly physics [5–8] but also interaction-driven and emergent fractional quantum Hall states in the butterfly appear [9]. The ideal platform would host a designer lattice with tunable electron density and lattice strength, allowing to emulate band physics for a wide variety of lattice types and giving access to the strong-interaction limit of correlated Mott phases [10–14]. Semiconductor heterostructures with nano-fabricated gate structures provide this flexibility in lattice design and operation, yet inherent disorder in the host materials, as well as the short length scales required, make the realization of clean lattices difficult [15–17].

In this letter, we introduce a novel experimental platform for realizing artificial gate-induced lattices in semiconductors, based on a capacitance spectroscopy technique [18–20], with the potential to observe both single-particle band structure physics such as Hofstadter’s butterfly and many-body physics such as the interaction driven Mott insulator transition. We discuss different gating strategies for imprinting a two-dimensional periodic potential at length scales where interactions are expected to be strong, characterize intrinsic disorder levels, and show first measurements of double gate devices.

6

6.2. HETEROSTRUCTURE AND CAPACITANCE SPECTROSCOPY

To host the 2D electron gas (2DEG), we use a GaAs quantum well with AlGaAs barriers, grown by molecular beam epitaxy. The substrate contains a highly Si-doped GaAs layer that acts as a back gate. It is tunnel coupled to the 2DEG through a $\text{Al}_x\text{Ga}_{1-x}\text{As}$ tunnel barrier (see Fig. 6.1(a) and Table 6.1). There is no doping layer above the quantum well in order to avoid an important source of disorder. A metallic top gate is fabricated on the surface. A variable capacitor forms between the back and top gates: when an alternating potential difference is applied between them, electrons tunnel back and forth between the back gate and the 2DEG, modifying the capacitance by an amount proportional to the density of states (DOS) of the 2DEG. The tunnel frequency depends mainly on the thickness and the Al content (x) of the tunnel barrier. At the limits of zero or infinite DOS, the system behaves like a simple parallel plate capacitor, described by the distance between the top gate and the back gate or the top gate and the 2DEG, respectively. The capacitance is read out using a bridge design with a reference capacitor [21], where the voltage at the bridge point is kept constant (Fig. 6.1(b)) by changing the amplitude ratio and phase difference of AC signals applied to each capacitor (see subsection 6.7.1 for experimental details).

To impose a periodic potential in the 2DEG, we pattern a metallic gate into a grid shape before making the top gate. From a capacitance spectroscopy perspective, this double-gate structure can be made with two different designs. In the first design, the top gate is separated from the grid gate by a thick dielectric layer, rendering its capacitance to the grid gate negligible (a few pF compared to tens of pF)(Fig. 6.1(c)). Alternatively,

we can minimize the separation between the two gate layers, such that the capacitance between the two top gates (100s of pF) exceeds the sample capacitance. Here the two gates effectively form a single gate (Fig. 6.1(d)), as seen in AC. We investigate both designs below, starting with describing the fabrication (limits) and following with measurements of disorder levels and imposed potentials.

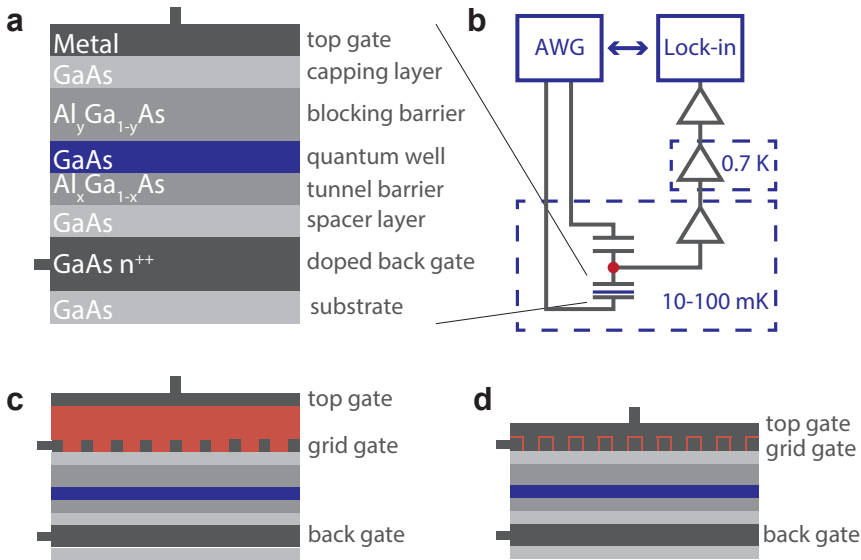


Figure 6.1: (a) Schematic diagram showing the various layers of the samples with a single global gate. (b) Bridge set-up for equilibrium capacitance measurements, where sinusoidal signals are applied by a waveform generator (WG) on both the sample back gate and on a reference capacitor of 45 pF. The relative amplitude and phase difference between these two signals are adjusted to maintain a constant zero voltage at the bridge point (red dot), which is amplified in different stages and read out using a lock-in amplifier. The bridge point is connected to the grid gate when there is a grid gate present, and to the top gate otherwise. (c)-(d) Schematic diagrams of two different two-layer gate geometries, designed to impose a periodic potential on the 2DEG, comprising either of a deposited dielectric (c) or a dielectric obtained by oxidation of the first metallic layer (d). The dielectric spacer is depicted in red. The other colors are as in panel (a).

6.3. GATE DESIGN AND FABRICATION

We distinguish devices with a single global gate (Fig. 6.1(a)) and devices with two layers of gates: a grid gate and a uniform global gate on top (Fig. 6.1(c-d)). The former will be used to characterize disorder levels in section 6.4, whereas the latter allows for the imposition of a periodic potential. The strength of the imparted periodic potential depends on the dielectric choice (thick or thin, compare Fig. 6.1(c-d)), gate design, grid gate pitch, and the maximum voltages that can be applied. Grid gates are made with a pitch of 100 - 200 nm (Fig. 6.2(a-b)), which is mainly limited by the fabrication constraints. The maximum voltage is determined by the onset of leakage through the heterostructure or the accumulation of charges in the capping layer and thus depends on heterostructure details such as the Al concentration and layer thicknesses.

The expected imparted potentials at the 2DEG with typical maximum voltages for both designs are shown in Fig. 6.2(c-f) (calculated using COMSOL electrostatic simulation software). In order to observe a Mott transition and the corresponding localization of electrons on individual sites, the periodic potential amplitude must exceed the local Coulomb repulsion (typically several meVs) [22]. For 200 nm grids, both designs show similar maximum effective periodic potentials, and they should suffice for the formation of quantum dots. For the 100 nm grids, however, the achievable potentials exceed the charging energy only when using the overlapping gate design. For the smaller pitch grid, effective shielding of the top gate voltage by the grid gate is larger when the top gate is farther away from the heterostructure. Therefore, an overlapping gate design is required to go to sufficiently strong periodic potentials for localization at 100 nm site-to-site pitch.

Furthermore, we note that screening induced by mobile charges in the back gate region has both desired and undesirable consequences. An intended benefit is that disorder from charged impurities or defects in the heterostructure is partly screened, and the more so the closer to the back gate the impurities or defects are located [14]. However, electron-electron interactions and the gate-voltage imposed potential modulation itself are partly screened as well, and more so as the lattice dimension is reduced.

6

Double gate devices with either a thick (Fig. 6.1(c)) or a thin dielectric (Fig. 6.1(d)) between the two gates require different fabrication processes. Here, we discuss the fabrication of the active regions in both designs, which have a size of $200\ \mu\text{m}$ by $200\ \mu\text{m}$. The detailed information for all steps in the fabrication is provided in subsection 6.7.2. In both designs, the square grid metallic gates are fabricated at pitches of 100-200 nm using electron beam lithography and evaporation of metals in a standard lift-off process (Fig. 6.2(a-b)). In the first design, both gates are made of Ti/Au(Pd) and separated by $> 200\ \text{nm}$ layer of oxide, such as plasma-enhanced chemical vapor deposition grown SiO_x or plasma-enhanced atomic layer deposition grown AlO_x . In the second design, both gates are made of Al, and an oxygen (remote) plasma oxidation step is used after depositing the first Al layer to ensure sufficient electrical isolation between the two layers by transforming part of the Al gate to Aluminum oxide [23]. In this design, we measure resistances exceeding $1\ \text{G}\Omega$ over several volts.

Because of the fabrication process, there are limits in the periodicity and homogeneity of the grid gate layer. We typically find (1) that plaquettes of a smaller size than $40\ \text{nm} \times 40\ \text{nm}$ will not lift off and that (2) the grain size of a particular metal determines the narrowest lines that can be made reliably with liftoff. For the materials used here, AuPd and Al, these effects limit the minimum lattice pitch (Fig. 6.3(a)). Furthermore, we have analyzed the homogeneity of the lattices by using image processing techniques to give the statistics of the non-metal plaquette areas (Fig. 6.3(b)). A more relaxed lattice constant means higher relative homogeneity but this is not necessarily helpful: it also increases the flux through a single plaquette when a perpendicular magnetic field is applied (relevant for Hofstadter butterfly physics, as will be described below) and it decreases the charging energy, relevant for Mott interaction physics.

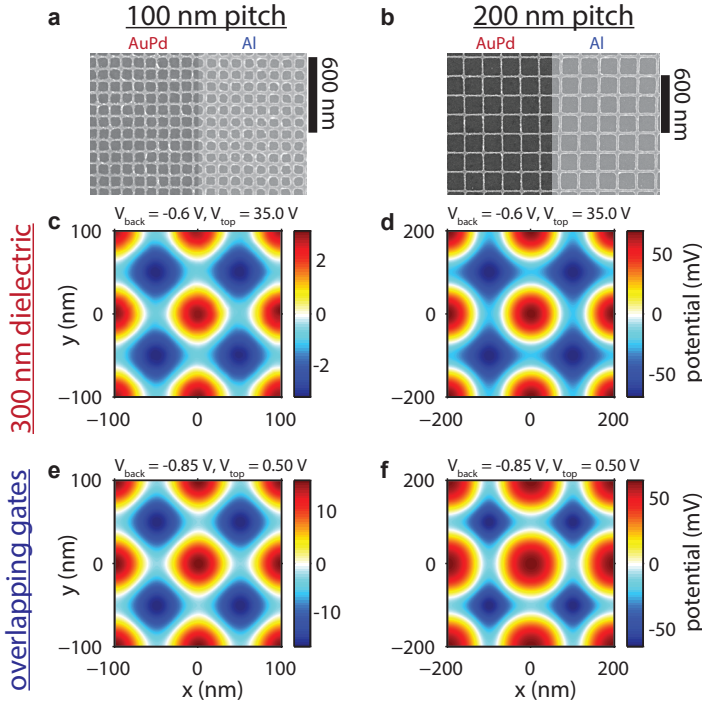


Figure 6.2: (a) Electron micrograph of 100 nm periodic AuPd and Al grid gate structures for two different gate designs. (b) Similarly, for 200 nm periodic gate structures. (c)-(f) Electrostatic simulations of imparted potential in the 2DEG in both designs and both gate pitches (100 and 200 nm) using denoted gate voltages. For (c)-(d), we use a 350 nm SiO₂ dielectric and flat top gate. For (e)-(f), we use a 5 nm spacer dielectric (oxidized Aluminum oxide) separating the two top gates. Voltages used are roughly the empirical maximum voltage difference we can set for both designs (see fig 6.5), $V_{\text{grid}} = -0.45$ V for both. Widths of the metal grids are taken as 22 nm and 25 nm for AuPd and Al grids respectively, for reasons explained below.

6.4. MEASUREMENTS

6.4.1. GLOBAL GATES: DISORDER LEVELS

In order to assess disorder levels, we first measure the devices with a single uniform top gate. We measure the capacitance at frequencies below and above the rate at which electrons tunnel between the 2DEG and the doped back gate region as a function of bias voltage (Fig. 6.4(a-b)) and magnetic field. Having measured the capacitance at low and high frequencies, we calculate the equilibrium DOS. There are essentially two unknown parameters in this conversion, namely the distance from top to bottom gate and the relative location of the 2DEG itself. The former can be directly inferred from the capacitance at high frequency, the latter by using either the known effective mass or the Landau level splitting with magnetic field as benchmarks (see subsection 6.7.3 for details on this conversion).

As a magnetic field is turned on, we see the onset of Landau level formation. For

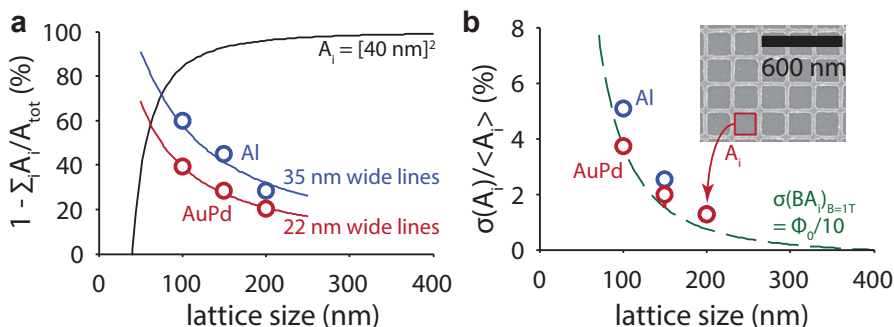


Figure 6.3: (a) The fraction of surface area covered by the grid gate as a function of lattice size. The black line indicates a grid with the smallest possible plaquettes allowed by the lift-off process, whereas the blue (red) line indicates the percentage of surface area covered by a grid with metallic lines of 35 nm (22 nm). (b) Variation in relative area of non-metal plaquettes in the grid gate layer (A_i , see inset) as a function of lattice size, as a measure of fabrication (in)homogeneity. The green dashed line indicates variations in plaquette area that coincide with variations of a tenth of a flux quantum at 1 T (see Discussion below). Blue (red) points indicate grid gates made of Al (AuPd) for both figures.

6

magnetic fields above 2 T, we observe a splitting between the spin subbands of the Landau levels which increases with the applied magnetic field (Fig. 6.4(c)). For a given magnetic field, the separation between the two subbands of any Landau level is significantly larger than the Zeeman energy with $g = -0.44$ for bulk electrons in GaAs [18]. This enhanced Zeeman splitting is an effect of the Coulomb repulsion between electrons in the same subband [24].

We focus on the low-field data (Fig. 6.4(d)) and infer disorder levels from the density of states data (Fig. 6.4(e)). Gaussian fits to the Landau levels yield typical widths ranging between 0.4-1 meV at densities above 10^{11} cm^{-2} , which, although hard to compare directly to the mobilities reported for transport-based wafers [15–17], is comparable to previously reported values for similar heterostructures [25]. The Landau levels themselves (aliased at low fields in Fig. 6.4(d)) become visible above fields of roughly 0.25 T, corresponding to densities per Landau level of $1.2 \times 10^{10} \text{ cm}^{-2}$ and cyclotron gaps of 0.43 meV. The Landau level width did not change when we increased the mixing chamber temperature from 10 mK to 100 mK or when we varied the excitation voltage. Furthermore, the Landau level width was consistent across fabrication schemes but did vary with the wafer used. Therefore, we consider it a heuristic metric for the achievable disorder levels on a particular wafer.

We have tried to optimize wafer design to minimize this disorder, while allowing for the imposition of a periodic potential. All in all, over twenty different GaAs/ $\text{Al}_x\text{Ga}_{1-x}\text{As}$ wafers grown by molecular beam epitaxy have been used. Growth details of the wafers can be found in Table 6.1.

The initial wafer (W1) design was based on Dial et. al. [26], and was grown on a conducting substrate. This simplifies the fabrication of single-gate devices, as an unpatterned ohmic back gate contact can be directly evaporated on the back side of the wafer,

while simple metallic pads fabricated on the front side can be directly bonded to and used as a top gate. A double-gate design requires dedicated bond pads, which would give a sizable contribution to the total capacitance when fabricated directly on the wafer. The device used for Fig. 6.5(a-b) in the main text, fabricated on one of the first rounds of wafers (W2), therefore, had bond pads on top of the thick dielectric separating the two gates. This strategy is not compatible with the second design, where there is no thick dielectric layer, and also gives a very low wire bonding yield due to poor adhesion of the dielectric layers on the GaAs surface. Furthermore, handling both sides of a substrate during fabrication risks contaminating the front surface, and is particularly suboptimal when detailed features (grid gates) are present as well. Subsequent wafers were, therefore, grown with a 400-800 nm thin degenerately Si-doped back gate region that is contacted from the front side of the wafer, and is etched to form electrically isolated device and bond pad mesas.

We have further tried to optimize the wafer stacks aiming to increase the amplitude of the periodic potential at the 2DEG and to decrease disorder levels. A stronger periodic potential can be obtained by either increasing the maximum possible gate voltage, reducing the separation between the grid gate and the 2DEG or increasing the distance between the 2DEG and the back gate. The latter may also reduce disorder caused by dopant diffusion from the back gate. Increasing the quantum well thickness is also expected to reduce the effect of disorder by accommodating more of the electron wavefunction away from the interfaces. Concretely, we have first varied spacer layer thickness (25 and 35 nm) and quantum well widths (15 and 30 nm). In further attempts to optimize the trade-off between the periodic potential that can be set at a fixed voltage and the maximum voltage we can apply to the gates before leakage sets in, we varied the blocking barrier thickness (40, 50, 60, and 70 nm) and fabricated devices with a thin dielectric layer (see wafers M1 and W3) added underneath the grid gate. None of these, however, managed to noticeably increase the maximum potential we could impose on the 2DEG, or to decrease disorder levels. The strongest effect on disorder was obtained by changing the aluminum concentration in the $\text{Al}_x\text{Ga}_{1-x}\text{As}$ blocking and tunnel barrier (from $x = 0.31$ everywhere to $x = 0.36$ in the blocking barrier and $x = 0.20$ in the tunnel barrier), while slightly increasing the tunnel barrier thickness in order to keep the tunnel rates roughly the same (see Table 6.1). The measurements shown in Fig. 6.4 and Fig.s. 6.5(c-d) are taken on this optimized wafer, called M2.

6.4.2. GRID GATES: PERIODIC POTENTIAL STRENGTH

For measurements of two-layer gate devices of both designs (Fig. 6.5), we keep the grid gate potential fixed, given that it serves as the gate voltage of the first transistor in the amplification chain, and map out the remaining two gate voltages over as large a range as possible. Initial devices of both designs indeed show accumulation as a function of the two gate voltages (transition from light gray to blue in Fig. 6.5(a,c). At voltages where we expect a flat periodic potential (close to the center of each panel in Fig. 6.5), and for our final set of devices, we can still distinguish well-defined Landau levels, indicating that the added fabrication steps themselves do not severely increase the disorder levels (data not shown). This disorder in the potential landscape also leads to a broadening of the onset of accumulation, seen in the center of Fig. 6.5(a,c).

Table 6.1: Heterostructure details.

	W1	W2	M1	W3	M2
capping layer	GaAs	GaAs	GaAs	GaAs	GaAs
	10 nm	10 nm	5 nm	10 nm	5 nm
blocking barrier (Al content)	0.316	0.316	0.316	0.315	0.360
	60 nm	60 nm	40 nm	60 nm	60 nm
quantum well	GaAs	GaAs	GaAs	GaAs	GaAs
	23 nm	23 nm	23 nm	23 nm	23 nm
tunnel barrier (Al content)	0.316	0.316	0.316	0.315	0.199
	13 nm	13 nm	14 nm	14 nm	16 nm
spacer layer	GaAs	GaAs	GaAs	GaAs	GaAs
	25 nm	15 nm	15 nm	15 nm	15 nm
back gate	GaAs n ⁺⁺	GaAs n ⁺⁺	GaAs n ⁺⁺	GaAs n ⁺⁺	GaAs n ⁺⁺
	800 nm	800 nm	400 nm	400 nm	400 nm
tunneling frequency at 0T, $n \approx 10^{11} \text{ cm}^{-2}$	1 MHz	200 kHz	2 kHz	30 kHz	100 kHz
lowest field at which Landau levels can be distinguished	3 T (at 4 K)	0.65 T	0.50 T	0.40 T	0.25 T
comments	n ⁺⁺ doped	n ⁺⁺ doped			
	substrate	substrate			

For devices of the first design, this broadening increases as we move away from the center, along the gray-blue boundary (Fig. 6.5(a)). This suggests that we see a gate-voltage induced spatial variation in the 2DEG potential that exceeds disorder levels (0.4–1 meV) at low densities. Based on electrostatic simulations of the strength of the imposed potential, the gate-voltage induced variation is indeed expected to exceed the disorder levels (Fig. 6.2). The asymmetry between positive and negative top gate values seen in the data could possibly be explained by effective disorder levels being smaller when charges accumulate mainly underneath the grid gate, as compared to when charges accumulate mainly underneath the dielectric. Finally, in Fig. 6.5(b) we resolve separate lines at the onset of accumulation for negative top gate voltages. Even though we expect to see evidence of miniband formation, we do not attribute these splittings to miniband formation, as they show a much larger periodicity in back gate voltage than the 6 mV expected from the density of states calculation (see below).

For devices of the second design, the widening of the onset of accumulation is less pronounced, but the effect of gating is seen at finite magnetic fields, where a voltage difference between the grid and top gate effectively blurs out the gaps between Landau levels (Fig. 6.5(c-d)). This indicates that the imposed local potential variation must be comparable to or stronger than the Landau level spacing at 1 T (1.7 meV). We conclude that also for the second design, the 200 nm periodic potential exceeds disorder levels.

Increasing further the amplitude of the potential variation induced by the gates was limited by saturation of the gating effect. For the first gate design, we find a saturation to the effect of the top gate in gating the 2DEG at gate voltages exceeding 35 V in absolute value. This could be a sign of charges building up at the interface of the capping layer

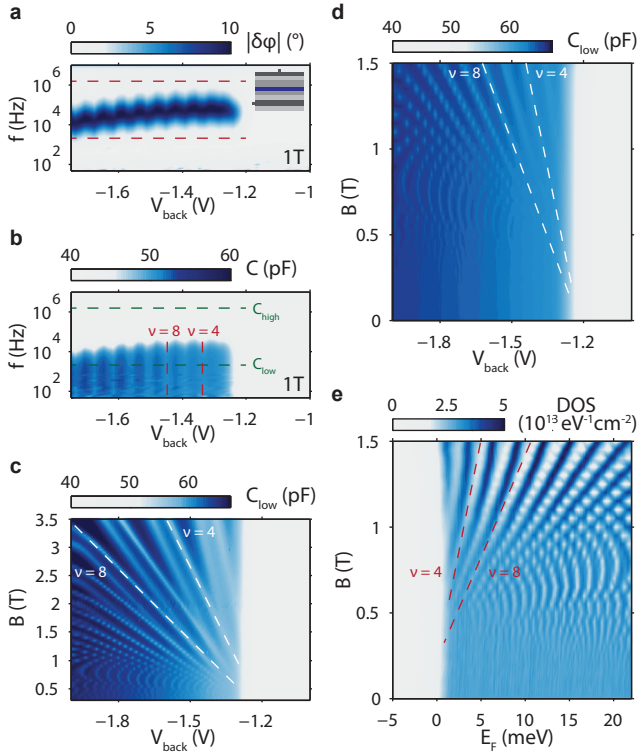


Figure 6.4: (a) Bridge equilibrium phase as function of back gate bias and measurement frequency. (b) Global gate capacitance as function of back gate bias and measurement frequency. (c) Landau fan diagram: device capacitance as function of back gate bias and magnetic field, showing onset of accumulation, integer quantum Hall levels and exchange splitting. (d) Zoom in of Landau fan diagram for low field regime of (c). (e) Calculated density of states (DOS) from (d), allowing us to assess disorder from Landau level visibility. The gaps at filling factors $\nu = 4$ and $\nu = 8$ are indicated. At lower fields, the small Landau level spacing leads to aliasing in the image.

and the dielectric, or in the dielectric itself, which screen the effect of the top gate. This saturation limits the potential we can impose on the 2DEG. For the second gate design, a maximum voltage difference of roughly 2 V can be set between the back gate and the surface gates before leakage starts to occur. As an attempt to allow for larger gate voltages before leakage through the heterostructure occurs, we have tried the same fabrication but with an additional 5 nm ALD-grown AlO_x dielectric placed underneath the grid gate. This indeed prevents leakage but the gating effect saturated at the same voltages where leakage occurred for devices without this additional dielectric. Therefore, 2 V was still the maximum voltage we could apply between the back and surface gates in the second design.

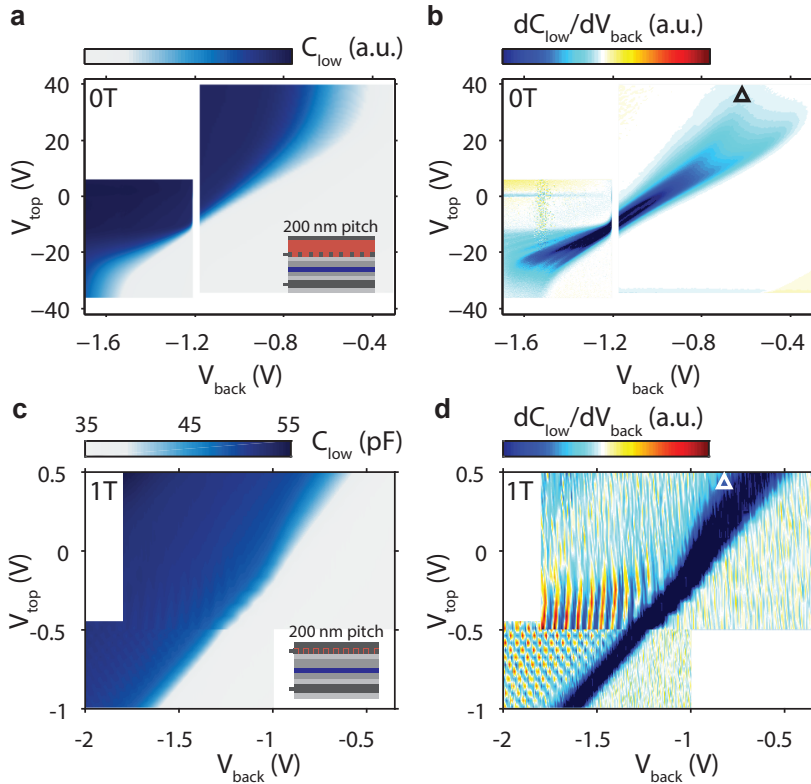


Figure 6.5: (a) Capacitance as function of back gate and top gate voltages for a device with a 200 nm periodic square grid gate and a 360 nm SiO₂ dielectric separating the two gate layers (see inset and Fig. 6.2(b)). (b) Derivative of capacitance data. (c)-(d) Similar data taken for a device with aluminum overlapping gates (see inset) at 1 T. Black and white triangles in (b) and (d) indicate the gate voltages used in Fig. 6.2 (d) and (f) respectively. The onset of accumulation shows broadening in (b) whereas Landau levels get blurred out with increasing top gate voltage in (d)

6.5. DISCUSSION: WHAT TO SEARCH FOR IN FUTURE DATA

As we have just seen, (i) the periodic potential exceeds disorder levels. In order to see Hofstadter's butterfly and Mott physics, however, we also need to (ii) be able to resolve the induced density of states modulations and (iii) the lattice potential from the grid itself should be sufficiently homogeneous. The latter two considerations will be discussed below, based on the data presented.

Using either gate design, we find both gates to influence the accumulation of charges in the quantum well as expected, but neither shows clear evidence of a lattice potential imposed on the 2DEG (Fig. 6.5). At zero magnetic field, a lattice potential would lead to minibands that manifest as periodic modulations in the density of states (and capacitance) with a period corresponding to two electrons per lattice site, or $5 \times 10^9 \text{ cm}^{-2}$ for a 200 nm square grid. Expressed in mV on the back gate, this corresponds to a period of 6

mV. Furthermore, at finite magnetic field, Landau levels are expected to show structure due to Hofstadter butterfly physics[16, 27], with the largest gaps expected around $k \pm 1/4$ of a flux quantum Φ_0 threading each lattice plaquette (with k an integer; Φ_0 corresponds to 104 mT for a 200 nm grid). Finally, a strong enough periodic potential would allow interaction effects to dominate. Miniband gaps are expected to split as filling starts to occur with a period of one electron per lattice site, akin to the interaction-driven Mott transition [12]. None of these effects are visible in Fig. 6.5 nor in many detailed targeted scans of magnetic field and gate voltages on devices with 200 and 100 nm grid gate periodicity.

If we compare the $5 \times 10^9 \text{ cm}^{-2}$ density modulations expected from miniband formation with the $1.2 \times 10^{10} \text{ cm}^{-2}$ broadening of low-field Landau levels (global gate devices at high densities, i.e., we do not have evidence that we can resolve density variations below $1.2 \times 10^{10} \text{ cm}^{-2}$), it is reasonable that gaps are not yet seen opening up at densities corresponding to the filling of (pairs of) electrons on each lattice site. This suggests that either lattice size or wafer disorder has to be further reduced. As it proves hard to lift off plaquettes of metal that are smaller than roughly 40 nm by 40 nm, there is not much room to reduce lattice dimension further in this particular fabrication scheme (Fig. 6.3(a)). For 100 nm pitch grids, the period of the density modulations is expected to be four times larger but is still comparable to current best-case scenario Landau level broadening. As such, reducing intrinsic disorder seems necessary. An appropriate goal would be to make double layer gate devices with Landau levels that are distinguishable at fields below 100 mT.

The visibility of Hofstadter butterfly gaps depends not only on the intrinsic disorder in the device but also on the inhomogeneity in the plaquette sizes, as this would entail a different number of flux quanta threading through different plaquettes. If the size variations from electron micrographs of our devices translated to identical size variations in the periodic potential (Fig. 6.3(b)), we should just be able to distinguish the largest gaps[16]. It is hard to assess, however, whether this indicator from the electron micrographs directly correlates to the relevant physics in the 2DEG.

6.6. OUTLOOK

There is room for further optimization of these devices. On the heterostructure side, the distance between the back gate and the 2DEG can be further increased, compensating with a decreased Al content in the tunnel barrier to keep the tunnel-rate fixed. Furthermore, part of the spacer layer can be grown at reduced temperatures, which has been shown to strongly reduce disorder by limiting the diffusing of Si dopants from the back gate region[25]. On the fabrication side, there is still room left for a modest reduction of the lattice periodicity with the current lift-off process. Even smaller length scales can be obtained by switching to dry etching of the grid pattern, albeit at an unknown impact to wafer disorder levels.

In summary, we have demonstrated a novel platform intended for the realization of artificial lattices of interacting particles. Although fine-tuning the design to the point where a sufficiently homogeneous and strong periodic potential can be applied remains to be done, the quantum Hall data already show how the strong-interaction, low-temperature limit can be reached. Such a platform has potential for studying the interaction-driven

Mott insulator transition[12, 28] and Hofstadter butterfly physics[5] with finite interactions, and can be extended from the steady-state measurements presented here to include time-domain measurements of excited states[26].

6.7. SUPPLEMENTARY MATERIAL

6.7.1. CAPACITANCE BRIDGE

The capacitance bridge is built on a printed circuit board (PCB) that is mounted on the 10 mK mixing chamber stage of a dilution fridge and whose main components are the device, the reference capacitor and a high electron mobility transistor (HEMT, that serves as the first amplifier). By mounting the HEMT orthogonal to the PCB surface, we can apply magnetic fields to the sample without influencing the amplification chain. All D/C lines on the sample PCB have R/C filters on top of the filtering in the fridge. A 10 and 40 M Ω resistance is used to bias the bridge point and top gate in D/C, respectively, and a bias-tee is added to bias the back gate on top of the measurement signal. The high-frequency lines are not attenuated in the fridge, as we found this to lead to ground loop issues, but are instead attenuated on the PCB itself. Measurement excitations are generated using a signal generator at room temperature. The bridge point voltage is amplified further at 0.7 K and at room temperature and measured using a lock-in.

An iterative scheme is implemented to minimize the bridge point voltage by updating the amplitude ratio and phase difference of the two excitations as gate voltages and applied magnetic field are changed. The excitation on the sample side is kept constant and the excitation on the reference capacitor side is updated based on the secant method. For this, we model the bridge as a linear system of complex variables: $Y = AX + B$, where X is the reference signal, Y is the output from the lock-in, and A and B are complex numbers. Given two iterations with reference signals X_i and X_{i+1} and respective output values Y_i and Y_{i+1} , A and B are calculated as well as $X_{i+2} = -B/A$, which is subsequently set and Y_{i+2} measured. As the first two iterations, we take the last set reference signal as well as a point with a typically 1 % higher amplitude and a tenth of a degree increased phase. Convergence is reached when the amplitude difference between the last two reference signals drops below some pre-defined value, typically chosen to be several parts per thousand of the amplitude itself. The sample capacitance C_{sample} follows from the reference capacitor value C_{ref} and the applied amplitude ratio $R = \frac{V_{\text{ref}}}{V_{\text{sample}}}$ and phase difference $\delta\phi = \pi + \phi_{\text{ref}} - \phi_{\text{sample}}$ at equilibrium: $C_{\text{sample}} = \cos(\delta\phi)RC_{\text{ref}}$.

6.7.2. DESIGN AND FABRICATION DETAILS

As discussed earlier, several different designs and fabrication recipes were used throughout this work to fabricate devices. In the first part, we give some general information on steps that have been employed for many of these fabrication runs. Next we describe fabrication processes of different dielectrics used in the first design to separate the top and grid gate layers. Finally, we provide detailed information for a fabrication run of the second design with overlapping aluminum gates, which serves as a clear example from which the steps required for fabricating the other devices measured can be deduced.

All lithography steps were performed using electron beam lithography (Vistec EBPG 5000+ or 5200) at 100kV acceleration voltage. Etching $\text{Al}_x\text{Ga}_{1-x}\text{As}$ was done using di-

luted Piranha (1:8:240 H_2SO_4 : H_2O_2 : H_2O) yielding etch rates of roughly 4 nm/s. The actual etch rate decreases on a timescale of minutes as the H_2O_2 concentration slowly decreases. Spinning is done at 500 rpm for 5 seconds and then for 55 seconds at speeds listed below. Etching SiO_2 and AlO_x was done using buffered HF (BOE 1:10) solutions. After either type of wet etch, devices are rinsed repeatedly in H_2O . Adhesion issues for resists with HF etch times longer than 20 s mean iterative etching and re-baking is necessary. For the 366 nm AlO_x layers, this meant we had to use a dry Cl etch to etch the bulk of the depth of the vias before finishing with a wet etch. Metallic layers were deposited using electron-beam evaporation at room temperature and subsequent lift-off in a solvent.

The first design, with a thick dielectric separating the two gate layers, has been fabricated with two different dielectrics. For the results of Fig. 6.5(a-b), plasma-enhanced chemical vapor deposition (PECVD) of 360 nm of SiO_2 as dielectric was used, which was found to introduce phase-noise during capacitance-bridge measurements. We have also fabricated devices with 366 nm of plasma-enhanced atomic layer deposition (ALD) grown AlO_x dielectric (optical image in Fig. 6.6(a)). Although these devices had less phase-noise, they showed large top gate hysteresis, rendering them practically impossible to measure with (Fig. 6.6(b)). Furthermore, etching small vias through such a thick layer of alumina is very cumbersome. All devices of the first design had low yield in wire-bonding because of poor adhesion of the dielectric layers to the GaAs surface.

An overview of the fabrication steps for realizing double-layer gate devices with aluminum gates (second design) is given below. See Fig. 6.7(a) for schematic side views of the process and Fig. 6.7(e) for the top view of a finished device.

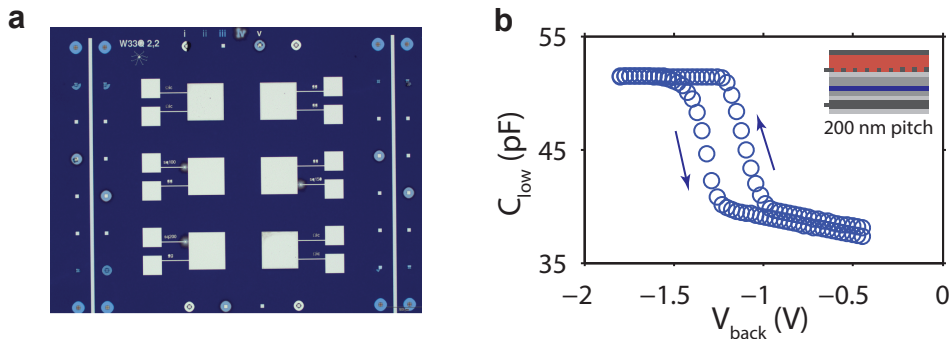


Figure 6.6: (a) Optical image of a device cell of the first design with a 366 nm thick AlO_x dielectric layer. Top left and bottom right squares are ohmic contacts, which could have also been fabricated on the back side of the wafer. The other squares are three double-gate devices and one single-gate device, each with two bond pads. Contacting the grid layer underneath the dielectric is done using etched vias. (b) Capacitance as a function of back gate for a device from (a), showing hysteresis as function of either top or back gate voltage (shown).

- Ohmic contacts - spin PMMA 495K A8 resist at 6000 rpm - bake 15 min at 175 °C (400 nm) - lithography - development 60 s in 1:3 MIBK/IPA - wet etch of 180 nm in diluted Piranha - evaporation of 5/150/25 nm Ni/AuGe/Ni - lift-off in acetone and

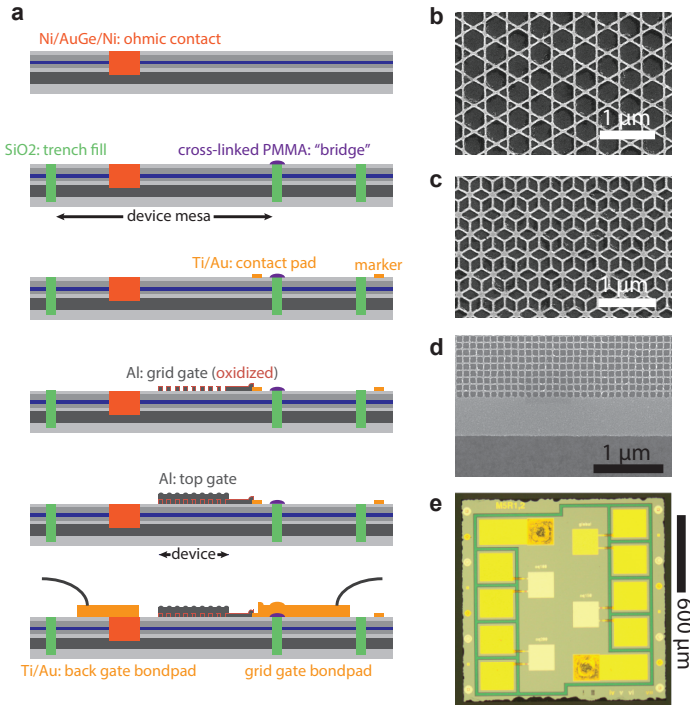


Figure 6.7: (a) Overview of the fabrication process for overlapping gates. Note that the top gate bondpad is not shown in this view, and that the mesa and bridge steps are shown added to the same figure. (b) Electron micrograph of a kagome-type lattice fabricated using the same lift-off recipe as used for the square grids, with 5/15 nm Ti/Au. Note that for non-square lattice such as this, a different lattice is imposed on the 2DEG depending on the polarity of the voltage difference between the grid and top gate. (c) Electron micrograph of a 5/15 nm Ti/Au dice-type lattice gate. (d) Electron micrograph at the edge of a square 100 nm pitch grid, showing the overdosed 'frame' that is used to counter proximity effect induced inhomogeneity effects at the edge of the grid. (e) Optical image of a device cell containing two ohmic contacts at top left and bottom right as well as a single-gate device on the top right and three double-gate devices. The dielectric-filled etched region that separates the device mesa from the bonding pads is visible in green.

IPA rinse - anneal 60 s at 440 °C in forming gas.

- Mesa etch - spin PMMA 495K A8 resist at 6000 rpm - bake 15 min at 175 °C (400 nm) - lithography - development 60 s in 1:3 MIBK/IPA - wet etch of 700 nm in diluted Piranha - sputtering 700 nm of SiO₂ - lift-off in acetone and IPA rinse.
- Bridges - spin PMMA 495K A8 resist at 6000 rpm - bake 15 min at 175 °C (400 nm) - lithography - cross-link PMMA strips through electron beam overdose at 25 mC/cm². These sections act as bridges over which the leads will connect sample mesa and bond pad regions.
- Connection pads and markers - spin PMMA 495K A8 resist at 6000 rpm - bake 15 min at 175 °C (400 nm) - lithography - development 60 s in 1:3 MIBK/IPA - evaporation of 10/50 nm Ti/Au - lift-off in acetone and IPA rinse. These sections act

either as markers or as pads that will be contacted on the top both by the Al gates and the leads contacting the bond pads. We found these thin layers of metal to be the most robust way to make an electrical connection (typically several Ohm) between the Al gates and the Au bond pads.

- Grid gate - spin CSAR 62.04 resist at 5000 rpm - bake 3 min at 150 °C (72 nm) - lithography - development 70 s pentyl acetate and 60 s 1:1 MIBK:IPA - evaporation of 20 nm Al - lift-off in NMP at 70 °C using soft ultrasound excitation for 4 hrs and subsequent acetone and IPA rinse - oxidation in 20 min at 200 °C at 100 mTorr and 300 W RF power using the remote plasma of an ALD machine. We have optimized the lithographic sequential writing such that a 200 μm x 200 μm grid is written in one go and at under a minute, avoiding stitching errors and reducing the effect of drift (typically several tens of nm/min). We have done this by direct programming of an iterative sequence that the e-beam follows in writing the grid instead of the standard procedure of converting a design file (in this case a large square grid) to an e-beam lithography file using BEAMER software. Furthermore, we add a 200 nm thin frame around the grids whose overdose is chosen to counter proximity edge effects (Fig. 6.7(d)). Note also that we found the conflicting requirements of high resolution and undercut required for lift-off to be best served using a single layer CSAR62 resist. Finally, we find feature size, yield and reproducibility to be limited by the grain size of the evaporated Al, instead of by the resist mask or lithography process. To achieve a smaller grain size, we used a fast Al evaporation rate of 0.2 nm/s. As such, Ti/Au but especially Ti/AuPd gates are easier to fabricate than Al gates but they cannot be oxidized and would require actual deposition of a dielectric. Also note that the lift-off based fabrication of grids allows for different lattice types to be made, see Fig. 6.7(b-d).
- Top gate - spin PMMA 495KA8 resist at 6000 rpm - bake 15 min at 175 °C (400 nm) - lithography - development 60 s in 1:3 MIBK/IPA - evaporation of 50 nm Al - lift-off in acetone and IPA rinse.
- Bonding pads - spin OEBR-1000 (200cp) lift-off resist at 3500nm - bake 30 min at 175 °C (500 nm) - spin PMMA 950K A2 resist at 2000 rpm - bake 10 min at 175 °C (90 nm) - lithography - evaporation of 50/200 nm Ti/Au - lift-off in acetone and IPA rinse.

6.7.3. CONVERSION FROM CAPACITANCE TO DENSITY OF STATES

In calculating density of states from capacitance data, we follow a procedure described before[18]. We model the system as a parallel plate capacitor made up of the top and bottom gates, with the potential for added charges at the location of the quantum well, as sketched in Fig. 6.8. As a start, $C_{\text{high/low}}$ are measured as function of gate voltages and magnetic field values (Fig. 6.9(a)). Note that the heterostructure stack is designed to keep the tunnel frequency in the middle of the experimental measurement window (Fig. 6.4(a-b) in the main text): below 1 kHz signal to noise ratio declines (mainly because of the $1/f$ noise of the first transistor in the amplification chain) and above 2 MHz systematic errors occur (we find asymmetric cross-talk between the two excitation signals and the second transistor in the amplification chain).

The total voltage difference over the device is a combination of the electric fields $V = V_{\text{back}} - V_{\text{top}} = E_1(w + d) + E_2d$, which in turn depends on the charges on the plates as $V = \frac{\sigma_{\text{top}}(w+d)}{\epsilon} + \frac{\sigma_{\text{QW}}d}{\epsilon}$. The total capacitance, which is the one measured at low enough frequencies, is defined as $C_{\text{low}} = \frac{\partial Q}{\partial V} = A \frac{\partial \sigma_{\text{top}}}{\partial V} = \frac{\epsilon A}{w+d} - \frac{dA}{w+d} \frac{\partial \sigma_{\text{QW}}}{\partial V}$ + small terms that depend on changing distances and which we ignore. The first term describes the bare capacitor, and is therefore equal to the total capacitance measured at high frequencies: $C_{\text{high}} = \frac{\epsilon A}{w+d}$. The second term is the one of interest. It describes changes between the capacitance measured at low and high frequency because of the addition of charges in the quantum well, which allows us to infer changes in electron density using $\frac{\partial n}{\partial V} = -\frac{1}{e} \frac{\partial \sigma_{\text{QW}}}{\partial V} = \frac{1}{eA} \frac{w+d}{d} (C_{\text{low}} - C_{\text{high}})$ (Fig. 6.9(b)).

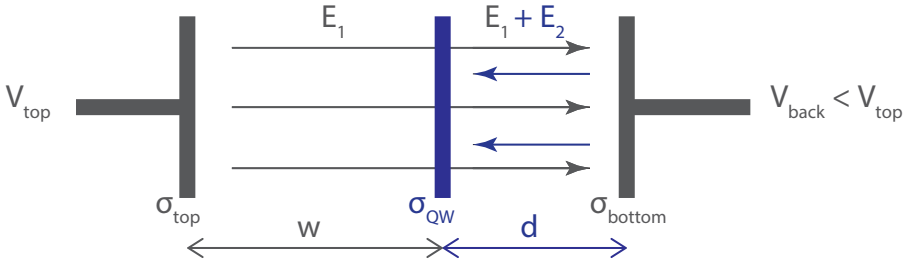


Figure 6.8: Schematic representation of the device as a parallel plate capacitor of distance $w + d$ with an inserted quantum well at a distance d from the back gate. When the DOS at the quantum well is nonzero, charges can build up.

The voltage required to change the Fermi level E_F of the quantum well can be found using a similar deduction to the one described above, and is described by a voltage-dependent lever arm $\alpha \equiv -e \frac{\partial V}{\partial E_F}$. We find the lever arm by following the dependence of the Fermi level in the quantum well through changes in the electric field as $\frac{\partial E_F}{\partial V} = -ew \frac{\partial E_1}{\partial V} = -e \left(\frac{w}{w+d} + \frac{e}{\epsilon} \frac{wd}{w+d} \frac{\partial n}{\partial V} \right)$ (Fig. 6.9(c)). The first term describes how the Fermi level of a gapped system in the quantum well ($\delta n = 0$) changes with bias as expected given its relative location $\frac{w}{w+d}$ between the plates of a simple parallel plate capacitor (Fig. 6.9(c)). It is the second term that encompasses the electron filling, showing the lever arm to increase when charges can be added to the quantum well (after accumulation this becomes the dominant term, see Fig. 6.9(b)). Given the above expressions for density and Fermi level changes as function of gate voltage, we can define the density of states in the 2DEG through $DOS = \frac{\partial n}{\partial V} \frac{\partial V}{\partial E_F} = \frac{1}{e^2 A} \frac{w+d}{d} \alpha (C_{\text{low}} - C_{\text{high}})$ (Fig. 6.9(d)). As indicated by changes in C_{high} in Fig. 6.9(a), the distances describing the system are non-static with gate voltage. In the case of $(w + d)$, this is most likely due to back gate charges populating part of the spacer layer as the electric fields bend the conduction band edge, indeed increasing C_{high} for more negative back gate voltages. The exact location of the charges in the quantum well and related distance d , however, we cannot directly infer from an independent measurement. As a first guess, the growth distances combined with the $(w + d)$ extracted from C_{high} suffices. A better estimate can be made using the known

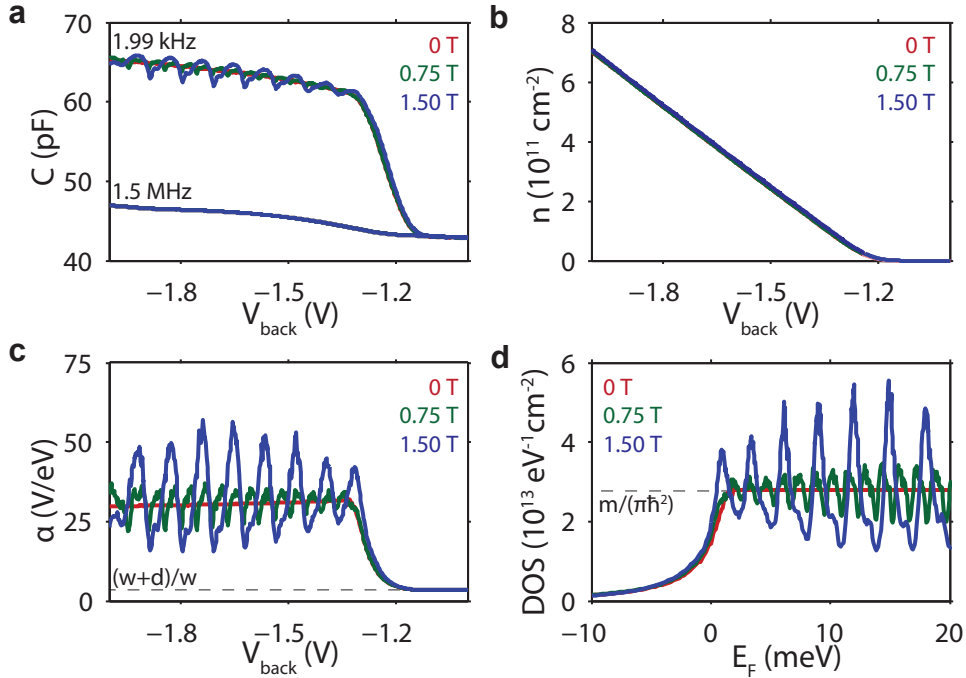


Figure 6.9: (a) Capacitance as function of back gate bias at 0 T (red), 0.75 T (green) and 1.5 T (blue), both below and above the tunnel frequency. Top gate is kept constant for all measurements as it serves as the bridge point, which is also directly contacted to the gate of the first transistor in the amplification chain. (b) Density as function of back gate bias. As the system becomes more gapped between Landau levels at higher fields, steps start to form in the graph that indicate the filling of distinct levels at well-defined densities. (c) Lever arm as function of back gate bias. Note that the quantum capacitance of a large density of states in the 2DEG increases the voltage required to change the Fermi level, as expected. At zero density of states, however, the lever arm is simply the geometric ratio expected from the relative location of the quantum well between the top and bottom gate. (d) Density of states as function of the Fermi energy, which is the integrated lever arm. We choose zero in energy to lie close to accumulation.

linear degeneracy of Landau levels with magnetic field, $n_{\text{LL}} = \frac{2eB}{h}$ (Fig. 6.9(b)). To obtain the best possible calibration, however, we compensate for any further dependence of the relative quantum well position on back gate voltage by pegging the 0 T DOS after accumulation to the expected value of $\frac{m}{\pi\hbar^2} \approx 2.8 \times 10^{13} \text{ eV}^{-1} \text{ cm}^{-2}$ (Fig. 6.9(d)), and use this calibration for nonzero magnetic field values.

BIBLIOGRAPHY

- [1] T. Hensgens, U. Mukhopadhyay, P. Barthelemy, R. F. L. Vermeulen, R. N. Schouten, S. Fallahi, G. C. Gardner, C. Reichl, W. Wegscheider, M. J. Manfra, and L. M. K. Vandersypen, *Journal of Applied Physics* **124**, 124305 (2018) .
- [2] J. I. Cirac and P. Zoller, *Nature Physics* **8**, 264 (2012).

- [3] M. C. Rechtsman, J. M. Zeuner, Y. Plotnik, Y. Lumer, D. Podolsky, F. Dreisow, S. Nolte, M. Segev, and A. Szameit, *Nature* **496**, 196 (2013).
- [4] D. Tanese, E. Gurevich, F. Baboux, T. Jacqmin, A. Lemaître, E. Galopin, I. Sagnes, A. Amo, J. Bloch, and E. Akkermans, *Physical Review Letters* **112**, 146404 (2014).
- [5] D. Hofstadter, *Physical Review B* **14**, 2239 (1976).
- [6] C. R. Dean, L. Wang, P. Maher, C. Forsythe, F. Ghahari, Y. Gao, J. Katoch, M. Ishigami, P. Moon, M. Koshino, T. Taniguchi, K. Watanabe, K. L. Shepard, J. Hone, and P. Kim, *Nature* **497**, 598 (2013).
- [7] L. A. Ponomarenko, R. V. Gorbachev, G. L. Yu, D. C. Elias, R. Jalil, A. A. Patel, A. Mishchenko, A. S. Mayorov, C. R. Woods, J. R. Wallbank, M. Mucha-Kruczynski, B. A. Piot, M. Potemski, I. V. Grigorieva, K. S. Novoselov, F. Guinea, V. I. Fal'ko, and A. K. Geim, *Nature* **497**, 594 (2013).
- [8] B. Hunt, J. D. Sanchez-Yamagishi, a. F. Young, M. Yankowitz, B. J. LeRoy, K. Watanabe, T. Taniguchi, P. Moon, M. Koshino, P. Jarillo-Herrero, and R. C. Ashoori, *Science* **340**, 1427 (2013).
- [9] G. L. Yu, R. V. Gorbachev, J. S. Tu, A. V. Kretinin, Y. Cao, R. Jalil, F. Withers, L. A. Ponomarenko, B. A. Piot, M. Potemski, D. C. Elias, X. Chen, K. Watanabe, T. Taniguchi, I. V. Grigorieva, K. S. Novoselov, V. I. Fal'ko, A. K. Geim, and A. Mishchenko, *Nature Physics* **10**, 525 (2014).
- [10] C. A. Stafford and S. Das Sarma, *Physical Review Letters* **72**, 3590 (1994).
- [11] E. Manousakis, *Journal of Low Temperature Physics* **126**, 1501 (2002).
- [12] T. Byrnes, N. Kim, K. Kusudo, and Y. Yamamoto, *Physical Review B* **78**, 075320 (2008).
- [13] A. Singha, M. Gibertini, B. Karmakar, S. Yuan, M. Polini, G. Vignale, M. I. Katsnelson, A. Pinzuk, L. N. Pfeiffer, K. W. West, and V. Pellegrini, *Science* **332**, 1176 (2011).
- [14] P. Barthelemy and L. M. K. Vandersypen, *Annalen der Physik* **525**, 808 (2013).
- [15] K. Ensslin and P. Petroff, *Physical Review B* **41**, 12307 (1990).
- [16] M. Geisler, J. Smet, V. Umansky, K. von Klitzing, B. Naundorf, R. Ketzmerick, and H. Schweizer, *Physical Review Letters* **92**, 256801 (2004).
- [17] C. Albrecht, J. Smet, K. von Klitzing, D. Weiss, V. Umansky, and H. Schweizer, *Physical Review Letters* **86**, 147 (2001).
- [18] R. C. Ashoori, *PhD thesis*.
- [19] R. Ashoori, H. Stormer, J. Weiner, L. Pfeiffer, S. Pearton, K. Baldwin, and K. West, *Physical Review Letters* **68**, 3088 (1992).
- [20] R. Ashoori, J. Lebens, N. Bigelow, and R. Silsbee, *Physical Review B* **48**, 4616 (1993).

- [21] R. E. Cavicchi and R. H. Silsbee, *Review of Scientific Instruments* **59**, 176 (1988) .
- [22] L. P. Kouwenhoven, C. M. Marcus, P. L. McEuen, S. Tarucha, R. M. Westervelt, and N. S. Wingreen, "Electron transport in quantum dots," in *Mesoscopic Electron Transport*, edited by L. L. Sohn, L. P. Kouwenhoven, and G. Schön (Springer Netherlands, Dordrecht, 1997) pp. 105–214.
- [23] S. J. Angus, A. J. Ferguson, A. S. Dzurak, and R. G. Clark, *Nano Letters* **7**, 2051 (2007), pMID: 17567176 .
- [24] T. Ando and Y. Uemura, *Journal of the Physical Society of Japan* **37**, 1044 (1974) .
- [25] J. Jang, B. M. Hunt, L. N. Pfeiffer, K. W. West, and R. C. Ashoori, *Nature Physics* **13**, 340 (2017).
- [26] O. E. Dial, R. C. Ashoori, L. N. Pfeiffer, and K. W. West, *Nature* **448**, 176 (2007).
- [27] D. Pfannkuche and R. Gerhardt, *Physical Review B* **46**, 12606 (1992).
- [28] M. Imada, A. Fujimori, and Y. Tokura, *Reviews of Modern Physics* **70**, 1039 (1998).

7

CONCLUSIONS AND OUTLOOK

7.1. CONCLUSIONS

The aim of my research for the last four years was to scale up arrays of gate-defined quantum dots and use them in analog simulations of the Fermi-Hubbard model. In this section, I summarize the key findings of this thesis.

Chapter 3 describes our effort in fabrication to scale up the number of quantum dots in an array using a bottom-up approach. We employ a double-layer gate design to fabricate the 2x2 dot array device. A sputtered slab of SiN_x is used as the dielectric material to electrically separate the gates in different layers. We successfully developed a recipe to lift-off this dielectric slab with low standing-edges. This facilitates a fairly easy and flexible way of fabricating multi-layer gate stacks. We also demonstrate that more the traditional way of scaling up linear arrays works up to eight dots.

We establish the 2x2 quantum dot array as a promising analog quantum simulator of the Fermi-Hubbard model in chapter 4. The electron filling of each dot is controlled in the few-electron regime. Both the on-site (U) and the inter-site (V) interaction energies are measured accurately. We show that the hopping energy (t) of the Fermi-Hubbard model can be tuned to attain values larger than the thermal energy of the system, even with a single electron in each dot. This hopping can be increased substantially by increasing the electron occupation of the dots. The size of the center gate currently limits the access to even larger values of t , which can be solved easily by changing the gate width in subsequent fabrication runs. We perform high fidelity spin-readout of the electrons using the Pauli spin blockade technique. Although we achieve desirable tuning of the hopping energies (t) and the chemical potentials (μ) with the help of virtual gates [1, 2], the tuning process takes significant time and effort, as the disorder in the 2DEG needs to be compensated using gate voltages to create and manipulate these dots. This is currently the biggest challenge in tuning the quantum dot arrays.

In chapter 5, we present evidence of Nagaoka ferromagnetism using the 2x2 dot array. We observe the signature of a ferromagnetic ground state in an almost-half-filled lattice, driven by interactions. The high-level of control in the system enables us to manipulate the Hamiltonian parameters and perform measurements that confirm the validity of our interpretation. This is the first experimental realization of this ferromagnetism, more the fifty years after Nagaoka's theoretical prediction in 1966. This experiment demonstrates the potential of gate-defined quantum dot arrays in simulating the Fermi-Hubbard physics. At the same time, it exhibits the potential of NISQ era quantum technologies [3].

We explore a drastic scale-up of quantum dot arrays using a top-down approach with only global control in chapter 6. This approach requires homogeneous 2DEGs with low disorders as the lack of individual control knobs makes it impossible to compensate for these disorders. Although we used specially designed 2DEGs to increase homogeneity, the disorder level was still too high to form large arrays of quantum dots and to measure periodic effects through capacitance spectroscopy.

From the results in this thesis, I conclude that small arrays of quantum dots are currently well poised to simulate the Fermi-Hubbard physics. We have seen great potential to control different Hubbard parameters in a small scale array. Gradually scaling up the system size, while keeping the same level of control, seems well within reach, although with some effort in both fabrication and tuning of the dot arrays. Whereas, scaling to large 2D arrays of quantum dots requires significant improvement in 2DEG homogeneity as well as device fabrication.

7.2. OUTLOOK

The results discussed in this thesis demonstrate the potential of gate-defined quantum dot arrays in simulating the Fermi-Hubbard model. In this section, I will discuss a few possible ways to build upon my research. I will describe the current challenges in achieving these and their possible solutions.

7.2.1. SIMULATION USING A 2X2 DOT ARRAY DEVICE

The control over the device parameters in the 2x2 dot array facilitated the first experimental observation of Nagaoka ferromagnetism, which is described in chapter 5. These same controls can be leveraged to explore several interesting phenomena in different regimes in the same system. With one electron per dot and sufficiently low tunnel coupling between the dots, the system can be described by the Heisenberg model of spin-spin interaction (see section 2.2). When the Heisenberg interaction energy between all nearest-neighbor double-dot pairs are equal in this regime, the ground state of the system is predicted to form a resonance valance bond (RVB) state [4–6]. In a 2x2 dot array, this RVB state will manifest as an oscillation between two vertical and two horizontal singlets (see Fig 7.1).

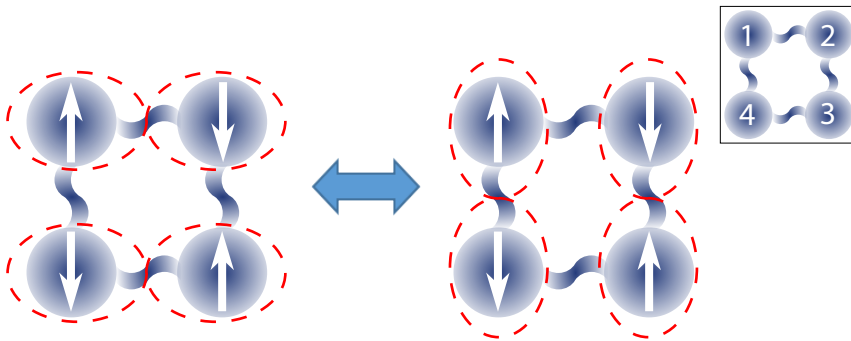


Figure 7.1: The RVB state in the 2x2 dot array, given by an oscillating pair of singlets between the horizontal (left) and the vertical (right) pairs of dots. The inset shows a schematic of the dot array with dot numbers.

The Pauli spin-blockade measurement allows one to determine if two electron spins in two separate dots are in singlet or triplet configuration (see subsection 2.1.5). A correlation of PSB measurements between two opposite double dots (vertical or horizontal) can be used to look for evidence of the RVB state in the system. Next, we calculate the

probability of the correlated singlet measurements for the two horizontal double dots (double dots 12 and 34). The expected RVB ground state should have states $|S^{12}S^{34}\rangle$ and $|S^{14}S^{23}\rangle$ with equal probability (see subsection 5.6.3 for the definitions of $|S\rangle$, $|T_+\rangle$, $|T_0\rangle$, and $|T_-\rangle$). Taking the relevant normalization into account, the ground state turns out to be:

$$\psi_{RVB} = \frac{1}{\sqrt{3}} (|S^{12}S^{34}\rangle - |S^{14}S^{23}\rangle) \quad (7.1)$$

Now for this ground state, the probability of measuring correlated singlet in the horizontal double dots is given by:

$$\begin{aligned} \|\langle S^{12}S^{34} | \psi_{RVB} \rangle\|^2 &= \|\langle S^{12}S^{34} | \frac{1}{\sqrt{3}} (|S^{12}S^{34}\rangle - |S^{14}S^{23}\rangle) \rangle\|^2 \\ &= \frac{1}{3} \|\langle S^{12}S^{34} | S^{12}S^{34} \rangle - \langle S^{12}S^{34} | S^{14}S^{23} \rangle\|^2 \\ &= \frac{1}{3} \|1 - \langle S^{12}S^{34} | \frac{1}{2} (|\uparrow\downarrow\rangle - |\downarrow\uparrow\rangle)^{14} (|\uparrow\downarrow\rangle - |\downarrow\uparrow\rangle)^{23} \rangle\|^2 \\ &= \frac{1}{3} \|1 - \frac{1}{2} \langle S^{12}S^{34} | (|\uparrow\uparrow\downarrow\downarrow\rangle - |\uparrow\downarrow\uparrow\downarrow\rangle - |\downarrow\downarrow\uparrow\uparrow\rangle + |\downarrow\uparrow\downarrow\uparrow\rangle) \rangle\|^2 \\ &= \frac{1}{3} \|1 - \frac{1}{2} \langle S^{12}S^{34} | (T_+^{12}T_-^{34} + T_-^{12}T_+^{34} - T_0^{12}T_0^{34} - S^{12}S^{34}) \rangle\|^2 \\ &= \frac{1}{3} \|1 + \frac{1}{2}\|^2 = \frac{1}{3} * \left(\frac{3}{2}\right)^2 = \frac{3}{4} \end{aligned} \quad (7.2)$$

So for the RVB state, the probability of measuring correlated singlets in horizontal double dots is $\frac{3}{4} * 100\% = 75\%$. The probability of measuring correlated singlets in vertical double dots is also 75%, following similar calculations. If due to measurement inaccuracies the measured correlation is different from the expected value of 75%, this equal correlation between horizontal and vertical double dots can be utilized to demonstrate the evidence of the RVB state. These correlation measurements require consecutive PSB measurements in two double-dot pairs. This can be achieved using a readout protocol similar to what is reported in Ref. [7].

7.2.2. SCALING OF QUANTUM DOT ARRAYS

Scaling up the number of quantum dots in an array is essential for both quantum simulation and computation experiments. There are different aspects to this scaling. First, we need different gate designs to make arrays of various shapes. Significant fabrication development might be needed to make some of these gate structures. Once we fabricate these gate structures, the next set of challenges appear in tuning these dot arrays using gate voltages. As several gate voltages affect each parameter of the dot array, this tuning process can become rather complex with increasing number of dots. Finally, we need to think of sensing methods for the dot arrays. Charge sensing with sensing dots is currently the popular choice. This sensing technique requires capacitive coupling between the sensing dot and the dot array, which is achieved by placing the sensing dot close

to the dot array. However, the new gate architectures to create bigger dot arrays might not allow enough space for sensing dots adjacent to the dot array, forcing us to adopt different sensing methods.

The quantum dot community has historically been most comfortable in working with linear dot arrays. As a result, most efforts of scaling has been based on linear arrays. There are a few advantages of scaling the number of dots in a linear array. We can copy-paste the gate structure to create single dots next to one another to increase the size of the array, without any major problem. Moreover, the gate design allows enough space for strategically creating sensing dots to charge sense a linear array of arbitrary length. Furthermore, the recent developments in tuning strategy and technique enable reasonably fast tuning of the linear arrays. The main challenges of tuning come from the disorder in the substrate and different cross-capacitance between the gates and the dots. These cross-talks can be compensated using virtual gates, which are linear combinations of multiple gate voltages designed to control only a single parameter of the dot array. The ‘n+1 method’, introduced in Ref. [8], provides a powerful protocol to tune any number dots in a linear array and reliably load each dot with the desired number of electrons. Finally, tuning of the tunnel couplings between different pairs of dots can be automatized following the technique reported in Ref. [10]. These techniques enabled controlling linear arrays with eight [8] and nine dots [9]. Increasing the number of dots even further should be achievable, following a similar procedure.

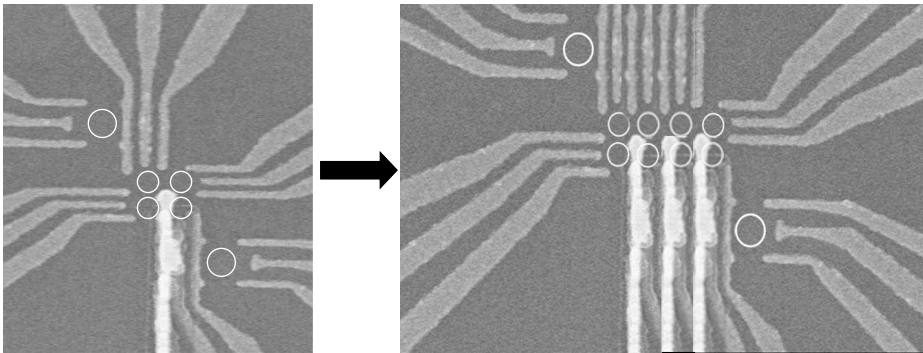


Figure 7.2: Proposal to scale up from a 2x2 dot array (left) to a 2x4 dot ladder (right), with the positions of the dots (white circles). The picture on the left is an SEM image of a real device. Whereas, the picture on the right is created by copy-pasting parts of the left image next to each other, to illustrate the scalability of the design.

Scaling the quantum dot array to the second dimension promises significant advantages for simulation and computation experiments due to increased connectivity. Exact solutions of models in 2D are often harder to achieve, compared to their linear counterparts. Quantum simulation offers a new way to study these 2D systems. 2D architectures are also currently favored in error correction protocols for quantum computation. The gate structures required to create these 2D arrays are quite different from the linear arrays. In this thesis, we have implemented a double-layer gate stack, with a center gate, to make a 2x2 dot array. This device showed significantly improved control over dot parameters compared to the previous attempt of making a 2x2 dot array [11]. Although

our gate design cannot be readily extended to make an arbitrary 2D array of shape $N \times M$, creating a ladder array of shape $2 \times N$ seems rather straight-forward. Fig. 7.2 shows how the gate-structure for the 2×2 dot array can be extended to make a 2×4 dot ladder. For 2×2 dot array as well as small ladder arrays, sensing dots can be placed adjacent to the dot array for charge sensing. A different charge detection technique should be adopted as the size of these ladder arrays increase. The gate-based dispersive read-out is a very promising alternative, which is compatible with the proposed gate design [12–16]. Modified versions of the $n+1$ method and automated tunnel coupling tuning can be employed to tune these arrays.

Finally, we discuss the scaling to arbitrary 2D arrays with $N \times M$ quantum dots, which is currently the most challenging problem in scaling. There are very few attempts to make 2D arrays larger than 2×2 dots. The 3×3 dot array reported in Ref. [17] doesn't exhibit the required control over the tunnel couplings. Moreover, the gate design used in this work is not scalable to arbitrary 2D arrays. Meanwhile, our attempt to create 1000×1000 dot arrays with global control didn't show any evidence of the Mott gap, probably due to high disorder in the 2DEG. In Ref. [18], a scalable gate-design based on cross-bar architecture is proposed to create large 2D arrays of quantum dots. This proposal is also currently disorder-limited as it requires the use of shared control lines. Whereas, the proposal in Ref. [19] requires significant development in fabrication to have individual voltage-control of each gate.

Currently, the gate voltages are optimized manually to create the dot arrays and control their parameters. As the number of dots in an array increases, we should try to automatize the tuning process. The first steps towards this automation are reported in Ref. [10, 20, 21]. The rising interest in using machine learning to quantum tune dot arrays can be leveraged to further improve the scope and the performance of automated tuning [22–25].

7.2.3. SIMULATION USING LARGER QUANTUM DOT ARRAY DEVICES

Once we achieve the current level of control over the Hamiltonian parameters in the larger arrays, they can be used to perform various quantum simulation experiments. Until now, the quantum simulation experiments performed using quantum dot arrays could be verified using numerical simulations. As we scale up the array, this will not be possible at some point, due to the limitation in computing power. This will enable us to achieve Feynman's ambition of leveraging the powers of quantum mechanics to learn new physics. This is obviously our ultimate goal for simulation experiments. But, I will argue that it is equally essential to perform as many simulations as possible with the smaller arrays. The experience gathered from these experiments will enable the full utilization of the larger arrays. More importantly, the verification of simulation results with numerical analysis will bestow the required confidence upon the uncorroborated simulations with larger arrays.

We should also identify the problems, that can be simulated with different dot arrays. Active collaboration with different theory groups will be extremely useful in this regard. Here, I briefly discuss a few possible options. The linear dot arrays are well suited to simulate different properties of the Heisenberg spin-chains [4, 26]. A quantum dot ladder of size $2 \times N$ will be useful to study weakly doped Hubbard ladders. The numerical

simulations of these ladders don't agree with analytical arguments on whether superconducting correlations dominate charge-density-wave correlations in these systems or vice versa [27]. Measuring correlations in a quantum dot ladder might be useful in resolving this conflict. Different 2D dot arrays ($2 \times N$ or $M \times N$) can also be used to study itinerant magnetism, as discussed in Chapter 5. Finally, a large 2D array ($M \times N$) of quantum dots with ample control over the parameter space will be a great tool to explore the Mott-Hubbard phase space, with all its richness.

BIBLIOGRAPHY

- [1] K. C. Nowack, M. Shafiei, M. Laforest, G. E. D. K. Prawiroatmodjo, L. R. Schreiber, C. Reichl, W. Wegscheider, and L. M. K. Vandersypen, *Science* **333**, 1269 (2011).
- [2] T. Hensgens, T. Fujita, L. Janssen, X. Li, C. J. Van Diepen, C. Reichl, W. Wegscheider, S. Das Sarma, and L. M. K. Vandersypen, *Nature* **548**, 70 (2017).
- [3] J. Preskill, *Quantum* **2**, 79 (2018).
- [4] E. Dagotto and T. M. Rice, *Science* **271**, 618 (1996) .
- [5] L. Balents, *Nature* **464**, 199 EP (2010).
- [6] A. W. Sandvik, *AIP Conference Proceedings* **1297**, 135 (2010) .
- [7] M. D. Shulman, O. E. Dial, S. P. Harvey, H. Bluhm, V. Umansky, and A. Yacoby, *Science* **336**, 202 (2012) .
- [8] C. Volk, A. M. J. Zwerver, U. Mukhopadhyay, P. T. Eendebak, C. J. van Diepen, J. P. Dehollain, T. Hensgens, T. Fujita, C. Reichl, W. Wegscheider, and L. M. K. Vandersypen, *npj Quantum Information* **5**, 29 (2019).
- [9] A. R. Mills, D. M. Zajac, M. J. Gullans, F. J. Schupp, T. M. Hazard, and J. R. Petta, *Nature Communications* **10**, 1063 (2019).
- [10] C. J. van Diepen, P. T. Eendebak, B. T. Buijtenorp, U. Mukhopadhyay, T. Fujita, C. Reichl, W. Wegscheider, and L. M. K. Vandersypen, *Applied Physics Letters* **113**, 033101 (2018) .
- [11] R. Thalineau, S. Hermelin, A. D. Wieck, C. Bäuerle, L. Saminadayar, and T. Meunier, *Applied Physics Letters* **101**, 103102 (2012).
- [12] J. I. Colless, A. C. Mahoney, J. M. Hornibrook, A. C. Doherty, H. Lu, A. C. Gossard, and D. J. Reilly, *Phys. Rev. Lett.* **110**, 046805 (2013).
- [13] M. F. Gonzalez-Zalba, S. Barraud, A. J. Ferguson, and A. C. Betz, *Nature Communications* **6**, 6084 EP (2015) .
- [14] G. Zheng, N. Samkharadze, M. Noordam, N. Kalhor, D. Brousse, A. Sammak, G. Scappucci, and L. Vandersypen, *arXiv preprint arXiv:1901.00687* (2019).

- [15] M. Urdampilleta, D. J. Niegemann, E. Chanrion, B. Jadot, C. Spence, P.-A. Mortemousque, L. Hutin, B. Bertrand, S. Barraud, R. Maurand, *et al.*, arXiv preprint arXiv:1809.04584 (2018).
- [16] A. Crippa, R. Ezzouch, A. Aprá, A. Amisse, L. Houtin, B. Bertrand, M. Vinet, M. Urdampilleta, T. Meunier, M. Sanquer, *et al.*, arXiv preprint arXiv:1811.04414 (2018).
- [17] P.-A. Mortemousque, E. Chanrion, B. Jadot, H. Flentje, A. Ludwig, A. D. Wieck, M. Urdampilleta, C. Bäuerle, and T. Meunier, arXiv preprint arXiv:1808.06180 (2018).
- [18] R. Li, L. Petit, D. P. Franke, J. P. Dehollain, J. Helsen, M. Steudtner, N. K. Thomas, Z. R. Yoscovits, K. J. Singh, S. Wehner, L. M. K. Vandersypen, J. S. Clarke, and M. Veldhorst, *Science Advances* **4** (2018) .
- [19] M. Veldhorst, H. G. J. Eenink, C. H. Yang, and A. S. Dzurak, *Nature Communications* **8**, 1766 (2017).
- [20] T. Baart, P. Eendebak, C. Reichl, W. Wegscheider, and L. Vandersypen, *Applied Physics Letters* **108**, 213104 (2016).
- [21] T. Botzem, M. D. Shulman, S. Foletti, S. P. Harvey, O. E. Dial, P. Bethke, P. Cerfontaine, R. P. G. McNeil, D. Mahalu, V. Umansky, A. Ludwig, A. Wieck, D. Schuh, D. Bougeard, A. Yacoby, and H. Bluhm, *Phys. Rev. Applied* **10**, 054026 (2018).
- [22] J. D. Teske, S. S. Humpohl, R. Otten, P. Bethke, P. Cerfontaine, J. Dedden, A. Ludwig, A. D. Wieck, and H. Bluhm, *Applied Physics Letters* **114**, 133102 (2019) .
- [23] S. S. Kalantre, J. P. Zwolak, S. Ragole, X. Wu, N. M. Zimmerman, M. Stewart, and J. M. Taylor, *npj Quantum Information* **5**, 6 (2019).
- [24] D. Lennon, H. Moon, L. Camenzind, L. Yu, D. Zumbühl, G. Briggs, M. Osborne, E. Laird, and N. Ares, arXiv preprint arXiv:1810.10042 (2018).
- [25] J. P. Zwolak, S. S. Kalantre, X. Wu, S. Ragole, and J. M. Taylor, *PLOS ONE* **13**, 1 (2018).
- [26] H. Bethe, *Zeitschrift für Physik* **71**, 205 (1931).
- [27] M. Dolfi, B. Bauer, S. Keller, and M. Troyer, *Phys. Rev. B* **92**, 195139 (2015).

ACKNOWLEDGEMENTS

My life in Delft started during the early days of QuTech. Although we grew dramatically as a department since then, the camaraderie has remained very much the same. During my time here, I had the pleasure to meet and interact with a multitude of people, many of whom had a profound impact on my life. Finally, it is time to express my heartfelt gratitude towards them.

First of all, **Lieven!** Thank you for giving me the opportunity to work in your group. The last four years have been the most challenging period of my life, but you were there to guide me through it. I appreciate the freedom you gave us to choose our projects. At the end of my first year, when the ‘many’ project was not progressing as expected, you readily allowed me to switch to the ‘few’ project. In retrospect, this was one of the decisive moments of my Ph.D. I learned a lot from our meetings, where you always asked the relevant questions and in the process pointed me towards the right path. You have also helped me grow as a person. I am a great admirer of your calm but decisive leadership, and I hope to emulate it in the future.

It was you, **Toivo**, who first taught me the ways around the cleanroom and the measurement lab. The amount of trust you placed on me early in my Ph.D. helped me grow as a researcher faster than I expected. Although our joint venture did not bear as much fruit as we expected, I learned a lot during our time together and did so with a lot of fun. In your dissertation, you called me your ‘final padawan’. Looking at the similarities between our Ph.D. trajectory, I can say you were right, as always. Next, it was my turn to work with **JP**. We worked together for more than two years, and I enjoyed every moment of it. You trained me on how to measure quantum dots. It was a great pleasure teaming up with you, not only because of your enormous knowledge of the subject matter and fun personality but also because your calmness in approaching a problem brought a counter-balance to my over-enthusiasm (impatience). I wish you all the best in setting up your new lab in Australia and life in general.

Jelmer, I had the maximum overlap with you in the group. We suffered in the cleanroom together and we have had some great time in and outside the lab. Thank you for all the nice memories. Also, thank you for helping me with the Dutch language, customs, and translations over the years. I am delighted to have you as my paranymp. The same is true for you **Anne-Marije**. Last few months, it has been an absolute pleasure to work with you. The way you effectively balance your numerous responsibilities in the group has always amazed me. You are a bundle of energy and I will eagerly wait to hear about teleportation. **Guoji, Xiao, Nodar**, I am going to miss our ‘Foodies’ outings. **Guoji**, thanks for all the drinks break chats and the news of (free) food. **Xiao**, keep on smiling and you will find all the resonances you want and some more. And of course, keep the gossips coming. **Sjaak**, I always enjoyed our short discussion sessions in F008. The future of the quantum simulation project can not be in better hands. **Stephan**, your enthusiasm is rather contagious. Thank you for all your programming and electronics

contribution and especially for the DMSolver. I am sure you will get your hero device any day now. **Tobias**, thank you for motivating me to go for runs and then slowing down to keep me company. I was fortunate to be able to rely on several senior members of the group. **Nodar, Takafumi, Tim, Tom, Roy, Gabriel, Nima, Christian, Sergei, Tobias, Patrick, Andrea, Pasquale, Erica**, thank you all for helping me over the years. My best wishes to **Floor, Kostas, Alice, Tzu-kan, Max, Haruki, Nico, Gertjan, Luca, Will, Luka, Brian, Alberto, Mario, Mohammad, Amir. Rens, Michael**, I had the opportunity to supervise you for your projects and it was a very enriching experience. Your enthusiasm reminded me of a younger me. I wish you a great future ahead.

Thank you, **Vincent**, for our frequent theory discussions. Also thanks to **Yao, Mark**, and **Eugene** for your time in discussing the Nagaoka results. Your feedback significantly improved our work. Thank you, **Delphine, Ale**, and **John** for your help and tips in the cleanroom. Thanks also to **Luc** and **Pieter** for all the programming support which made our measurements run so smoothly. **Slava, Menno**, and **Giordano** thank you for many discussions and feedback.

Life in QuTech offers a lot of activities outside the labs, from uitjes and barbecues to Friday night drinks and parties. **Michiel, Alex, James, Florian, Jasper, Fokko, Srijit, Damaz, Jouri, Willemijn, Adriaan, Niels, Matt, Max, Matt, Francesco, Jonas, Ramiro, Mohamed, Nandini, Glaucia, Suzanne, Norbert, Nathan** and many others thank you for all the fun times we have had over the years. I had a great time organizing the best uitje of all time with **Leon, Daniël, Sophie, Kenneth**, and **Oscar. Thijs, Christian** keep the sports day tradition going. I fondly remember all the conferences I attended with many of you. I don't know how much of those conferences I can still remember, but the evenings will be impossible to forget. Also thanks Lieven and the entire spin-qubit team for all the sweet memories of Iceland. A special thanks to the people who were there to have a chat from time to time, such as **Kaushik, LaReine**, and **Avradeep**.

Let me now thank the technical support team in QuTech, DEMO, and the Kavli cleanroom. **Hans**, I cannot count the number of times I dropped by your office with a new request or a problem, and you always had a solution. The same is true for you, **Raymond, Raymond**, and **Marijn**. My life as a researcher would be much harder without your help. **Nico**, I always asked you to make machined parts for me at the last moment, but you still delivered before I expected them. Thank you, **Olaf, Jason, Remco, Jelle, Siebe**, and **Mark** for keeping the labs in QuTech running so smoothly. Thanks also to **Marc, Marco, Arnold, Anja, Charles, Ewan**, and the rest of the cleanroom technicians for maintaining the cleanroom and its instruments. I would also like to thank **Jack, Ruud**, and the rest of the DEMO for their help.

Marja and **Yuki**, you made my relocation to the Netherlands easy as a breeze. Thank you for helping me navigate through all the forms and regulations of TU Delft. Also thank you **Chantal, Joanna, Jenny**, and the rest of the support staff for working your magic behind the scenes.

Finally, I would like to thank **Leo K, Ronald, Leo D C** and all the PIs for creating and maintaining an enjoyable work environment in QuTech.

A

FABRICATION RECIPE OF THE QUANTUM DOT DEVICES IN GAAS

In this Appendix, I describe the details of the recipe used to fabricate both the 2x2 and the eight-dot linear array device.

We start with some general remarks:

- The exposure details mentioned in different steps may need to be changed depending on the properties of the e-beam lithography machine. For large features (feature size $\sim \mu\text{m}$ or more), small variations of the machine don't affect the created structures. A dose test is recommended to deduce the required dose for finer features, which are sensitive to e-beam configuration.
- We followed a few tricks to increase the reliability of the lift-off process. The solvents are warmed up in a au-bain marie as well as stirred continuously with a rotating bar magnet throughout the lift-off process. Finally, the lift-off is finished by spraying the solvent on the sample using a syringe. This spraying doesn't damage the gates. Special care should be taken to not boil solvents while warming them up.
- The spinners used to coat resist are programmed to spin at 500 rpm for 5 s before they spin at the intended spinning speed for 55 s.

Detailed Fabrication Recipe:

(a) Substrate preparation

Clean Ga on the backside:

- pre-bake on hot plate: 120 °C (10 min)
- spin coat photoresist (S1813) on the front side of the wafer, spinning speed: 2000 rpm
- bake on hot plate: 110 °C (10 min)
- second layer spin coat photoresist (S1813) on the front side of the wafer, spinning speed: 2000 rpm
- bake on hot plate: 110 °C (10 min)
- 2 min in hot HCl (36-38%), temperature: 50 °C
- H₂O rinse (60 s): 30 s each in two consecutive beakers with H₂O
- dry with N₂ gun
- Check if there are traces of Ga left on the back of the wafer: if yes, repeat the previous three steps. Note: As long as gas formation occurs there is still Ga on the backside.
- acetone (30 min)

Remarks:

- The photoresist also desolves in HCl. So, one should always be careful that the HCl doesn't come into contact with the front surface of the wafer, which makes the wafer unusable. We use two layers of photoresist to prevent this.
- A small wiper (known as 'Q-tip' in the cleanroom) is often used to wipe the back-side of the wafer, which aids in the removal of Ga.

(b) Alignment markers

Preparation:

- acetone rinse (60 s)
- IPA rinse (60 s)
- dry with N₂ gun

Resist:

- spin coat PMMA 495K A8 (e-beam resist), spinning speed: 6000 rpm
- bake on hot plate: 175 °C (10 min)

Exposure:

- e-beam dose: 850 $\mu\text{C}/\text{cm}^2$ at 100 kV
- spot size 100 nm, beam current 250 nA

Developing:

- 1:3 MIBK / IPA (60 s)

- IPA stop (60 s)
- dry with N₂ gun

Evaporation:

- 10 nm Ti, rate 0.05 nm/s
- 80 nm Au, rate 0.15 nm/s

Lift-off:

- warm acetone (50 °C) 2 h while stirring with a bar magnet
- acetone spray
- IPA rinse (60 s)
- dry with N₂ gun

(c) Mesa etching

Preparation:

- acetone rinse (60 s)
- IPA rinse (60 s)
- dry with N₂ gun

Resist:

- spin coat PMMA 495K A8 (e-beam resist), spinning speed: 6000 rpm
- bake on hot plate: 175 °C (10 min)

Exposure:

- e-beam dose: 850 $\mu\text{C}/\text{cm}^2$ at 100 kV
- spot size 100 nm, beam current 250 nA

Developing:

- 1:3 MIBK / IPA (60 s)
- IPA stop (60 s)
- dry with N₂ gun

Etching:

- measure resist height using a profile meter to have a etching reference
- wet etch (piranha) in 1:8:240 H₂O₂/H₂SO₄/H₂O, etch time: 37 s
- H₂O rinse (60 s): 30 s each in two consecutive beakers with H₂O
- IPA rinse (60 s)
- dry with N₂ gun
- measure the height of the etched heterostructure using a profile meter, target: 90 nm

(d) Ohmic contacts

Preparation:

- acetone rinse (60 s)

- IPA rinse (60 s)
- dry with N₂ gun

Resist:

- spin coat PMMA 495K A8 (e-beam resist), spinning speed: 6000 rpm
- bake on hot plate: 175 °C (10 min)

Exposure:

- e-beam dose: 850 $\mu\text{C}/\text{cm}^2$ at 100 kV
- spot size 100 nm, beam current 250 nA

Developing:

- 1:3 MIBK / IPA (60 s)
- IPA stop (60 s)
- dry with N₂ gun

Plasma Cleaning:

- clean with oxygen plasma in a plasma chamber (Tepla), oxygen flow: 70 mL/min, plasma power: 120 W, time: 2 min

Evaporation:

- 5 nm Ni, rate 0.05 nm/s
- 150 nm AuGe, rate 0.15 nm/s
- 25 nm Ni, rate 0.10 nm/s

Lift-off:

- warm acetone (50 °C) for 2 h while stirring with a bar magnet
- acetone spray
- IPA rinse (60 s)
- dry with N₂ gun

Rapid thermal annealing:

- ramp from room temperature to 440 °C in 40 s, forming gas atmosphere (90% N₂, 10% H₂)
- anneal at 440 °C for 60 s in forming gas atmosphere
- bring temperature down from 440 °C to 80 °C in \approx 30 s, N₂ purge

Remarks:

- The plasma cleaning is introduced to clean any unwanted organic residue under the ohmic pads. We have sometimes faced problems with ohmic contacts to the 2DEG and this cleaning can be useful to combat that.

(e) Fine gates

Preparation:

- acetone rinse (60 s)
- IPA rinse (60 s)

- dry with N₂ gun

Resist:

- spin coat CSAR 62 (AR-P 6200) resist of 0.04 dilution, spinning speed: 5000 rpm
- bake on hot plate 150 °C (3 min)

Exposure:

- e-beam dose 350 $\mu\text{C}/\text{cm}^2$ at 100 kV
- estimated spot size 2-3 nm, beam current 900 pA

Developing:

- pentyl acetate (60 s)
- 1:1 MIBK / IPA (60 s)
- IPA stop (60 s)
- dry with N₂ gun

Evaporation:

- 5 nm Ti, rate 0.05 nm/s
- 20 nm Au, rate 0.05 nm/s

Lift-off:

- warm NMP (N-Methyl-2-Pyrrolidone) at 80 °C for 2 h while stirring with a bar magnet
- NMP spray
- cold acetone rinse (60 s)
- IPA rinse (60 s)
- dry with N₂ gun

(f) **SiN_x patch (only for 2x2 the devices)**

Preparation:

- acetone rinse (60 s)
- IPA rinse (60 s)
- dry with N₂ gun

Resist:

- spin coat CSAR 62 (AR-P 6200) resist of 0.04 dilution, spinning speed: 4000 rpm
- bake on hot plate 150 °C (3 min)

Exposure:

- e-beam dose 450 $\mu\text{C}/\text{cm}^2$ at 100 kV
- estimated spot size 2-3 nm, beam current 900 pA

Developing:

- pentyl acetate (60 s)

- 1:1 MIBK / IPA (60 s)
- IPA stop (60 s)
- dry with N₂ gun

Evaporation:

- 10 nm Ti, rate 0.05 nm/s
- 100 nm Au, rate 0.1 nm/s

Lift-off:

- warm NMP (N-Methyl-2-Pyrrolidone) at 80 °C for 2 h while stirring with a bar magnet
- NMP spray
- cold acetone rinse (60 s)
- IPA rinse (60 s)
- dry with N₂ gun

(g) Center gate (only for 2x2 the devices)

Preparation:

- acetone rinse (60 s)
- IPA rinse (60 s)
- dry with N₂ gun

Resist:

- spin coat CSAR 62 (AR-P 6200) resist of 0.09 dilution, spinning speed: 4000 rpm
- bake on hot plate 150 °C (3 min)

Exposure:

- e-beam dose 440 $\mu\text{C}/\text{cm}^2$ at 100 kV
- estimated spot size 2-3 nm, beam current 900 pA

Developing:

- pentyl acetate (60 s)
- 1:1 MIBK / IPA (60 s)
- IPA stop (60 s)
- dry with N₂ gun

Sputtering:

- 50 nm SiN_x, Ar environment

Lift-off:

- warm NMP (N-Methyl-2-Pyrrolidone) at 80 °C for 2 h while stirring with a bar magnet
- NMP spray
- cold acetone rinse (60 s)

- IPA rinse (60 s)
- dry with N₂ gun

(h) **Large gates and bondpads**

Preparation:

- acetone rinse (60 s)
- IPA rinse (60 s)
- dry with N₂ gun

Resist:

- spin coat PMMA 495K A8 (e-beam resist), spinning speed: 6000 rpm
- bake on hot plate: 175 °C (10 min)

Exposure:

- e-beam dose: 850 $\mu\text{C}/\text{cm}^2$ at 100 kV
- spot size 100 nm, beam current 250 nA

Developing:

- 1:3 MIBK / IPA (60 s)
- IPA stop (60 s)
- dry with N₂ gun

Evaporation:

- 50 nm Ti, rate: 0.10 nm/s
- 200 nm Au, rate: 0.15 nm/s

Lift-off:

- warm acetone (50 °C) 2 h while stirring with a bar magnet
- acetone spray
- IPA rinse (60 s)
- dry with N₂ gun

CURRICULUM VITÆ

Uditendu MUKHOPADHYAY

27/03/1992 Born in Bankura, India.

EDUCATION

- 2002–2008 Secondary School
Ramakrishna Mission Vidyapith, Purulia, India
- 2008–2010 Higher Secondary School
Bankura Zilla School, India
- 2010–2015 Integrated MS in Physical Sciences (with Gold Medal)
Indian Institute of Science Education and Research, Kolkata
Supervision: Prof. dr. C. Mitra
Thesis: Surface optical and bulk acoustic phonons in topological insulator $\text{Bi}_2\text{Se}_2\text{Te}$
- 2015–2019 PhD in Experimental Quantum Physics
Delft University of Technology
Supervision: Prof. dr. ir. L.M.K. Vandersypen
Dissertation topic: Quantum simulation using arrays of gate-defined quantum dots

LIST OF PUBLICATIONS

1. *Nagaoka ferromagnetism observed in a quantum dot plaquette*
J.P. Dehollain*, **U. Mukhopadhyay***, V.P. Michal, Y. Wang, B. Wunsch, C. Reichl, W. Wegscheider, M.S. Rudner, E. Demler, L.M.K. Vandersypen,
arXiv:1904.05680
2. *A 2X2 quantum dot array with controllable inter-dot tunnel couplings*
U. Mukhopadhyay*, J.P. Dehollain*, C. Reichl, W. Wegscheider, L.M.K. Vandersypen,
Appl. Phys. Lett. **112**, 183505 (2018) (Editor's Pick)
3. *A capacitance spectroscopy-based platform for realizing gate-defined electronic lattices*
T. Hensgens*, **U. Mukhopadhyay***, P. Barthelemy*, R.F.L. Vermeulen, R.N. Schouten, S. Fal-lahi, G.C. Gardner, C. Reichl, W. Wegscheider, M.J. Manfra, L.M.K. Vandersypen,
Journal of Applied Physics **124**, 124305 (2018) (Editor's Pick)
4. *Loading a quantum-dot based "Qubyte" register*
C. Volk*, A.M.J. Zwerver*, **U. Mukhopadhyay**, P.T. Eendebak, C.J. van Diepen, J.P. Dehollain,
T. Hensgens, C. Reichl, W. Wegscheider, L.M.K. Vandersypen,
npj Quantum Information **5**, 29 (2019)
5. *Electrode-induced lattice distortions in GaAs multi-quantum-dot arrays*
A. Pateras, J. Carnis, **U. Mukhopadhyay**, M.-I. Richard, S.J. Leake, T.U. Schüllli, C. Reichl, W. Wegscheider, J.P. Dehollain, L.M.K. Vandersypen, P.G. Evans
Journal of Materials Research, 1-11 (2019)
6. *Ab Initio Exact Diagonalization Simulation of the Nagaoka Transition in Quantum Dots*
Y. Wang, J.P. Dehollain, F. Liu, **U. Mukhopadhyay**, M.S. Rudner, L.M.K. Vandersypen, E. Demler
arXiv:1907.01658
7. *Automated tuning of inter-dot tunnel coupling in double quantum dots*
C.J. van Diepen, P.T. Eendebak, B.T. Buijtenorp, **U. Mukhopadhyay**, T. Fujita, C. Reichl, W. Wegscheider, L.M.K. Vandersypen,
Appl. Phys. Lett. **113**, 033101 (2018) (Editor's Pick)
8. *Mesoscopic Elastic Distortions in GaAs Quantum Dot Heterostructures*
A. Pateras, J. Park, Y. Ahn, J.A. Tilka, M.V. Holt, C. Reichl, W. Wegscheider, T.A. Bart, J.P. De-hollain, **U. Mukhopadhyay**, L.M.K. Vandersypen, P.G. Evans,
Nano Lett. 2018, 18, 5, 2780-2786
9. *Surface optical and bulk acoustic phonons in the topological insulator, Bi₂Se₃*
U. Mukhopadhyay*, D. Chaudhuri*, J. Sarkar, S. Singh, R.K. Gopal, S. Tamm, P.C. Upadhyay, C. Mitra,
Appl. Phys. Lett. **106**, 241106 (2015)

* These authors contributed equally.